WL-TR-95-4022

PHOTO-ASSISTED EPITAXIAL GROWTH FOR III-V SEMICONDUCTORS

SELECTIVE AREA EPITAXY

C.W. TU
H.K. DONG

DEPT OF ELECTRICAL AND COMPUTER ENGINEERING
UNIVERSITY OF CALIFORNIA, SAN DIEGO
LA JOLLA, CA 92093-0407

MARCH 1995

FINAL REPORT FOR 09/01/90-10/31/94

APPROVED FOR PUBLIC RELEASE; DISTRIBUTION IS UNLIMITED.

DTIC
SELECTE
AUG 28 1995
S D
B

DTIC QUALITY INSPECTED 5

MATERIALS DIRECTORATE
WRIGHT LABORATORY
AIR FORCE MATERIEL COMMAND
WRIGHT PATTERSON AFB OH 45433-7734

19950825 065

NOTICE

When Government drawings, specifications, or other data are used for any purpose other than in connection with a definitely Government-related procurement, the United States Government incurs no responsibility or any obligation whatsoever. The fact that the government may have formulated or in any way supplied the said drawings, specifications, or other data, is not to be regarded by implication, or otherwise in any manner construed, as licensing the holder, or any other person or corporation; or as conveying any rights or permission to manufacture, use, or sell any patented invention that may in any way be related thereto.

This report is releasable to the National Technical Information Service (NTIS). At NTIS, it will be available to the general public, including foreign nations.

This technical report has been reviewed and is approved for publication.

WILLIAM C. MITCHEL
Project Monitor
Electronic and Optical Mat'ls Branch

ROBERT L. DENISON, Chief
Electronic and Optical Matls Branch

William R Woody
WILLIAM R. WOODY, Chief
Electromagnetic Matls and Surv Division
Materials Directorate
Wright Laboratory

If your address has changed, if you wish to be removed from our mailing list, or if the addressee is no longer employed by your organization please notify WL/MLPO, WPAFB, OH 45433-7707 to help us maintain a current mailing list.

Copies of this report should not be returned unless return is required by security considerations, contractual obligations, or notice on a specific document.

REPORT DOCUMENTATION PAGE

Form Approved
OMB No. 0704-0188

Public reporting burden for this collection of information is estimated to average 1 hour per response, including the time for reviewing instructions, searching existing data sources, gathering and maintaining the data needed, and completing and reviewing the collection of information. Send comments regarding this burden estimate or any other aspect of this collection of information, including suggestions for reducing this burden, to Washington Headquarters Services, Directorate for Information Operations and Reports, 1215 Jefferson Davis Highway, Suite 1204, Arlington, VA 22202-4302, and to the Office of Management and Budget, Paperwork Reduction Project (0704-0188), Washington, DC 20503.

1. AGENCY USE ONLY *(Leave blank)*

2. REPORT DATE
3 March 1995

3. REPORT TYPE AND DATES COVERED
Final. 1 Sept. 1990 - 31 Oct. 1994

4. TITLE AND SUBTITLE
Photo-Assisted Epitaxial Growth for III-V Semiconductors

5. FUNDING NUMBERS
CF 33615-90-C-5946
PE 62102
PR 2423
TA 01
WU B7

6. AUTHOR(S)
C.W. Tu and H.K. Dong

7. PERFORMING ORGANIZATION NAME(S) AND ADDRESS(ES)
Department of Electrical and Computer Engineering
University of California, San Diego
La Jolla, CA 92093-0407

8. PERFORMING ORGANIZATION REPORT NUMBER
TU-AFWL-95

9. SPONSORING/MONITORING AGENCY NAME(S) AND ADDRESS(ES)
Materials Directorate
Wright Laboratory
Air Force Materiel Command
Wright Patterson AFB, OH 45433-7734

10. SPONSORING/MONITORING AGENCY REPORT NUMBER
WL-TR-95-4022

11. SUPPLEMENTARY NOTES

12a. DISTRIBUTION/AVAILABILITY STATEMENT
Approved for public release;
Distribution unlimited.

12b. DISTRIBUTION CODE

13. ABSTRACT *(Maximum 200 words)*

We have investigated laser-enhanced growth of GaAs by metal-organic molecular beam epitaxy (MOMBE) with triethylgallium (TEGa) and solid arsenic and by chemical beam epitaxy (CBE) with TEGa and a safer, alternative organometallic precursor, tris-dimethylaminoarsenic (TDMAAs), to the highly toxic arsine. We discovered that with TDMAAs we can increase the laser-enhanced growth temperature window by 100 °C, as compared to that with arsine or arsenic. CBE growth of InP and InGaP using tris-dimethylaminophosphorus (TDMAP) and tertiarybutylphosphine (TBP) is also reported. We discovered the etching effect of TDMAAs and TDMAP, and investigated laser-enhanced etching of GaAs by TDMAAs. We also investigated laser-enhanced carbon and silicon doping in GaAs with diiodomethane ($\mathrm{CI_2H_2}$) and disilane, respectively. We can achieve a two-order-of-magnitude enhancement in p-type carbon doping with $\mathrm{CI_2H_2}$ by laser irradiation. Finally, we report on lateral bandgap variation by laser-modified compositional change in InGaAs/GaAs multiple quantum wells grown by MOMBE and CBE.

14. SUBJECT TERMS
GaAs, InGaAs, InP, InGaP, argon ion laser, MOMBE, CBE, strain, quantum wells, doping, etching

15. NUMBER OF PAGES
192

16. PRICE CODE

17. SECURITY CLASSIFICATION OF REPORT	**18. SECURITY CLASSIFICATION OF THIS PAGE**	**19. SECURITY CLASSIFICATION OF ABSTRACT**	**20. LIMITATION OF ABSTRACT**
unclassified	unclassified	unclassified	SAR

NSN 7540-01-280-5500

Standard Form 298 (Rev. 2-89)
Prescribed by ANSI Std. Z39-18
298-102

TABLE OF CONTENTS

List of Figures vi

List of Tables xv

1. Program Summary 1
    - 1.1 Program Objectives 1
    - 1.2 Accomplishments 2
    - 1.3 References 3

2. System Development 4
    - 2.1 Facility 4
    - 2.2 Laser and Optics 4
    - 2.3 Gas Manifold 7
    - 2.4 Growth Chamber 13
        - 2.4.1 Pumping and pressure measurement 13
        - 2.4.2 RHEED 13
        - 2.4.3 Mass spectrometer 16
        - 2.4.4 Computer-controlled growth operation 17
    - 2.5 Safety Handling 17
        - 2.5.1 Group V sources 17
        - 2.5.2 Group III metalorganics 18
        - 2.5.3 Exhaust scrubbing and monitoring 19
    - 2.6 Temperature Measurement by Infrared Laser Interferometry 21
        - 2.6.1 Principle of operation 21
        - 2.6.2 Substrate temperature calibration 22
        - 2.6.3 Measurement of Ar ion laser-induced local heating 29
    - 2.7 References 35

3. Laser-Assisted MOMBE of GaAs Using As_4 37

3.1 Introduction 37
3.2 MOMBE of GaAs 37
3.3 Laser-Assisted MOMBE of GaAs 47
3.4 References 55
4. Laser-Modified MOMBE of InGaAs/GaAs MQWs 59
4.1 Introduction 59
4.2 MOMBE of InGaAs 59
4.3 Laser-Modified MOMBE of InGaAs/GaAs MQWs 66
4.4 References 72
5. Laser-Assisted CBE of GaAs Using a Novel Precursor 74
5.1 Introduction 74
5.2 TDMAAs Decomposition 75
5.3 CBE of GaAs 78
5.4 Laser-Assisted CBE of GaAs 90
5.5 References 95
6. Laser-Modified CBE of InGaAs/GaAs MQWs 99
6.1 RHEED Study on CBE of InGaAs 99
6.2 Laser-Modified CBE of InGaAs/GaAs MQWs 106
6.3 References 114
7. Laser-Enhanced Doping and Etching with Novel Gas Sources 115
7.1 Carbon Doping by a Novel Dopant Precursor CI_2H_2 115
7.1.1 Carbon doping in GaAs by MBE, MOMBE, and CBE 116
7.1.2 Laser-enhanced carbon doping 122
7.2 Silicon Doping by Disilane 126
7.3 Laser-Enhanced *In Situ* GaAs Etching 129
7.4 References 133
8. CBE of Phosphorous-Based Materials by Chemical Beam Epitaxy 137

8.1. Introduction 137

8.2 CBE of InP 138

8.3 CBE of InGaP 147

8.4 References 151

9. Recommendations 155

9.1 Modification of Laser Optics 155

9.2 Laser-Assisted CBE of InGaP with TBP and TDMAP 155

9.3 Laser Holographic Growth 155

Appendix A Selectively Regrown Carbon-Doped (Al)GaAs by CBE with Novel Gas Sources for HBT Applications 158

A1 Introduction 158

A2 Selective-Area Growth of (Al)GaAs 159

A3 Regrown LBC Structure for HBT 168

A4 References 170

Appendix B Publications and Presentations 174

Accession For
NTIS GRA&I ☑
DTIC TAB ☐
Unannounced ☐
Justification
By
Distribution/
Availability Codes
Dist | Avail and/or Special
A-1

LIST OF FIGURES

Fig. 2.1 Laser-assisted CBE system. 5

Fig. 2.2 CBE system and its control panel. 6

Fig. 2.3 Ar ion laser beam path. 8

Fig. 2.4 The schematic drawing of the laser-assisted CBE system. 9

Fig. 2.5 TDMAAs, TBP and hydrogen gas cabinets. 11

Fig. 2.6 TDMAAs and TBP gas panel. 12

Fig. 2.7 The turbomolecular and mechanical pump system. 14

Fig. 2.8 The schematic drawing of the RHEED system. 15

Fig. 2.9 The schematic drawing of sampling points for the MDA-16 system. 20

Fig. 2.10 The physical illustration of interferometry. 23

Fig. 2.11 The infrared laser interferometry setup in an annealing furnace. 24

Fig. 2.12 Interferogram of a 500-micron-thick GaAs sample by 1.15 μm He-Ne laser inside a furnace. 26

Fig. 2.13 Temperature calibration curves for GaAs and InP samples by IR laser interferometry in a furnace. 27

Fig. 2.14 Substrate heating power versus sample temperature calibrated in MBE growth chamber. 28

Fig. 2.15 The schematic drawing of an optical fiber-coupled laser interferometric system. 30

Fig. 2.16 Measurement setup of substrate temperature change induced by Ar ion laser heating. 31

Fig. 2.17 Interferogram of GaAs sample under a 2000 W/cm^2 Ar ion laser irradiation, (a) without indium attachment

and (b) with indium attachment. 33
Fig. 2.18 GaAs sample surface temperature increment versus Ar ion laser power input. 34
Fig. 3.1 RHEED intensity oscillations. 39
Fig. 3.2 GaAs growth rate versus substrate temperature at different TEGa flow rates for an arsenic flux of 3.0×10^{-6} Torr. 40
Fig. 3.3 GaAs growth rate versus TEGa flow rate at different substrate temperatures under an arsenic flux of 3.0×10^{-6} Torr. 42
Fig. 3.4 RHEED intensity oscillation data for (a) linear region, (b) transition region, and (c) stabilization region. 44
Fig. 3.5 Arsenic-induced growth rate versus $1/T_S$ at a TEGa flow rate of 0.35 sccm for different arsenic fluxes. 46
Fig. 3.6 RHEED oscillations with and without laser irradiation at a substrate temperature of 365°C. Enhanced growth of GaAs is observed with laser irradiation, while no growth is observed without laser irradiation. 49
Fig. 3.7 RHEED oscillations with and without laser irradiation with TEGa and arsenic supply at a substrate temperature of 410°C. 50
Fig. 3.8 The growth rate as a function of substrate temperature with and without laser irradiation. 51
Fig. 3.9 TEGa absorption cross section as a function of laser wavelength. 53
Fig. 3.10 RHEED data showing arsenic desorption behavior under laser irradiation and arsenic exposure. 54
Fig. 3.11 Growth rate versus Ar^+ laser power at constant TEGa flow but under different arsenic flux at a substrate temperature of 390°C. 56

Fig. 4.1 RHEED intensity oscillation data for InGaAs and GaAs grown on (100) GaAs substrate. 61

Fig. 4.2 InGaAs transient growth behavior
(a) with changing TMIn flow rate
(b) with changing substrate temperature. 62

Fig. 4.3 X-ray rocking curves for the InGaAs/GaAs MQW structure grown at 500°C
(a) Experimental result,
(b) Simulation result (uniform distribution of well thickness and indium concentration),
(c) Simulation result (nonuniform distribution of well thickness and indium concentration). 64

Fig. 4.4 The critical number of MQW periods as a function of indium concentration for $In_xGa_{1-x}As$(85Å)/GaAs(140Å), $In_xGa_{1-x}As$(25Å)/GaAs(140Å), and $In_xGa_{1-x}As$(20Å)/GaAs(180Å) MQW structures. 65

Fig. 4.5 Effects of Ar ion laser irradiation on InGaAs/GaAs multiple quantum wells
(a) Surface morphology by Nomarski microscopy (50x),
(b) Dektak depth profile. 68

Fig. 4.6 Low temperature photoluminescence spectra of InGaAs/GaAs MQW structure grown at a substrate temperature of 500°C. 69

Fig. 4.7 Low temperature photoluminescence spectra of InGaAs/GaAs MQW structure grown at a substrate temperature of 550°C. 71

Fig. 5.1 Mass spectra resulting from (a) uncracked and (b) cracked TDMAAs. 77

Fig. 5.2 GaAs growth rate as a function of substrate temperature, with a TEGa flow rate of 0.5 sccm and a H_2 flow rate for TDMAAs of 2 sccm. The inserted figure shows the Ga-induced RHEED intensity oscillations. 79

Fig. 5.3 Arsenic-controlled growth rate as a function of substrate temperature, with a TEGa flow rate of 0.5 sccm and a H_2 flow rate for TDMAAs of 2 sccm. The inserted figure shows the arsenic-induced RHEED intensity oscillations. 80

Fig. 5.4 GaAs growth rate as a function of V/III incorporation ratio, with a substrate temperature of 510°C and TEGa flow rate of 0.5 sccm. 82

Fig. 5.5 The dependence of the carrier concentration on the substrate temperature. The TEGa and H_2 flow rates used for GaAs growth are 0.7 sccm and 2 sccm, respectively. 83

Fig. 5.6 (a) SIMS profile for the p-type GaAs sample grown at 440°C with a carbon concentration of $1x10^{17}$ cm^{-3}, a sulfur concentration of $6x10^{15}$ cm^{-3} and a silicon concentration of $5x10^{15} cm^{-3}$.
(b) SIMS profile for the n-type GaAs sample grown at 530°C with a silicon concentration of $1.5x10^{16}$ cm^{-3}. 84

Fig. 5.7 Variation of the hole concentration with temperature for the GaAs sample grown at 480°C. 87

Fig. 5.8 (a) Concentration dependence of the Hall mobility in n-GaAs at 300 K.
(b) Concentration dependence of the Hall mobility in n-GaAs at 77 K. 89

Fig. 5.9 The substrate temperature dependence of growth rates of laser-irradiated and nonirradiated areas. The solid lines denote the growth data obtained using TDMAAs, while the dashed and dotted lines denote the data from AsH_3 and As_4, respectively. 91

Fig. 5.10 (a) Nomarski micrograph (60x) of the GaAs line pattern grown by Ar-ion-laser-assisted CBE with the laser beam scanning at about 2 Hz and a laser power density of 550 W/cm^2.
(b) The cross-section profile of the line pattern measured by a Dektak stylus profiler. 93

Fig. 5.11 The growth rate dependence of laser power density at a substrate temperature of 340°C. The TEGa and H_2 flow rates used for GaAs growth are 0.5 sccm and 2 sccm, respectively. 94

Fig. 5.12 X-ray rocking curve and low-temperature PL spectra of GaAs grown with or without argon ion laser irradiation. The two peaks in the PL spectra, at 821 nm and 830 nm, are bound exciton and conduction band-to-carbon peaks, respectively. 96

Fig. 6.1 X-ray rocking curves for InGaAs/GaAs MQWs grown at 550°C with (a) cracked TDMAAs, and (b) uncracked TDMAAs. 100

Fig. 6.2 The RHEED intensity oscillation data for InGaAs grown on a (100) GaAs substrate at substrate temperatures of 500 and 525°C with flow rates of TEGa, TMIn, and H_2 (for TDMAAs) kept at 0.4, 0.06, and 2 sccm, respectively. 102

Fig. 6.3 The growth rate of InGaAs at each period of intensity oscillation versus the number of oscillations. 103

Fig. 6.4 X-ray rocking curves for InGaAs/GaAs MQWs grown at 500 and 525°C. 105

Fig. 6.5 X-ray rocking curves (a and c) and simulations (b and d) based on the dynamical theory for a 10-period InGaAs/GaAs MQW structure grown at 500°C with (a and b) and without (c and d) laser irradiation. 107

Fig. 6.6 (a) Indium composition, and (b) InGaAs well thickness as a function of substrate temperature with and without laser irradiation. 108

Fig. 6.7 GaAs growth rate as a function of (a) substrate temperature with and without laser irradiation, and (b) V/III incorporation ratio. 110

Fig. 6.8 (a) Indium composition, and (b) InGaAs well thickness as a function of laser power density with and without laser irradiation. 112

Fig. 6.9 (a) Low-temperature PL spectra of InGaAs/GaAs MQWs grown at a substrate temperature of 500°C, and (b) FWHM of PL exciton peaks as a function of substrate temperature. 113

Fig. 7.1 A schematic of the $\mathrm{CI_2H_2}$ doping line. 117

Fig. 7.2 Hole concentration of GaAs as a function of (a) the upstream $\mathrm{CI_2H_2}$ vapor pressure, and (b) the leak valve setting. 118

Fig. 7.3 Typical (400) X-ray rocking curve of a highly carbon-doped GaAs film with the thickness of 0.5 μm and a hole concentration of $8.8\mathrm{x}10^{19}$ cm^{-3}. 120

Fig. 7.4 Hole concentration of carbon-doped GaAs samples grown by MBE, MOMBE, and CBE as a function of the leak valve setting. 121

Fig. 7.5 The room-temperature hole mobility as a function of hole concentration for as-grown GaAs samples. The solid line is the Hilsum curve. 123

Fig. 7.6 (a) Hole concentration as a function of the substrate temperature, and (b) room-temperature Hall mobility as a function of hole concentration for carbon-doped GaAs samples with and without laser irradiation. 124

Fig. 7.7 Electron concentration as a function of (a) Si_2H_6 flow rate, and (b) substrate temperature. 127

Fig. 7.8 Room-temperature Hall mobility as a function of electron concentration for silicon-doped GaAs samples with and without laser irradiation. 128

Fig. 7.9 (a) The SEM picture showing the TDMAAs etching effect at 650°C on a SiO_2-masked GaAs patterned substrate.
(b) The SEM picture showing the GaAs surface etched by TDMAAs at 550°C. 131

Fig. 7.10 GaAs etch rate with and without laser irradiation as a function of substrate temperature. 132

Fig. 7.11 SEM pictures showing the surface morphology of the samples grown by (a) uncracked TDMAAs at 420°C, (b) uncracked TDMAAs at 460°C, (c) uncracked TDMAAs at 540°C, and (d) cracked TDMAAs at 540°C. 134

Fig. 8.1 (a) Phosphorous species, and (b) the byproducts as a function of the TDMAP cracker temperature. 139

Fig. 8.2 Typical indium-induced RHEED intensity oscillations for InP grown at 470°C with a V/III incorporation ratio of 1.3. 140

Fig. 8.3 Typical PL spectrum of an unintentionally doped InP epilayer using cracked TDMAP. 141

Fig. 8.4 InP surface morphology. 143

Fig. 8.5 The SEM picture showing the TDMAP etching effect at 570°C on a SiO_2-masked GaAs patterned substrate. 144

Fig. 8.6 The dependence of the InP growth rate on the TMIn flow rate using cracked TBP and cracked TDMAP. 145

Fig. 8.7 InP growth rate as a function of substrate temperature. 146

Fig. 8.8 SEM photograph of a typical InGaP surface grown on a GaAs substrate using uncracked TDMAP. 148

Fig. 8.9 X-ray rocking curve for the InGaP sample grown at a substrate temperature of 500°C with a TDMAP cracker temperature at 750°C. 149

Fig. 8.10 SEM photograph showing the surface morphology of the InGaP sample grown at 500°C with TDMAP cracked at 750°C. 150

Fig. 8.11 SEM photograph showing the "lumpy" surface morphology for the InGaP sample grown at 470°C. 152

Fig. 8.12 X-ray rocking curve of InGaP layer grown at 500°C with TBP cracked at 850°C. 153

Fig. 8.13 The low-temperature PL spectrum of the InGaP layer grown by cracked TBP. 154

Fig. 9.1 (a) Laser holography setup.
(b) GaAs grating pattern. 157

Fig. A1 SEM photographs for GaAs selective area growth:
(a) using uncracked TDMAAs at a substrate temperature of 440°C,
(b) using uncracked TDMAAs at 540°C, and
(c) using cracked TDMAAs at 540°C.
The stripe is parallel to the $01\bar{1}$] direction. 161

Fig. A2 SEM photograph of a selective GaAs:C layer in a stripe opening of 5 μm grown at 540°C with a V/III ratio of 1.85. 163

Fig. A3 Broad-area growth rate and "rabbit-ear" thickness of GaAs:C layers as a function of stripe openings for two values of V/III ratios. The thickness of the GaAs:C layer is 470 nm. 164

Fig. A4 Schematic cross-section of GaAs:C layers grown at V/III ratio of (a) 1.7 (b) 2.4 (c) 3.5 (d) 5.7 along $01\bar{1}$] and [011] directions. 166

Fig. A5 The typical SEM photographs of GaAs layers with (a) (311)A facets along $01\bar{1}$] direction, and (b) vertical sidewalls along [011] direction grown at a V/III of 1.7. 167

Fig. A6 An SEM photograph and schematic cross-section of the embedded SAE AlGaAs/GaAs:C layers grown in an undercut groove at a V/III ratio of 1.3. The stripe is along the $01\bar{1}$] direction. 169

Fig. A7 Common-emitter current gain as a function of collector current for the original and the regrown external-base HBT structures. 171

LIST OF TABLES

Table 2.1 Toxic data of group-V precursors 18
Table 2.2 Alarm levels of TDMAAs and TBP 19

1. Program Summary

1.1 Program Objectives

The goal of this project is to develop a novel growth method, photo-assisted epitaxy of III-V semiconductor, for material science and applications. We used laser-assisted metalorganic molecular beam epitaxy (MOMBE) or chemical beam epitaxy (CBE) as a direct-writing technique to grow III-V semiconductor materials. This could possibly remove the conventional photoresist mask process in today's semiconductor industry, and simplify fabrication processes of electronic and optoelectronic devices. This could also enable us to integrate various devices, e.g., waveguide and modulator, and develop novel devices, e.g., multiple-wavelength laser.[1.1] It was hoped that we could perform in situ monitoring of the laser-assisted growth process, achieve selective-area growth, doping, and compositional modification, and grow novel III-V heterostructures. We used Hall-effect measurements, photoluminescence (PL), X-ray diffraction, scanning electron microscope (SEM), and Dektak stylus profiler to characterize the samples grown by laser-assisted CBE.

Another aspect of this project is to evaluate safer, alternative organometallic group V gas sources for CBE and laser-assisted CBE applications. Since arsine and phosphine are highly toxic and compressed in high-pressure cylinders, great efforts have been undertaken to develop novel organometallic arsenic reagents as alternative sources in metalorganic vapor phase epitaxy (MOVPE) and CBE. In our work, we used tris-dimethylaminoarsenic (TDMAAs), tris-dimethylaminophosphine (TDMAP), and tertiarybutylphosphine (TBP) as the group-V sources, which are far less toxic and have much lower vapor pressure than the hydrides. We also evaluated carbon doping in CBE and laser-assisted CBE using a novel dopant precursor, diiodomethane (CI_2H_2). It was hoped that we would obtain some unique characteristics in growing III-V semiconductors by laser-assisted CBE using these safer novel gas sources.

1.2 Accomplishments

During the 4-year duration covered by this report, significant progress was achieved on all aspects of laser-assisted CBE. The major achievements are highlighted as follows:

- Developed a laser-assisted CBE system. Set up a video-camera system for monitoring reflection high-energy electron diffraction (RHEED) and computerized data acquisition and image analysis.
- Set up infrared laser interferometry to calibrate the substrate temperature, and measure the temperature rise caused by laser local heating. Optical fibers were used for ease of use.
- Designed and built interface hardware and wrote a control software for computer control of valves, shutters, and mass flow controllers.
- Built a computer interface (including one for a cryostat) and wrote an analysis software for computer control of Hall measurements.
- Observed RHEED intensity oscillations during laser irradiation in laser-assisted MOMBE of GaAs using TEGa and solid arsenic.
- Discovered that TDMAAs, as a safer alternative to arsine, gives a wider temperature range of enhanced growth as compared to using solid arsenic and arsine. The enhanced growth rate was found to depend on substrate temperature, laser power density, and laser wavelength (visible or ultraviolet).
- Observed lateral variation of photoluminescence (PL) exciton peaks for InGaAs/GaAs multiple quantum wells grown by laser-modified MOMBE using TEGa and solid arsenic and laser-modified CBE using TEGa and TDMAAs.

- Performed laser-enhanced silicon doping by disilane and carbon doping by CI_2H_2. Much higher hole concentration (two orders of magnitude) was obtained in the carbon-doped GaAs films in the laser-irradiated area.
- Achieved *in situ* GaAs etching using TDMAAs, and etching rate was enhanced by laser irradiation.
- Performed selective-area epitaxy on SiO_2-masked GaAs substrates, and regrew external base to improve heterojunction bipolar transistors (HBTs).
- Wrote 17 papers and gave 17 conference presentations which are listed in Appendix B.

In summary, the much wider temperature window for selective-area growth using TDMAAs, the good structural and optical properties of low-temperature grown GaAs films, the selective-area doping and composition modification, and the enhanced GaAs etching by laser irradiation will provide novel applications for optoelectronic devices.

1.3 References

1.1 R. Iga, T. Yamada, and H. Sugiura, Appl. Phys. Lett. 64, 983 (1994).

2. System Development

2.1 Facility

A Perkin-Elmer 425B MBE system was modified to handle gas load in MOMBE and CBE. Gas manifolds for both group III and group V sources were installed, as were a diffusion pump and later a turbomolecular pump. In the early phase of this program, all the MOMBE and laser-assisted MOMBE growth experiments employed elemental arsenic and group III alkyls, and the results will be discussed in Chapters 3 and 4. In order to use gas-source group V precursors, we had to meet various safety requirements. Another laboratory space was modified to have a toxic-gas exhaust line; gas cylinders were installed in gas cabinets; and an MDA-16 toxic-gas monitor was operated continuously around the clock. Once the new laboratory was completed, the machine was disassembled and moved to this room. We continued the MOMBE work while setting up the gas manifold for the group-V precursors. The final setup was completed in January 1993, and two photographs of the system are shown in Figs. 2.1 and 2.2. The CBE growth using TDMAAs started in March 1993. In the new location, we were able to use the full range of source chemicals, including TDMAAs, TDMAP, and TBP, for CBE and laser-CBE of III-V compound semiconductors.

2.2 Laser and Optics

Since Ar ion laser has the advantage of smaller in size and easier to operate than an excimer laser, and two Japanese research group[2.1-3] have already shown Ar ion laser-assisted growth is a viable technique for selective-area growth, we chose Ar ion laser as our external energy source. The Coherent argon ion laser was purchased in March 1991, and was operational in June 1991. The laser has a 5 W maximum output with multiple

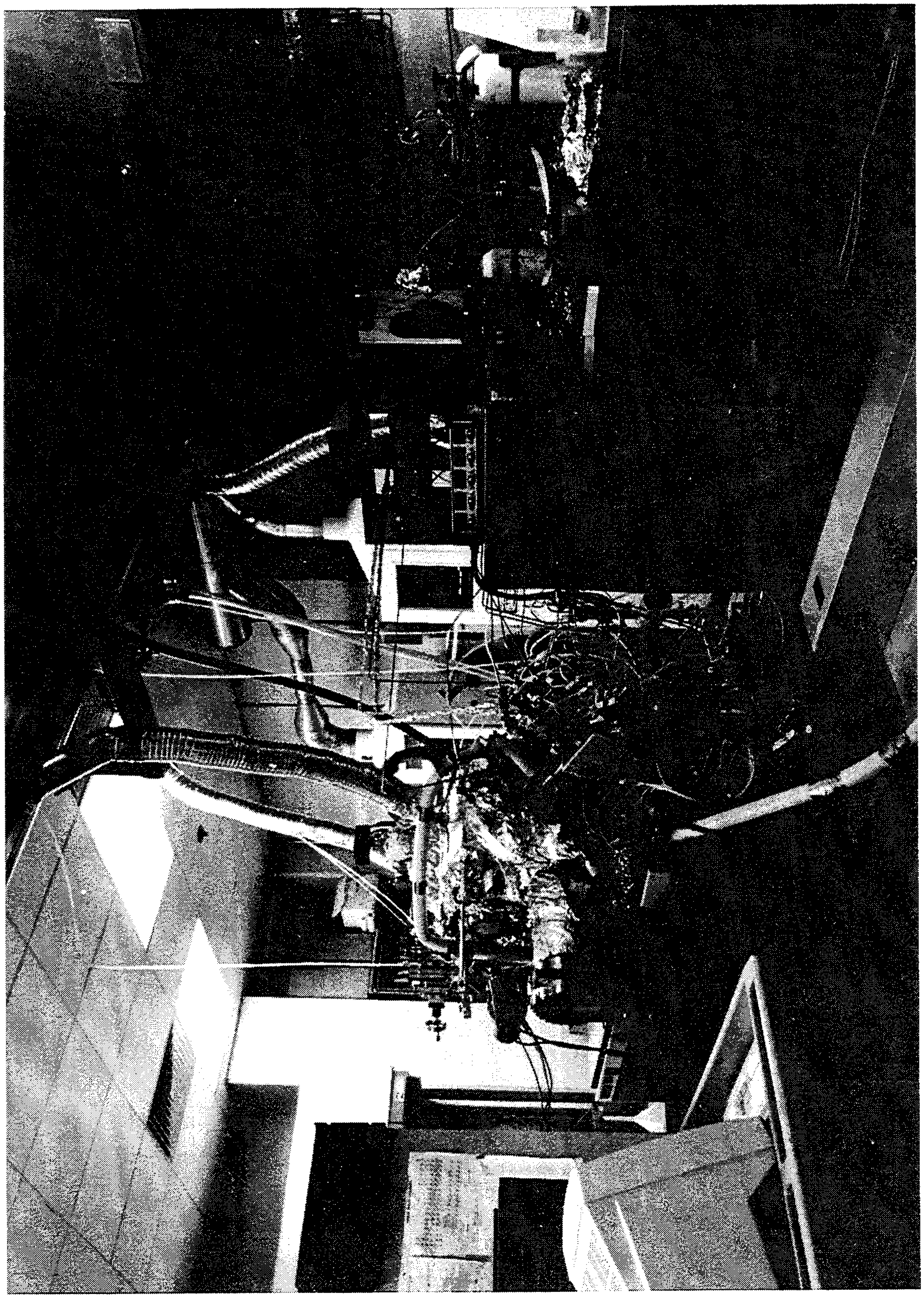

Fig. 2.1 Laser-assisted CBE system.

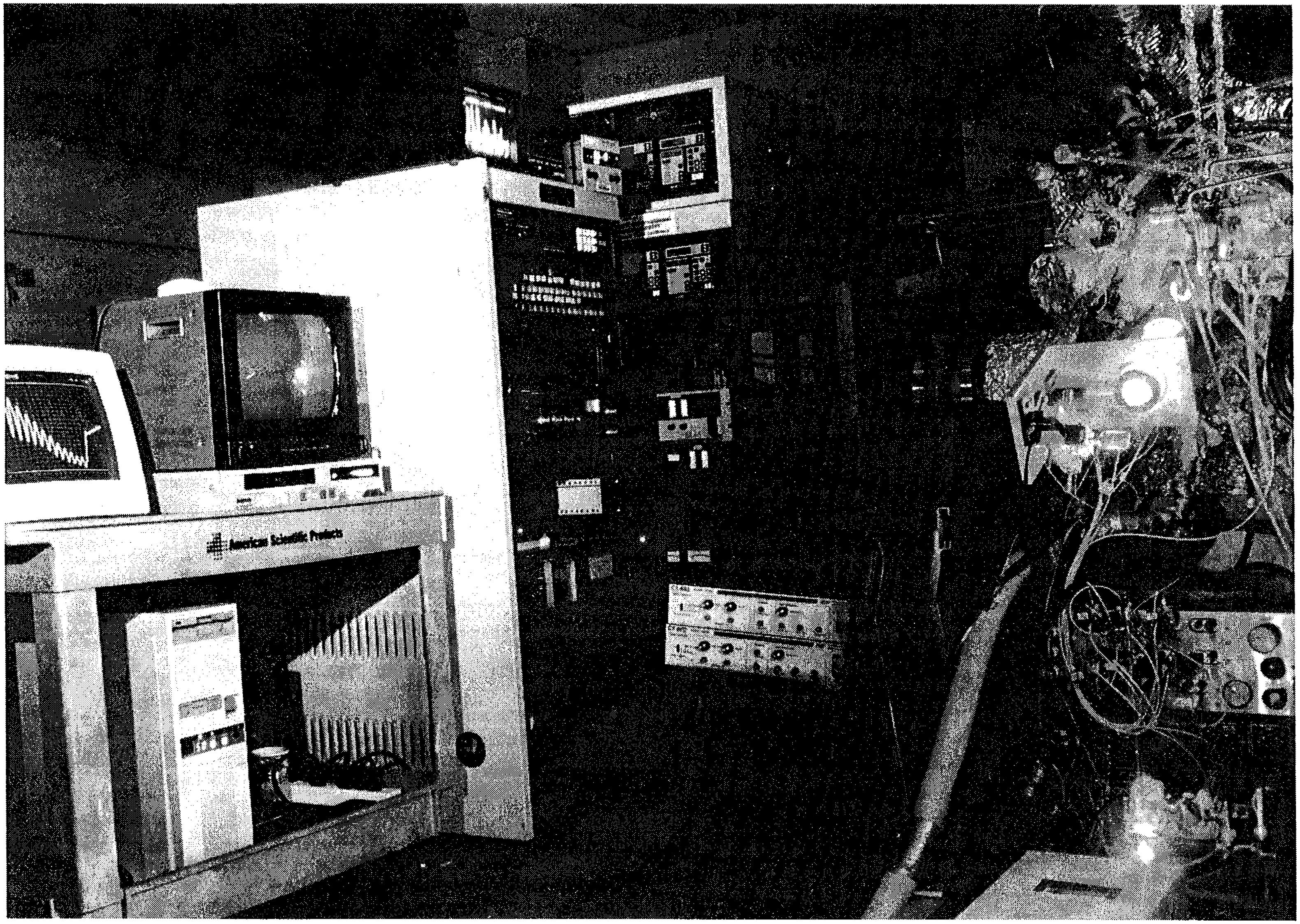
American Scientific Products

Fig. 2.2 CBE system and its control panel.

visible lines, but single-wavelength operation can also be selected. The UV output from this laser was implemented in June 1994, by adding a UV reflector and an output mirror. The step-motor-driven mirrors were first used to scan the laser beam and make line patterns. However, the scan rate was limited by the step-motor, only 2 cm/sec, and a square pattern was difficult to obtain. Therefore, we bought galvanometer-controlled mirrors, which have a scan frequency of up to 100 Hz and are very suitable for pattern scanning. The laser-beam path is clearly shown in Fig. 2.3. In fact, during the laser-assisted-growth experiment the beam path is covered by an aluminum shield for eye-protection.

2.3 Gas Manifold

There are basically three methods of controlling gas flows into the CBE growth chamber in our system. We use vapor-source mass flow controllers for group III alkyls to regulate the gas flow from a bubbler where the upstream vapor pressure is kept constant with a recirculating thermobath. For group V sources, in particular TDMAAs, we use normal mass flow controllers to regulate the flow of a carrier gas, hydrogen, through a bubbler to achieve a wider range of group V flux. For doping sources, we rely on an accurate control of the pressure behind a leak valve using a Baratron pressure sensor because mass flow controllers are unstable at very low range of full scale.

A schematic drawing of the laser-assisted CBE system is shown in Fig. 2.4. Separate gas lines for TEGa, TMIn, trimethylaluminum (TMAl), TDMAAs, tris-dimethylaminophosphine (TDMAP), tertiarybutylphosphine (TBP), CI_2H_2, and Si_2H_6 were installed in the system.

TEGa, TMIn, TMAl are introduced into the growth chamber without any carrier gas through the home-made run/vent system, and their flow rates are controlled by MKS 1150B vapor-source mass flow controllers. Two separate gas injectors inside the chamber

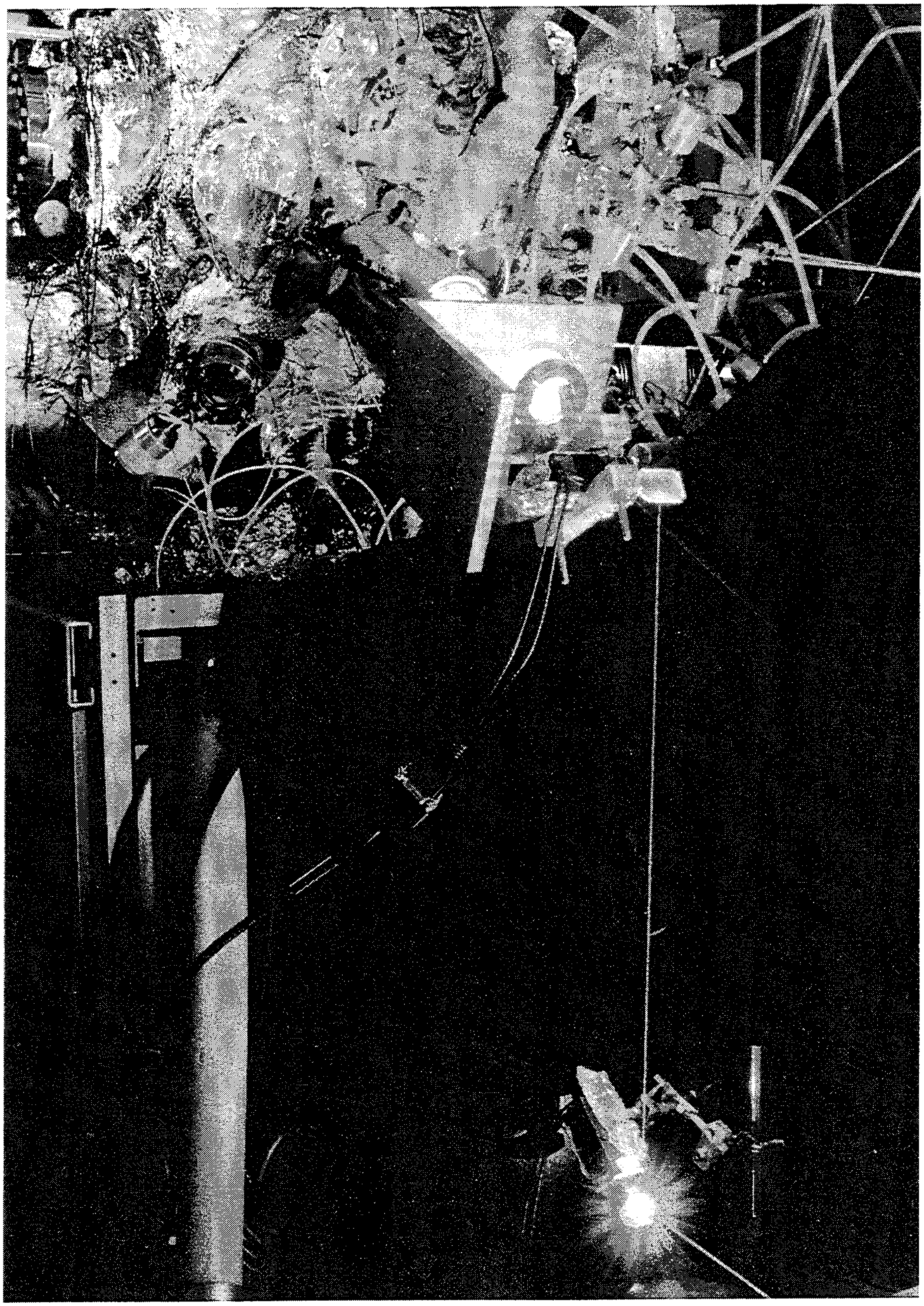

Fig. 2.3 Ar ion laser beam path.

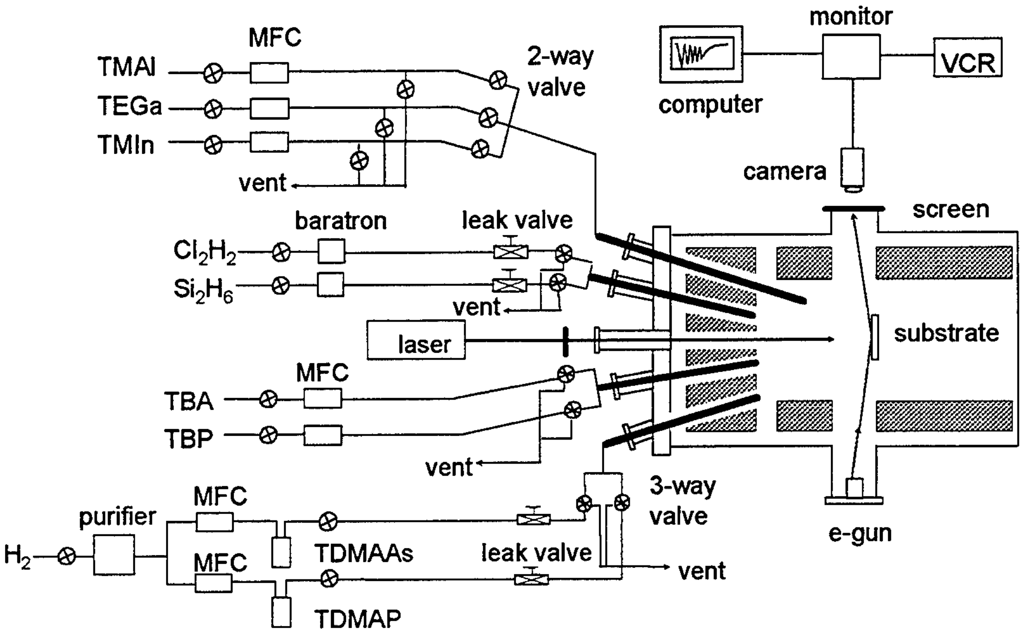

monitor
MFC
TMAl
TEGa
TMIn
2-way
valve
VCR
computer
vent
camera
baratron
leak valve
screen
Cl_2H_2
Si_2H_6
vent
laser
substrate
MFC
TBA
TBP
vent
purifier
MFC
3-way
valve
H_2
MFC
TDMAAs
leak valve
vent
e-gun
TDMAP

Fig. 2.4 The schematic drawing of the laser-assisted CBE system.

are used to direct gas molecules to the substrate and are kept at about 50°C to prevent condensation. Since the vapor source mass flow controller is very sensitive to the upstream vapor pressure, Lauda recirculated thermobaths are used to keep the bubblers at a constant temperature, and the gas lines are also maintained at a temperature 5°C higher than that of the bubblers.

TDMAAs, with a vapor pressure of about 1.35 Torr at 20°C, is carried by hydrogen and injected into the chamber through a leak valve, and it can be precracked by a home-made gas cracking cell. The TDMAAs flow is determined by the hydrogen flow rate, which is controlled by a Unit mass flow controller. Ultra-high purity (99.9999%) hydrogen is further purified by a hydrogen purifier. TDMAP has a similar gas introduction method as TDMAAs. However, due to the higher vapor pressure of TBP, it is directly introduced into the chamber without any carrier gas and its flow is also controlled by a Unit mass flow controller. A more detailed gas manifold for group-V sources is shown in Fig. 2.5 and 2.6. Emergency shutoff valves are incorporated into the gas lines for safety consideration, and nitrogen isolation valves are installed to purge the line after growth.

High-purity (99.999%) CI_2H_2, with a 25°C vapor pressure of about 1.5 Torr, is delivered into the chamber through an ultrahigh vacuum leak valve, and its flux is adjusted using a Baratron pressure sensor. 15% Si_2H_6 (mixed with hydrogen) is introduced into the chamber through an ultrahigh vacuum leak valve, and its flux is controlled by a Unit mass flow controller. Three-way valves are used for run/vent in handling all the group V and doping sources, and a mechanical pump is used for the vent line. Since the mechanical pump can only maintain a pressure in the 10^{-2} Torr range while our growth pressure is at a pressure between 10^{-5} and 10^{-4} Torr, the run/vent switching produces a flow transient, which normally lasts for about 4-5 seconds. A turbomolecular pump with nitrogen purge to its bearings or a diffusion pump which a liquid-nitrogen trap would be suitable for handling metalorganic gases in the vent line.

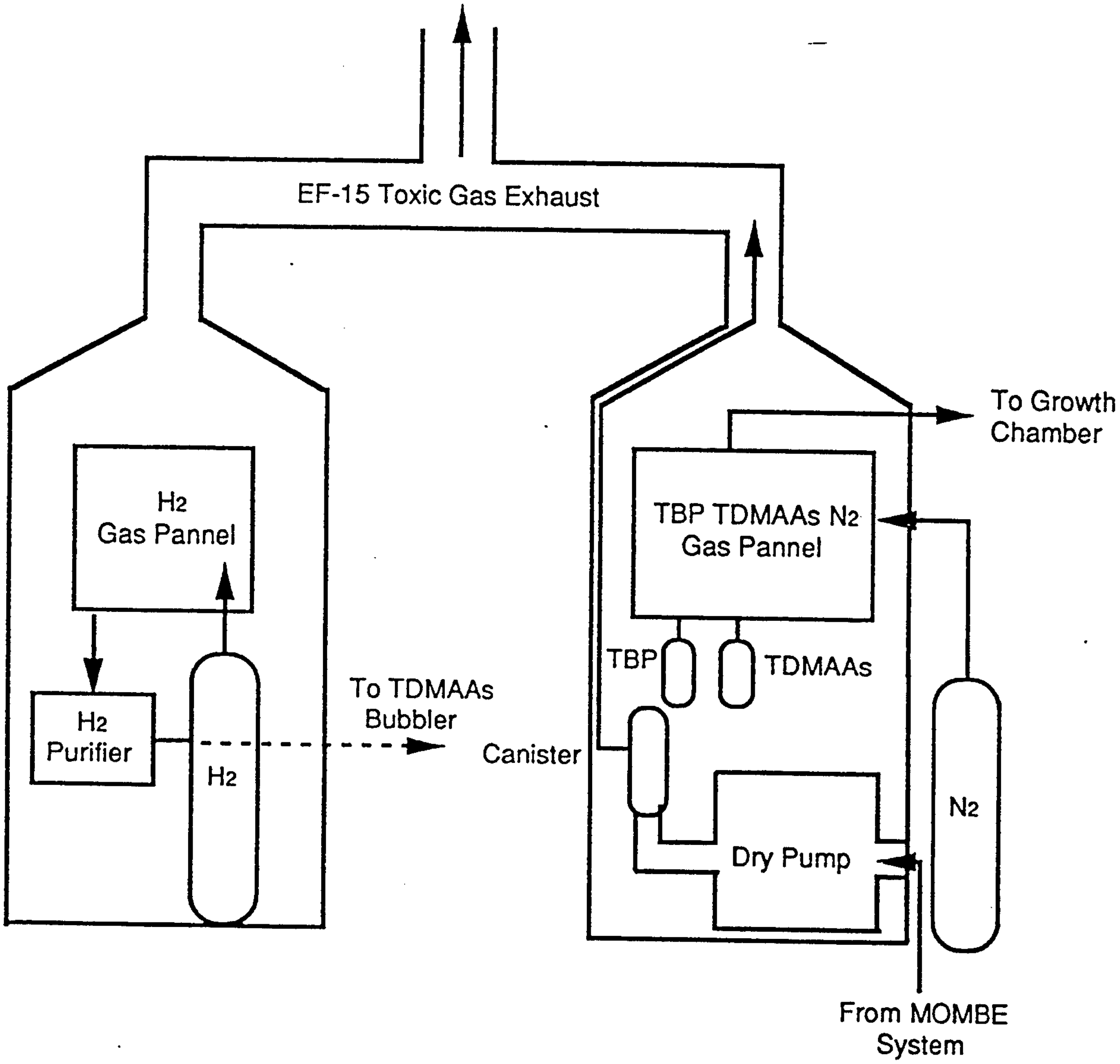
EF-15 Toxic Gas Exhaust
H2
Gas Pannel
H2
Purifier
H2
To TDMAAs
Bubbler
Canister
TBP TDMAAs N2
Gas Pannel
To Growth
Chamber
TBP
TDMAAs
Dry Pump
N2
From MOMBE
System

Fig. 2.5 TDMAAs, TBP, and hydrogen gas cabinets.

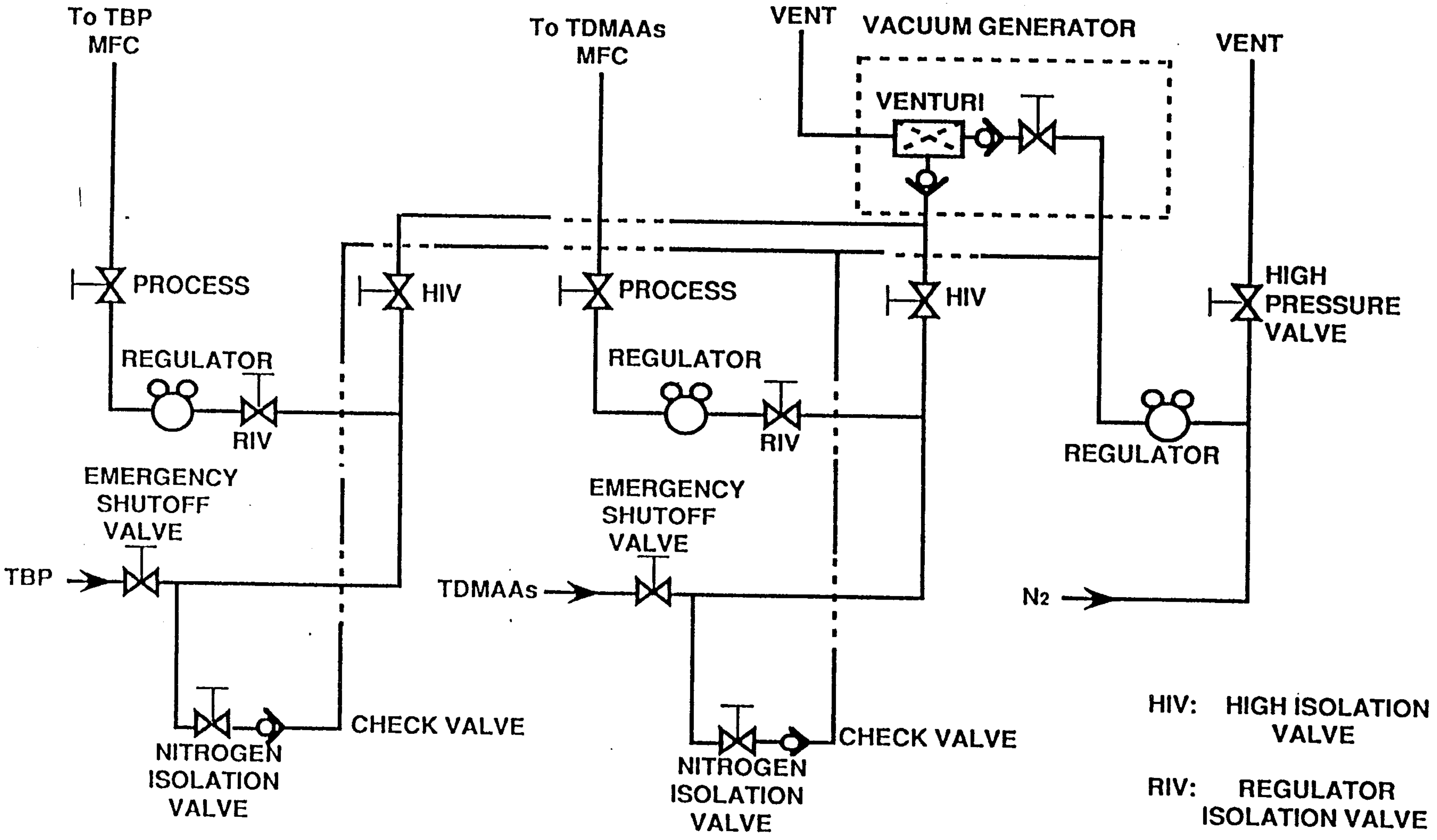
To TBP MFC
To TDMAAs MFC
VENT
VACUUM GENERATOR
VENT
VENTURI
PROCESS
HIV
PROCESS
HIV
HIGH PRESSURE VALVE
REGULATOR
REGULATOR
REGULATOR
RIV
RIV
EMERGENCY SHUTOFF VALVE
EMERGENCY SHUTOFF VALVE
TBP
TDMAAs
N_2
NITROGEN ISOLATION VALVE
CHECK VALVE
NITROGEN ISOLATION VALVE
CHECK VALVE
HIV: HIGH ISOLATION VALVE
RIV: REGULATOR ISOLATION VALVE

Fig. 2.6 TDMAAs and TBP gas panel.

2.4 Growth Chamber

2.4.1 Pumping and pressure measurement

The growth chamber is evacuated by a Balzers 1600 l/s turbomolecular pump, yielding a base pressure of 3×10^{-9} Torr. The picture of the pump system is shown in Fig. 2.7. The pump is interlocked to pressure in the growth chamber and in the mechanical pump, water flow, and power loss. If any problem happens, the gatevalve between the pump and the growth chamber and the valve between the turbopump and the mechanical pump will automatically close. The vent valve of the turbopump will open and fill the turbopump compartment with nitrogen.

Since metalorganic molecules tend to corrode hot filaments, an ion gauge is not suitable for pressure measurement, which has been proved by our experience. We use a Balzers cold cathode gauge in our growth chamber for pressure measurement. It is stable and easy to fix.

2.4.2 RHEED

In order to facilitate *in situ* growth monitoring at low substrate temperature and with laser-assisted growth, we set up a computer-controlled video-camera RHEED system. A schematic is shown in Fig. 2.8. The system hardware consists of the following:

PC: 486DX, 50 MHz, 8 Mb RAM, 200 MB hard drive, SVGA monitor, mouse
CCD monochrome camera: Sony SSC-M256
Frame Grabber: TARGA+
Computer controlled VCR: Panasonic AG-7355
Video monitor: Panasonic S1360
Software: RIP (rest in peace), Foxpro support executable, TARGA+ setup utility/batch file.

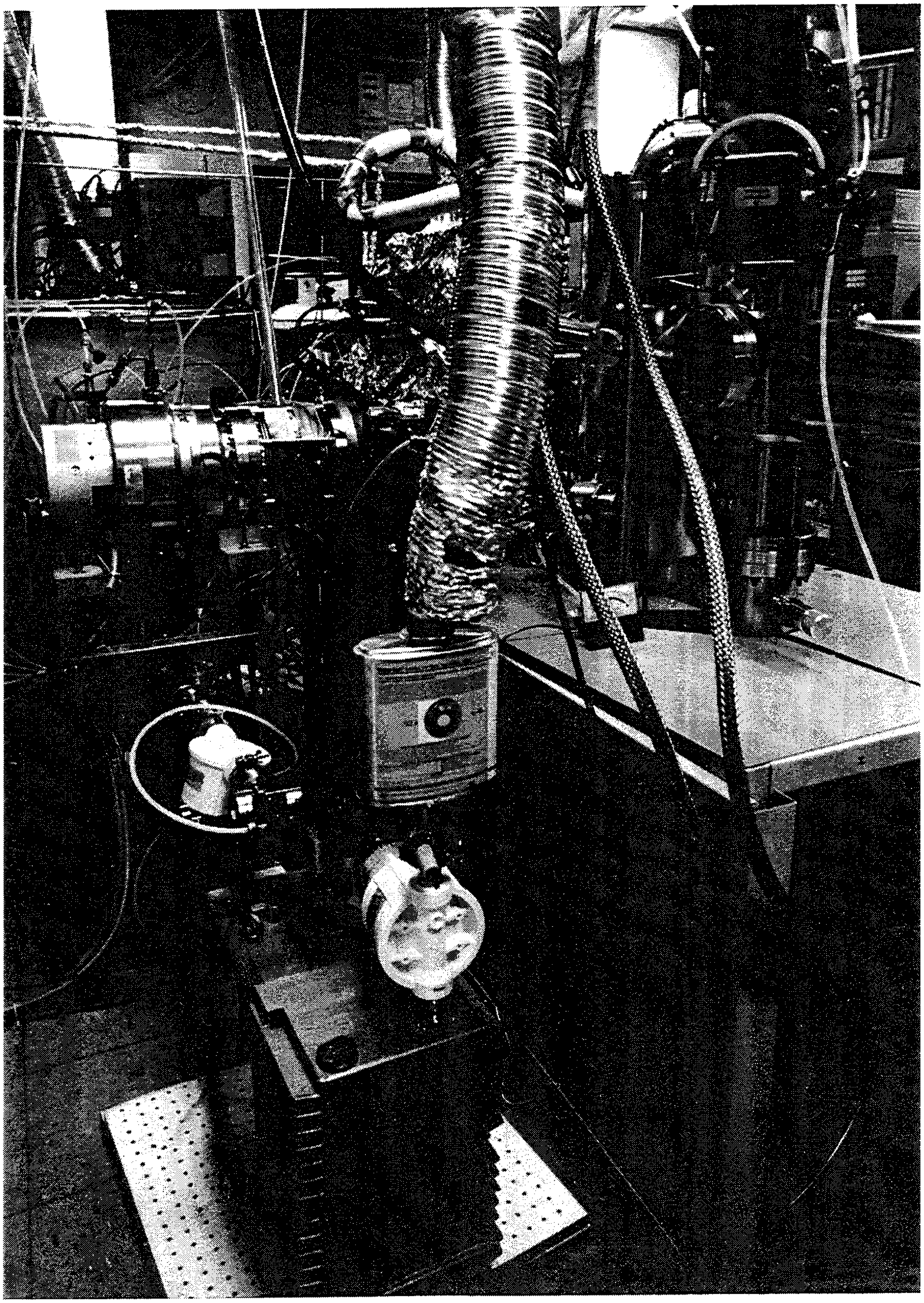

Fig. 2.7 The turbomolecular and mechanical pump system.

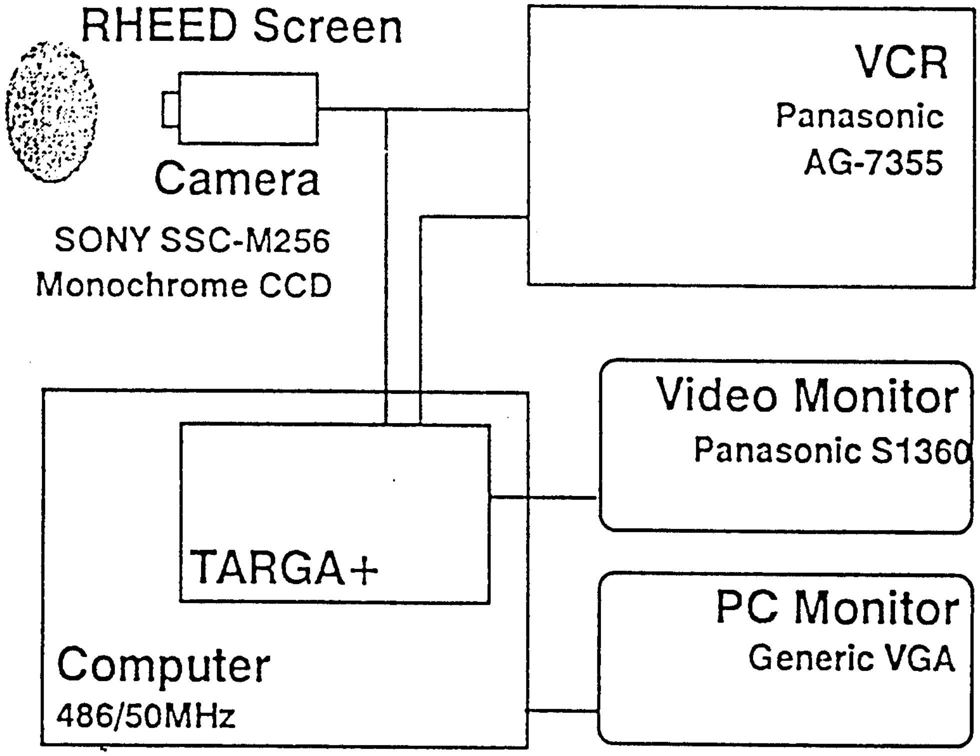
RHEED Screen
Camera
SONY SSC-M256
Monochrome CCD
VCR
Panasonic
AG-7355
Video Monitor
Panasonic S1360
TARGA+
Computer
486/50MHz
PC Monitor
Generic VGA

Fig. 2.8 The schematic drawing of the RHEED system.

An undergraduate engineering aid set up the hardware and wrote the control and analysis program. Five options are presented by this setup: video control, calibration, object definition, data acquisition, and analysis. Through video control, we can choose one of three display modes: live video, stored image, and a combination of the two. Calibration allows us to convert distance in an image to physical distance on the RHEED screen. We can define one of the following object types: intensity field (average intensity inside a definable rectangular region), tracked intensity field (the rectangular region is tracked with the RHEED spot to take into account wobbling during substrate rotation or drift in the electron beam), image field (average intensity and actual image in a rectangular region), tracked image field, line (intensity profile along a line), intensity line (average intensity along a line), and point (intensity at a point). Data acquisition has a real-time or off-line mode. For analysis, we have time series analysis, profile analysis, and image analysis. Data smoothing can be done by either Kaiser-Bessel filter or Savitzky-Golay filter.

Using this RHEED setup, we are able to perform group III- and group V-induced RHEED intensity oscillations very easily. We can also easily store RHEED images in the computer for more detailed studies later.

2.4.3 Mass spectrometer

A Dycor mass spectrometer is used in our growth chamber for analyzing different gas species and for leak checking. Another undergraduate engineering aid wrote a PC program for controlling the mass spectrometer and data acquisition. We can store mass spectra in the computer, instead of just printing out from the spectrometer controller. We can also select several channel and monitor ion currents at several mass numbers as a function of time. As we shall see later, the mass spectrometer is very useful in our gas cracking study of TDMAAs.

2.4.4 Computer-controlled growth operation

We have developed the hardware and software for controlling the shutter/valve operation and mass flow controllers. The software has the flexibility of both gas- and solid-source configuration. A solid source requires the control of only a single shutter, while a gas source requires the control of three independent gas valves (upstream, run, and vent). Besides these digital control lines, there are analog lines, which provide a voltage from zero to five volts for controlling mass flow controllers. Using a menu-driven recipe compiler, we can define whatever steps and procedures that are needed to grow a certain structure, especially quantum-well structures.

2.5 Safety Handling

2.5.1 Group V sources

Safety is a crucial issue in the development of a CBE system. Due to their extremely high toxicity and high vapor pressure, the hydrides, arsine (AsH_3) and phosphine (PH_3), are very difficult to handle. In our laser-assisted CBE system, TDMAAs and TBP were chosen as the group-V precursors to minimize hazard. The toxicity testing of TBP indicates that the LC_{50} (concentration in air when inhaled for 4 hours that will result in death of 50% of exposed animals) is in excess of 1100 ppm. However, there is no data on LC_{50} for TDMAAs as it is a relatively new source. Nevertheless we expect TDMAAs to have much lower toxicity than AsH_3 because it has no direct As-H bonds, which are believed to introduce the strongest toxic function. Table 2.1 summarizes the toxicity data for TDMAAs, AsH_3, TBP, and PH_3. It is clear that we should take extreme care while handling these gases.

Table 2.1 Toxic data of group-V precursors

	TDMAAs	AsH_3	TBP	PH_3
Properties	Colorless liquid with strong smell of amine	Colorless gas with garlic-like odor	Colorless, clear volatile liquid; stench	Colorless gas with rotten-fish odor
Toxicity	Fatal if inhaled.	Extremely toxic.	Fatal if inhaled.	Fatal if inhaled.
Fire Hazard	Flammable	Flammable; pyrophoric	Very flammable; pyrophoric with auto-ignition at 54.5°C; burns with highly toxic PO_x fumes	Very flammable; pyrophoric with auto-ignition at 40-50°C; burns with highly toxic PO_x fumes
LC_{50}	Unknown.	5-40 ppm	> 1100 ppm	11 ppm
Pressure	1.5 Torr	205 psi	250 Torr	600 psi
Treatment	Prompt medical attention is vital.			

2.5.2 Group III metalorganics

Most of the metalorganic group-III alkyls, e.g., TEGa, TMIn, TMAl, are believed to be far less toxic than the hydrides and As- or P-containing metalorganics, and the exposure times are generally not available. All of the metalorganics used in CBE are pyrophoric and react violently with water. Therefore, alkyl fires should not be treated with water. The safe way to deal with an alkyl fire is to use a smothering agent like vermiculite. The laboratory where the laser-CBE system is located has a smoke detector in case there is a fire.

2.5.3 Exhaust scrubbing and monitoring

All gas tubings are made of electronic-polished stainless steel. They have been helium-leak-checked under vacuum and pressurized-leak-checked with nitrogen (150% working pressure for 24 hours). The gas panel is well designed so that the number of joints is minimized (4 VCR connections on the panel). All gas tubings are covered with a hose under negative pressure. All the gas supply and exhaust lines are housed in gas cabinets or ducts, which are connected to a ventilation system (EF-15) separate from the other building exhaust systems. EF-15 is equipped with an emergency power back-up.

All gases that come from the CBE system which may possibly contain trace amount of toxic gas will pass through two charcoal canisters (GMC SS1) before being exhausted. The gas concentration at the end of the toxic gas scrubber is monitored continuously by an MDA-16 toxic gas monitor. The schematic of sampling points for the MDA system is shown in Fig. 2.9. Eight alarm bells and yellow strobe lights are connected to this monitor. The concentration, if any, of TDMAAs and TBP are printed out every eight hours. For safety, the alarm levels of TBP and TDMAAs in the MDA system were set the same as those of AsH_3 and PH_3, which are shown in Table 2.2. If the toxic gas level at any point is higher than the first level, the MDA will close all gas valves, and the first level alarm inside the lab, a buzzer, will be triggered. In this instant, the personnel in the lab are instructed to evacuate. If the toxic gas level is higher than the second level, a second alarm in the service corridor will be triggered, and the operator is instructed to follow the safety manual to decide whether the building should be evacuated.

Table 2.2 Alarm levels of TDMAAs and TBP

	TDMAAs	TBP
First level alarm	25 ppb	150 ppb
Second level alarm	100 ppb	600 ppb

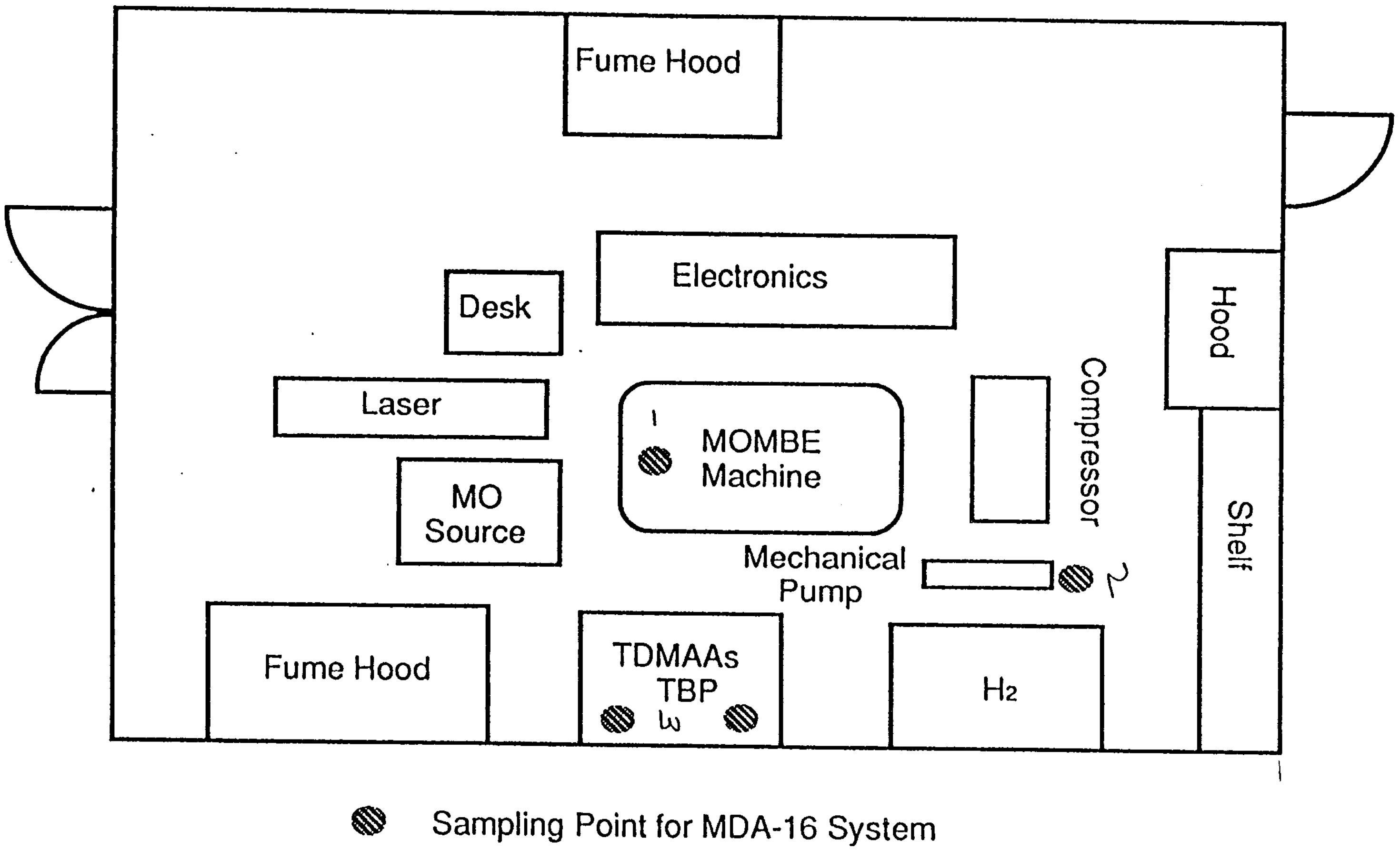
Fume Hood
Electronics
Desk
Laser
MO
Source
1
MOMBE
Machine
Compressor
Hood
Shelf
Mechanical
Pump
2
Fume Hood
TDMAAs
TBP
3
H2
Sampling Point for MDA-16 System

Fig. 2.9 The schematic drawing of sampling points for the MDA-16 system.

2.6 Temperature Measurement by Infrared Laser Interferometry

A precise temperature control during growth of thin films is necessary for optimizing the material characteristics. Thermocouples and optical pyrometers are widely used to measure the substrate temperature. Although accurate, the thermocouple needs to be in direct contact with the sample. One can avoid this problem by placing the thermocouple very close to the substrate holder. However, this method usually generates an uncertainty of ±40°C in an MBE system[2.4] due to radiation from the heater and reflection of radiation from the back of the substrate holder. On the other hand, the optical pyrometer is contactless and needs only the thermal radiation of the target[2.5-7]. Unfortunately, the pyrometer registers its signal from the absolute infrared (IR) radiation intensity, so the pyrometer cannot work for temperatures below 500°C. Furthermore, any coating on the viewport during growth or the existence of any other radiative sources within the growth chamber will decrease the accuracy of the detection[2.8, 2.9].

Recently a contactless IR laser interferometry method was demonstrated to overcome the above problems in MOCVD and MBE growth of semiconductors[2.9-13]. This technique is particularly useful for us because laser-assisted MOMBE operates at low substrate temperatures. In our work we have used this technique to calibrate the substrate temperature from 25°C to 550°C and measure the temperature increase due to Ar^+ laser irradiation[2.14].

2.6.1 Principle of operation

An optical reflection will result upon the encountering of a difference in the refractive index. Because our samples are double-side-polished, both the front and the rear surfaces will act as reflective planes. The reflected beams from both the front and the back surfaces of the wafer result in interference. The physical illustration of laser interferometry is shown in Fig. 2.10. For normal incidence, the phase difference between both reflected beams (R_1 and R_2) will be

$$\Phi = 2\pi\cdot(2/\lambda)\cdot n_2\cdot L$$

Where λ is the free space wavelength of the laser; n_2 the refractive index of the substrate; and l its thickness. We chose an infrared laser (λ = 1.15 mm) so that the substrate is transparent. Φ by itself has no significance, but it is its variation ($\Delta\Phi$) with respect to the temperature change (ΔT) that is important to our experiment. Since the change in substrate thickness due to thermal expansion is much smaller than λ, the effect of the temperature dependence of n_2 dominates. Therefore,

$$\Delta\Phi \approx (2\pi\cdot\frac{2}{\lambda}\cdot L)\cdot\Delta n_2$$

As Δn_2 increases with temperature, $\Delta\Phi$ varies as well. Therefore, by keeping track of the number of maxima and minima on the interference pattern, one can find $\Delta\Phi$ and then the actual temperature variation (ΔT) away from the reference temperature (T_0).

2.6.2 Substrate temperature calibration

Since the actual temperature dependence of n_2 and l are too complicated to be described analytically, a theoretical prediction of $\Delta\Phi$ as a function of ΔT is not feasible. Therefore, we calibrated the dependence of $\Delta\Phi$ on ΔT experimentally (the dependence of the interferometric fringe number ΔN versus the change in sample temperature T_S) in an annealing furnace where a known, uniform temperature could be maintained. The measurement setup is shown in Fig. 2.11. A double-side-polished GaAs (500 μm thick) or InP (300 μm thick) substrate was clamped onto a sample holder and positioned at the center part of the annealing furnace. A 1.15-μm He-Ne laser was directed to the wafer at normal incidence, and the reflected beam was detected by a photodiode. The signal was amplified by our home-made amplifier circuit, and the interferogram was recorded by a plotter. A Chromel-Alumel thermocouple (with the reference junction kept at 0°C in a

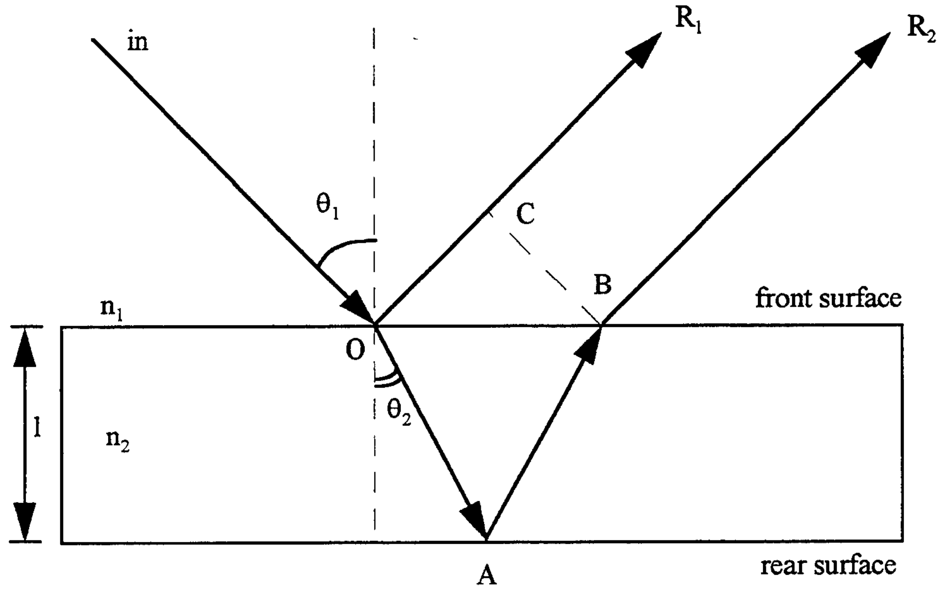
in
R1
R2
θ1
C
B
front surface
n1
O
θ2
l
n2
A
rear surface

Fig. 2.10 The physical illustration of interferometry.

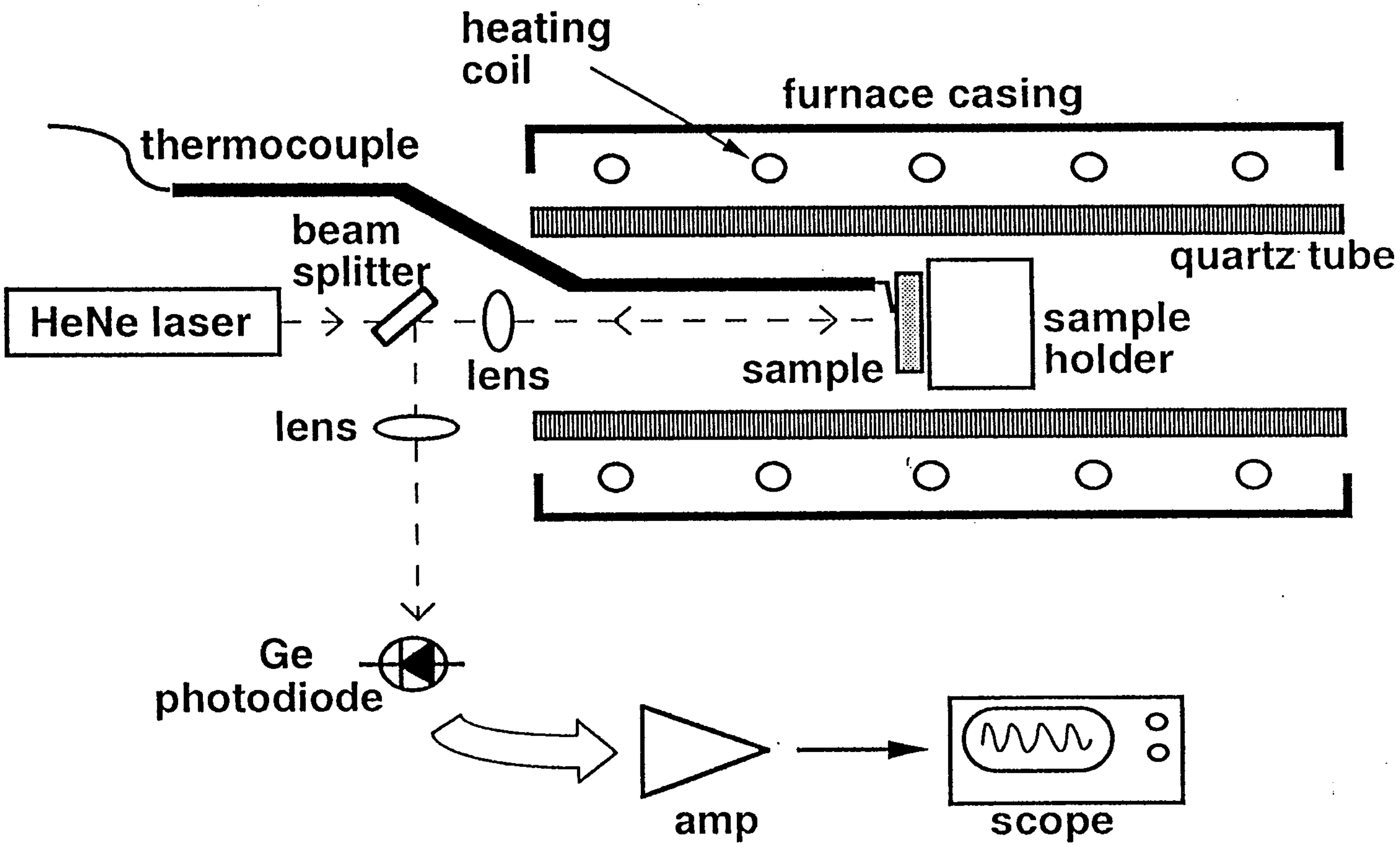
heating
coil
furnace casing
thermocouple
beam
splitter
HeNe laser
lens
lens
quartz tube
sample
sample
holder
Ge
photodiode
amp
scope

Fig. 2.11 The infrared laser interferometry setup in an annealing furnace.

constant-temperature bath recirculator) was attached to the sample surface within 2 mm from the laser spot. The thermocouple was in good thermal contact to the laser irradiated area of the substrate. The thermocouple readout was also compared with the thermometer readout and their difference was within ±0.1°C. The heating rate was kept at lower than 10°C per minute in order to get high accuracy.

Fig. 2.12 shows an interferogram trace obtained from our experiment. Notice that the signal level goes through a complete cycle for a temperature increment of approximately 2.8°C. This method is thus capable of detecting a temperature change of ±0.7°C. The results of interferometric fringe number (ΔN) versus sample temperature (T_S) in °C are plotted as shown in Fig. 2.13. Since both phosphorous and arsenic desorbed from the samples at high temperature which result in a rough surface, our calibration runs could only reach up to 550°C. For each temperature calibration curve, a third order polynomial was fitted:

for GaAs: $T_S = 22.640 + 2.775\times\Delta N - 5.8\times10^{-4}\times\Delta N^2 - 4\times10^{-6}\times\Delta N^3$,

for InP: $T_S = 18.692 + 3.024\times\Delta N - 4.25\times10^{-3}\times\Delta N^2 + 1\times10^{-5}\times\Delta N^3$.

The same samples were later mounted on a molybdenum holder and tested in a MBE growth chamber. At each manual power setting, the substrate heater heated the sample up to $T_0+\Delta T$ (T_0 is the reference temperature, about 22°C) and the interferogram was recorded. After the interferogram had stabilized, a slightly higher heating power was set, and the same detection cycle would repeat. A certain number of oscillations of the reflectance signal corresponds to a certain temperature change ΔT of the substrate. The substrate temperature was determined by adding the temperature change deduced from the reflectance signal to the initial reference temperature T_0. According to the calibration between the substrate temperature T_S and the fringe number ΔN, obtained in the annealing furnace, the substrate temperature as a function of the substrate heating power (percentage of the total output) could be calibrated, as shown in Fig. 2.14. Using this method, we found that different molybdenum substrate holders would give a little different

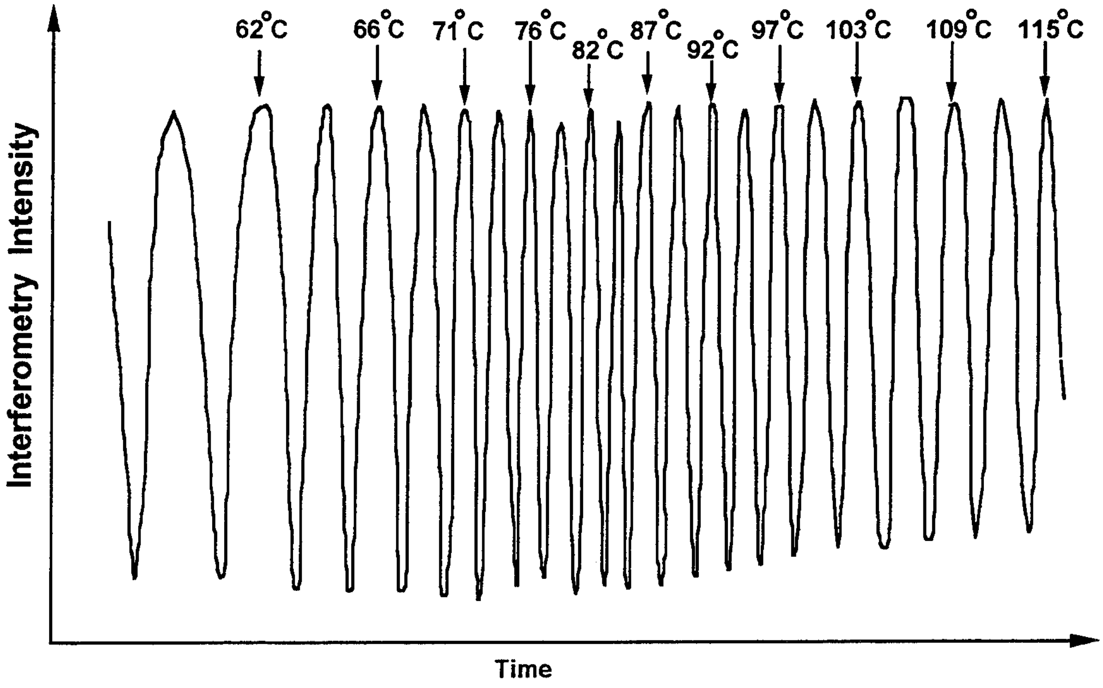

Fig. 2.12 Interferogram of a 500-micron-thick GaAs sample by 1.15 μm He-Ne laser inside an annealing furnace.

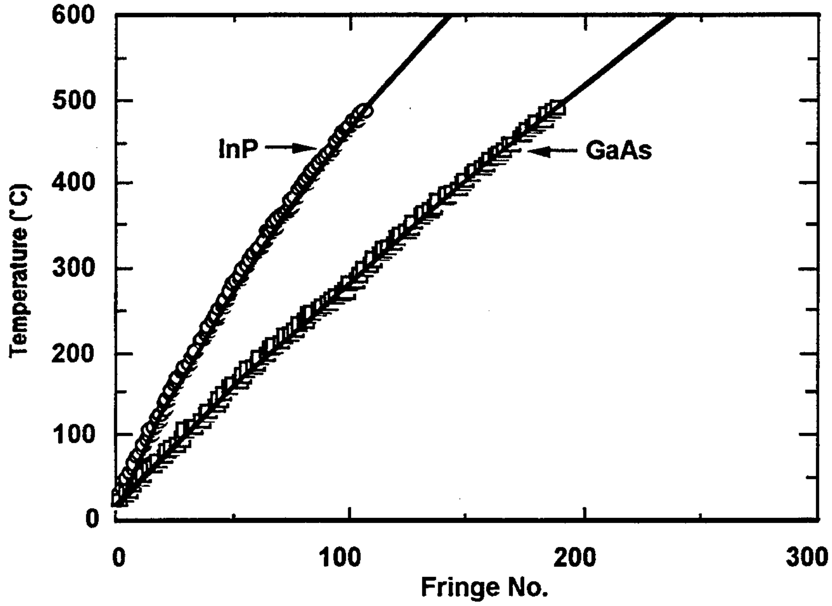

Fig. 2.13 Temperature calibration curves for GaAs and InP samples by IR laser interferometry in an annealing furnace.

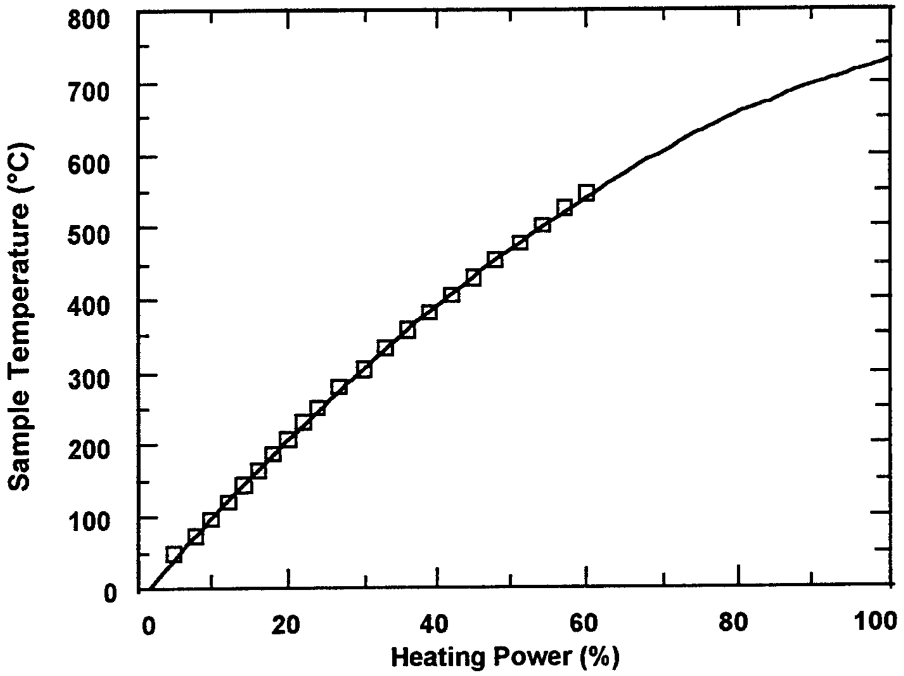

Fig. 2.14 Substrate heating power versus sample temperature calibrated in MBE growth chamber.

substrate temperature for the same substrate-heater power setting because of their different radiation reflectivity. Other growth conditions were also examined using this method.

(1) Without applying any heating power, the introduction of liquid N_2 effectively brought the sample temperature 35°C to 40°C below the room temperature. After the heating power was turned on, the samples could reach the same final temperature but after a longer time.

(2) Because of its relatively low furnace temperature (~300°C), the opening of the arsenic source shutter had almost no effect on the substrate temperature. On the other hand, due to its high furnace temperature (~1000°C), the opening of the Ga source shutter caused a temperature increment of about 10°C on the sample.

In order to facilitate the experimental procedure for routine temperature calibration, we developed an optical fiber-coupled laser interferometric system. The schematic is shown in Fig. 2.15. The experiment data were taken and analyzed by a computer. This improvement shortens the time for setup and alignment significantly.

2.6.3 Measurement of Ar ion laser-induced local heating

An Ar^+ laser (multiline mode) focused to a spot size of 400 μm was irradiated onto a GaAs substrate as shown in Fig. 2.16. Although the He-Ne laser was incident 5° away from the normal of the sample surface, it merely introduced an error of 0.38% which is acceptable. An insulation layer (a double-side masking tape) was placed between the sample and the sample holder. If an indium solder was used to secure the sample onto the sample holder, a temperature gradient would result across the sample thickness while the Ar^+ laser was on (since the thermal mass of the sample holder is much greater than that of the sample itself and the sample holder would work as a heat sink). This would destroy the uniformity of the sample refractive index, and hence degrade the interferogram. The

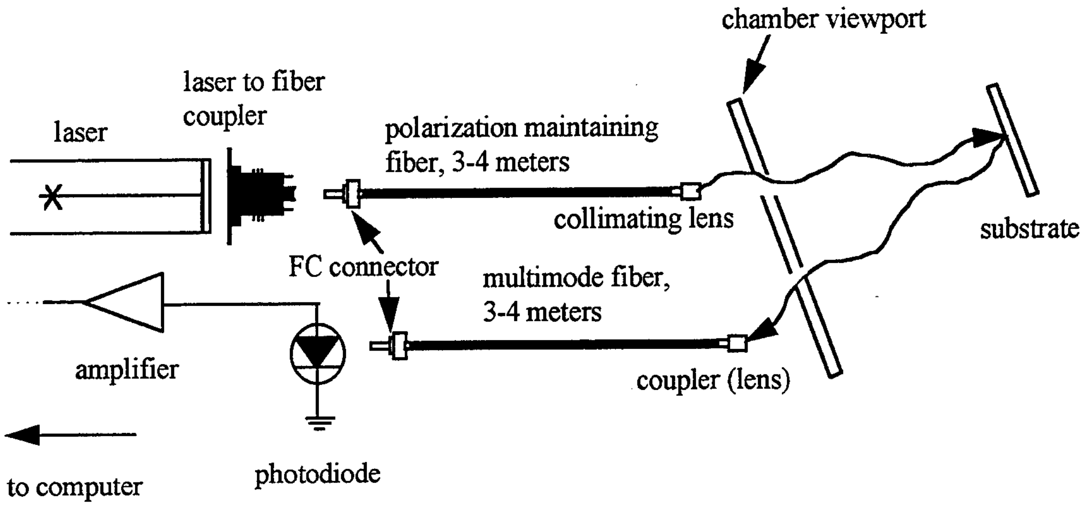
chamber viewport
laser to fiber coupler
laser
polarization maintaining fiber, 3-4 meters
collimating lens
substrate
FC connector
multimode fiber, 3-4 meters
amplifier
coupler (lens)
to computer
photodiode

Fig. 2.15 The schematic drawing of an optical fiber-coupled laser interferometric system.

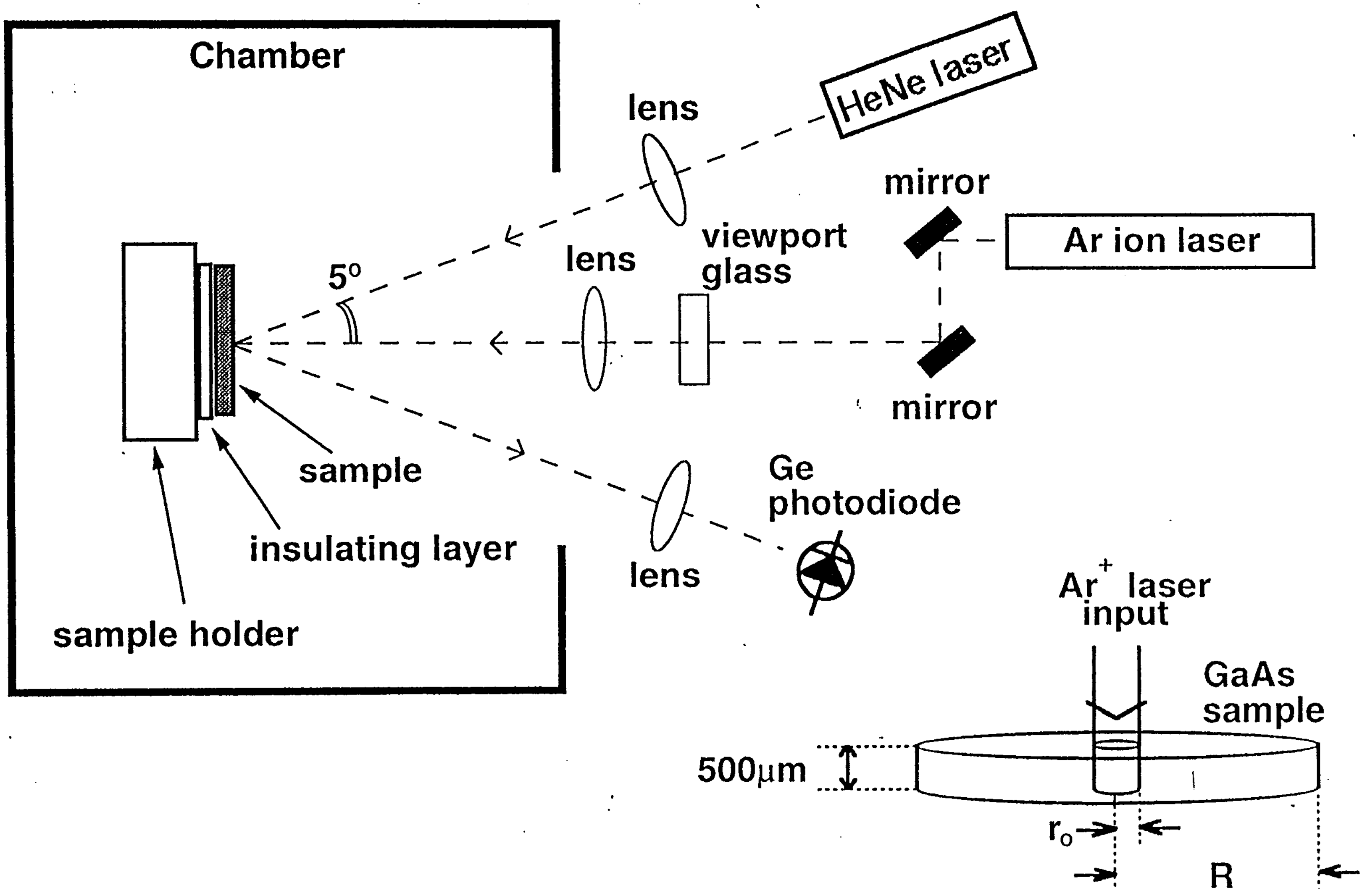
Chamber
HeNe laser
lens
mirror
Ar ion laser
viewport glass
lens
5°
mirror
sample
Ge photodiode
insulating layer
lens
sample holder
Ar^+ laser input
GaAs sample
500μm
r_o
R

Fig. 2.16 Measurement setup of substrate temperature change induced by Ar ion laser heating.

insulation layer was used to prevent this from happening. Nevertheless, both methods of sample attachment (with In and with an insulation layer) were employed, and the results were analyzed.

The interferograms for Ar$^+$ laser induced heating are shown in Fig. 2.17. The top trace was obtained with an insulating layer positioned between the GaAs sample and the sample holder. The bottom trace was obtained with the GaAs sample thermally attached to the sample holder with indium. It is clear how the indium bonding destroyed the interferogram. Our approximation for the surface temperature of the beam spot was based on the top trace, and the data points of the GaAs beam-spot surface temperature and the corresponding Ar$^+$ laser output power are plotted in Fig. 2.18.

To check whether the experiment made sense or not, a theoretical model was developed (see insert of Fig. 2.16) and a few verifying numbers were calculated. If we define T(r) as the front surface temperature at a radius r, then in a cylindrical coordinate, the front surface temperature over the edge of the Ar$^+$ laser beam spot should be$^{2.15}$

$$T(r_o) = T(R) + \frac{Q_{center} \times \ln(R/r_o)}{2 \cdot p \cdot L \cdot k}$$

Where r_0 (Ar$^+$ laser beam radius) = 0.02 cm; R (sample radius) = 0.5 cm; l (sample thickness) = 0.05 cm; k (GaAs thermal conductivity) = 0.4445 Watts/cm·°C; and Q_{center} is the amount of heating power being pumped into the center of the GaAs sample from the Ar$^+$ laser.

At 5 Watts of radiation power from the Ar$^+$ laser, the actual thermocouple measurement gave us T(R) = 106°C (the thermocouple was attached to the sample front surface about 1 mm from the Ar ion laser spot). Furthermore, we found from measurement that the reflectivity of the mirrors is 65.2%; the viewport glass transmittance 82.6%; the lens transmittance 98.5%; and the reflectivity of the polished GaAs front surface 51.5%. Thus, only 25.7% of Ar$^+$ laser power was absorbed in the GaAs sample. Finally, since the absorption coefficient of GaAs at l = 488 nm and 514 nm is about

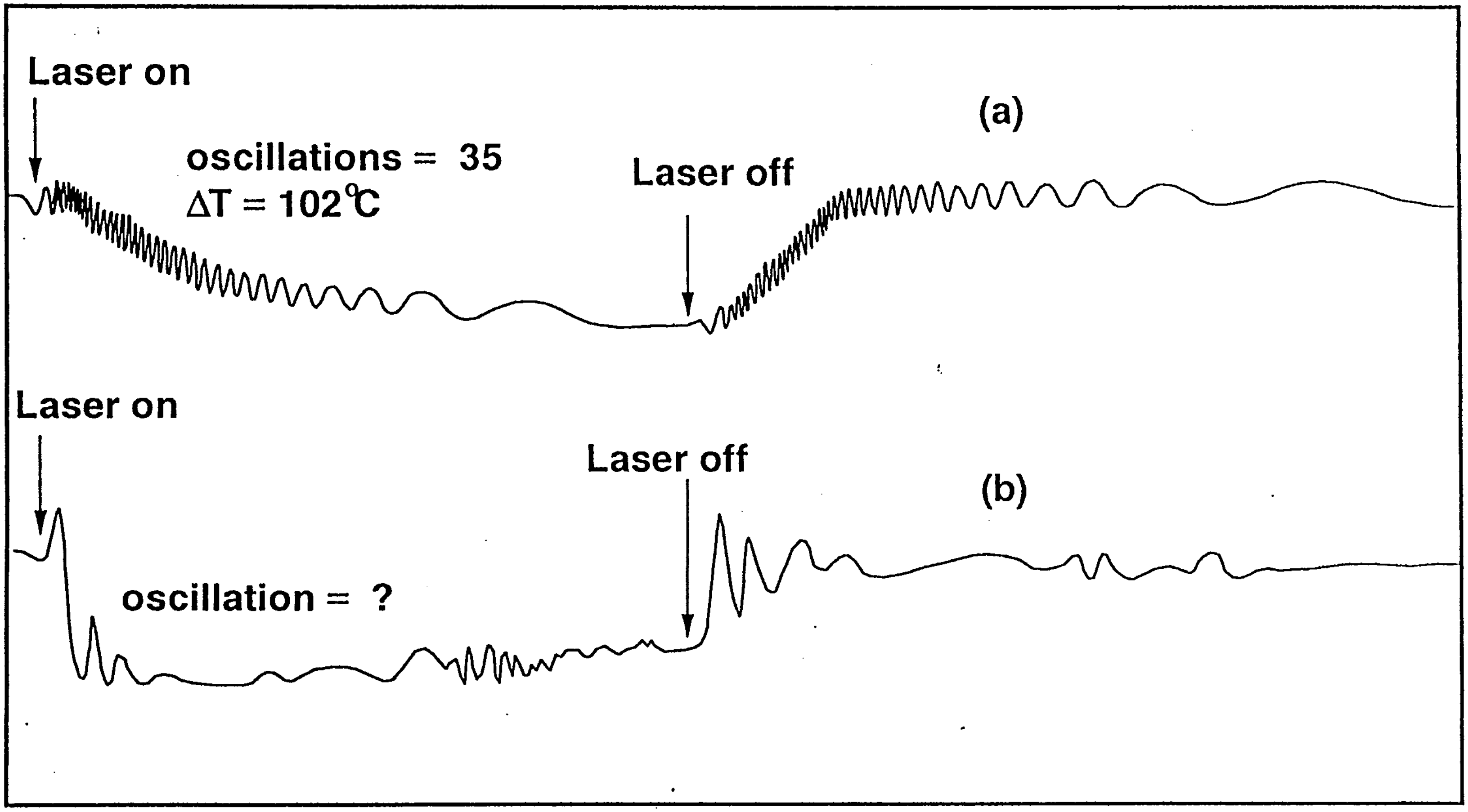

Fig. 2.17 Interferogram of GaAs sample under a 2000 W/cm² Ar ion laser irradiation, (a) without indium attachment and (b) with indium attachment.

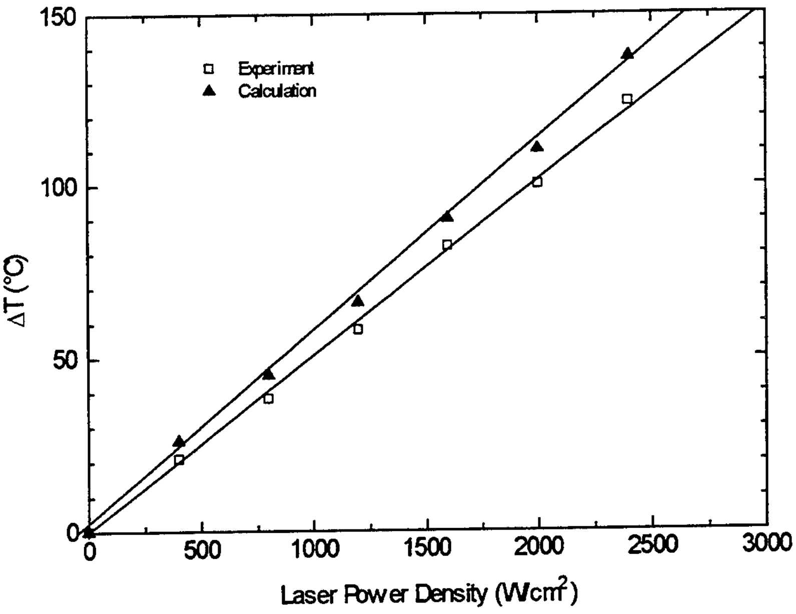

Fig. 2.18 GaAs sample surface temperature increment versus Ar ion laser power input.

8.9×10^4 cm^{-1}, almost all (about 99.99%) of the incident laser energy is absorbed in the 500 μm thick sample. Thus, for a 5-Watt output from the Ar$^+$ laser, we estimate $T(r_0)$ to be 137°C. From the IR interferometry method we found the beam spot temperature to be approximately 124°C, which is in fair agreement with the theoretical value.

2.7 References

2.1 Y. Aoyagi, M. Kanazawa, A. Doi, S. Iwai, and S. Namba, J. Appl. Phys. *60*, 3131 (1986).

2.2 H. Sugiura, R. Iga, T. Yamada, and M. Yamaguchi, Appl. Phys. Lett. *54*, 335 (1989).

2.3 R. Iga, H. Sugiura, T. Yamada, and K. Wada, Appl. Phys. Lett. *55*, 451 (1989).

2.4 C. M. Gronet, J. C. Sturm, K. E. Willians, J. F. Gibbons, and S. D. Wilson, Appl. Phys. Lett. *48*, 1012 (1986).

2.5 W. Heimann and U. Mester, Inst. Physics. Conf. Ser. No. *26*, 219 (1975).

2.6 C. F. Warnke, in Temperature: Its Measurement and Control in Industry, edited by H. H. Plumb (Instrument Society of America, Pittsburgh, 1975), Vol. 4.

2.7 James F. Schooley, Thermometry, (Chemical Rubber, Cleveland, OH, 1986).

2.8 F. G. Allen, Silicon Molecular Beam Epitaxy, edited by J. C. Beam (Electrochemical Society, Pennington, N. J., 1985), pp.3-15.

2.9 V. M. Donnelly and J. A. McCaulley. J. Vac. Sci. Technol. *A8*, 84 (1990).

2.10 H. Sankur and W. Gunning. Appl. Phys. Lett. *56*, 2651 (1990).

2.11 E. A. Morozova, G. A. Shafeev and M. Wautelet. Meas. Sci. Technol. *3*, 302 (1992).

2.12 Katherine L. Saenger and Julie Gupta. Applied Optics *30*, 1221 (1991).

2.13 James C. Sturm. Casper M. Reaves. IEEE Trans. on Electron Devices *39*, 81 (1992).

2.14 S. C. H. Hung, H. K. Dong, and C. W. Tu, Mat. Res. Soc. Symp. Proc. *340*, 35 (1994).

2.15 Glen E. Myers, Analytical Methods in Conduction Heat Transfer, (McGraw-Hill, New York, 1971), pp.1-33.

3. Laser-Assisted MOMBE of GaAs Using As_4

3.1 Introduction

As a method that combines some advantages of MBE and MOCVD, MOMBE has gained increasing interest not only for the fundamental studies of growth kinetics[3.1-3] but also for device applications[3.4] due to its potential of high throughput and selective-area growth and doping[3.5-7]. Because MOMBE takes place in an ultra-high vacuum chamber, RHEED can be used to clarify the growth mechanisms. Both group-III and group-V species were found to play important roles in the surface chemical reactions during MOMBE growth[3.1-3]. In order to perform the laser-assisted MOMBE growth, we need to study the MOMBE growth behavior in more detail to obtain enough data for comparison. In this chapter we are going to discuss MOMBE and laser-assisted MOMBE of GaAs on (001) GaAs substrate.

3.2 MOMBE of GaAs

Chow and Fernandez[3.8] examined the transition between Ga- and As-controlled incorporation rates on GaAs by RHEED in a conventional solid-source MBE system, and demonstrated the effects of substrate temperature on the transition point between Ga and As controlled incorporation. The As incorporation rate is independent of substrate temperature at low substrate temperatures, and has an Arrhenius dependence with a positive activation energy at high temperatures. Most of the previous work on growth kinetics of MOMBE of GaAs focused on the normal growth regime where an excess flux of As species is always supplied[3.9, 3.10]. In this work we used RHEED intensity oscillations to study the effects of varying the triethylgallium flow rate and arsenic flux on the growth rate over a wide range of substrate temperatures. Both the excess-arsenic and excess-gallium conditions in MOMBE growth were investigated[3.11].

Solid arsenic (As_4) was used as the group V source material for MOMBE growth. Semi-insulating (100) GaAs substrates were chemically etched and thermally cleaned at about 600°C. The substrate temperature was calibrated by using an infrared-laser interferometric technique discussed above, which gave an accuracy of about ±4°C. The RHEED intensity oscillation was used to measure the growth rate.

In the growth of III-V compound semiconductors, the V/III flux ratio is a key parameter for the control of materials quality and composition determination. Although the beam flux ion gauge gives us a value of V/III flux ratio, this value is not the actual V/III incorporation ratio and it varies in different systems. By studying both the group-III and group-V induced RHEED oscillations[4.12], we establish a quantitative method of obtaining the actual V/III incorporation ratio. Fig. 3.1 illustrates a typical RHEED oscillation and shutter/valve operation sequence during the growth of GaAs at 540°C. It starts with an arsenic-stabilized surface, and the Ga-induced oscillation is observed after the TEGa is introduced. The RHEED intensity decreases after the arsenic shutter is closed due to the Ga accumulation on the substrate. Then the TEGa valve is closed, and the arsenic shutter is opened at the same time. The oscillation resumes with incoming arsenic species reacting with the Ga accumulation on the surface. This represents arsenic-controlled growth because there is an excess amount of Ga adatoms on the surface and the available amount of arsenic limits the growth rate.

Fig. 3.2 shows the GaAs growth rate versus substrate temperature at different TEGa flow rate (0.1-0.35 sccm) for an arsenic flux of 3.0×10^{-6} Torr. The data are similar to those from other studies[3.13, 3.14] except that we did not study the growth for substrate temperatures lower than 400°C. The growth rate stays almost constant in the temperature range from 420 to 580°C because the pyrolytic decomposition of TEGa is complete above 420°C, but it decreases when the substrate temperature is higher than 580°C which is due

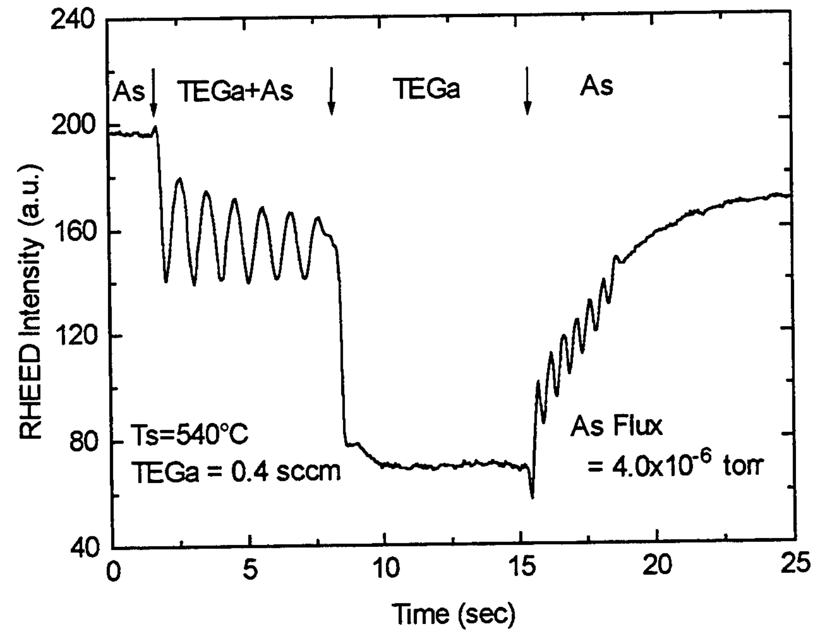

Fig. 3.1 RHEED intensity oscillations.

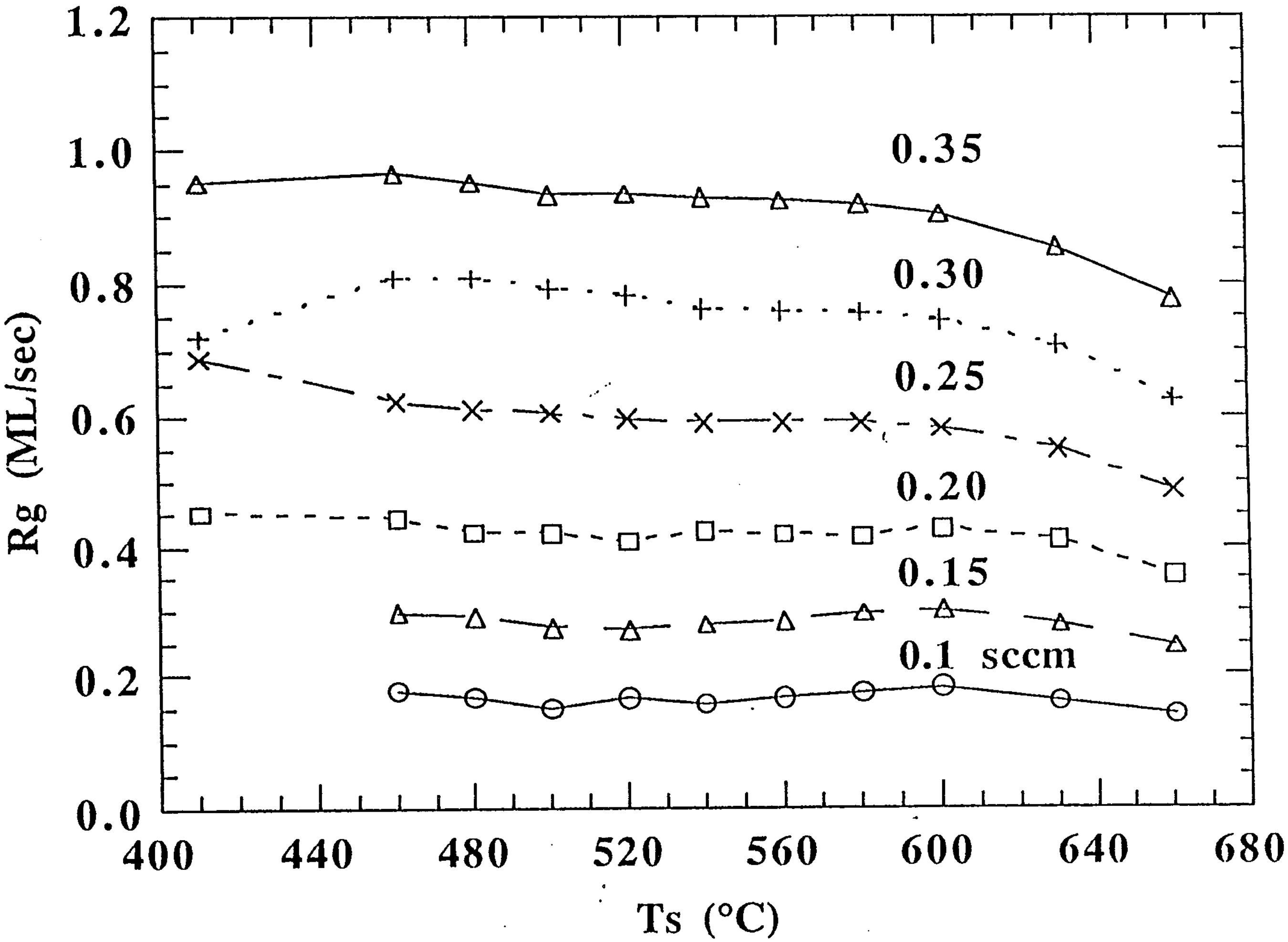

Fig. 3.2 GaAs growth rate versus substrate temperature at different TEGa flow rates for an arsenic flux of 3.0×10^{-6} Torr.

to the TEGa desorption at high temperature. When the TEGa flow rate is higher than 0.35 sccm, the relation between the growth rate and the substrate temperature changes greatly.

Fig. 3.3 shows the GaAs growth rate versus TEGa flow rate at different substrate temperatures under an arsenic flux of 3.0×10^{-6} Torr. At low TEGa supply rates, the GaAs growth rate follows a linear relation with respect to the flow rate for all different substrate temperatures, and an arsenic stabilized (2x4) surface reconstruction is observed. This linear relation extends up to about 0.35 sccm TEGa flow rate, where the growth rate reaches its maximum value, approximately 1.0 ML/sec. For the substrate temperature higher than 540°C, the figure clearly shows a transition region where the growth rate decreases as the TEGa flow rate increases past 0.35 sccm. In the transition region, the RHEED pattern changes from (2x4) to the Ga-stabilized (4x2) reconstruction. As the TEGa flow rate further increases, the growth rate then reaches a stabilization region where it does not change with the TEGa flow rate. In the stabilization region, the RHEED pattern becomes (4x2) immediately as growth starts. The higher the substrate temperature is, the lower the growth rate will be in the stabilization region. For the low substrate temperature conditions (480°C and 500°C), the growth rate starts to decrease gradually as the TEGa flow rate increases beyond 0.4 sccm, up to the highest TEGa flow rate used in our experiment (0.6 sccm). At higher TEGa flow rate, the RHEED intensity oscillation is difficult to observe. As the TEGa flow rate further increases, the growth rate could also become stabilized. A similar growth behavior is observed when the arsenic flux is changed to 2.5×10^{-6} Torr and 4.0×10^{-6} Torr. The growth rate at the transition point in these two cases is about 0.9 ML/sec and 1.5 ML/sec, respectively. The higher the arsenic flux is, the higher the TEGa flow rate at the transition point will be.

From Fig. 3.3, we can also see that the transition point at substrate temperatures of 580°C and 600°C occurs at a higher TEGa flow rate with a higher growth rate than at the other three lower substrate temperatures. Since the desorption of TEGa takes place when

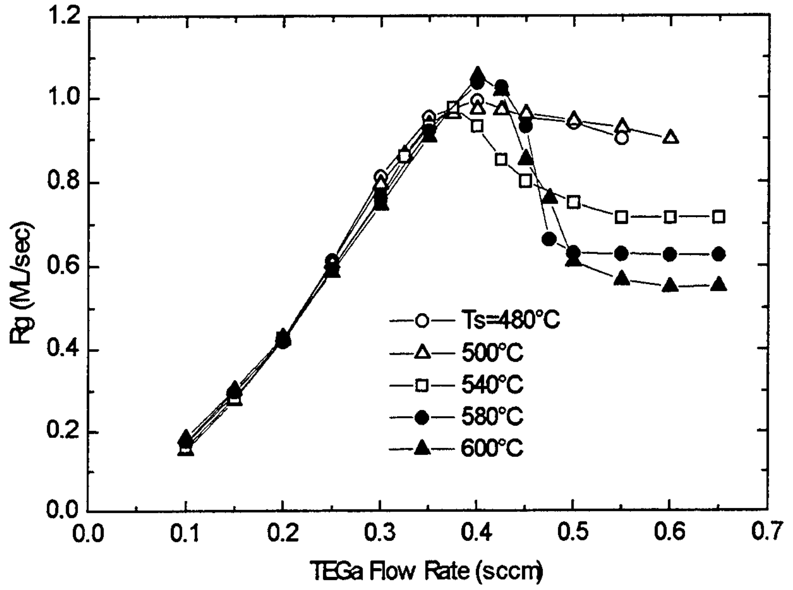

Fig. 3.3 GaAs growth rate versus TEGa flow rate at different substrate temperature under an arsenic flux of $3.0\text{x}10^{-6}$ Torr.

the substrate temperature is higher than 550°C, a higher TEGa flow is needed in order to maintain a unity V/III incorporation ratio and hence the transition point occurs at a higher TEGa flow rate. The shift of transition point to a higher TEGa flow rate extends the linear region and a higher TEGa flow gives a higher growth rate.

Compared to solid-source MBE[3.8], the transition region between V/III>1 and V/III<1 is quite gradual. This could be caused by the complicated surface reaction in MOMBE. At high temperatures (above 540°C), the MOMBE growth behavior approaches solid-source MBE. At low temperatures (480°C and 500°C), however, the MOMBE GaAs growth rate changes very little as the TEGa flow rate increases. This may come from the incomplete decomposition of excess TEGa molecules on the substrate surface.

Typical RHEED intensity oscillation data for the three different regions (linear, transition and stabilization) are shown in Fig. 3.4 (a), (b) and (c), respectively. At time t_1, TEGa is supplied, while at time t_2, TEGa supply is stopped. Arsenic is always supplied during the growth process. In the linear region, normal Ga-induced RHEED oscillations is observed, showing arsenic-excess growth condition. In the transition region, the growth shows Ga-controlled incorporation at first and then changes to As-controlled incorporation. However, the growth rate for both Ga- and As-controlled incorporation is the same. The number of RHEED oscillations in the transition region is far fewer than the other two regions. The reason is still not clear yet. The decrease of the growth rate with the increase of substrate temperature in the stabilization region is proposed to be due to arsenic desorption. The arsenic surface concentration becomes lower as the substrate temperature increases, and hence results in lower growth rate. In Figures 3.4(b) and 3.4(c), after the TEGa supply is stopped, there is no continued RHEED intensity oscillation, implying no residual gallium on the surface. This is in contrast to solid source MBE where RHEED oscillations are observed even after the Ga shutter is closed, due to the excess gallium atoms on the surface[3.8]. From Fig. 3.1, we see that As-induced oscillations occur after TEGa supply is stopped and arsenic supply is resumed. Therefore,

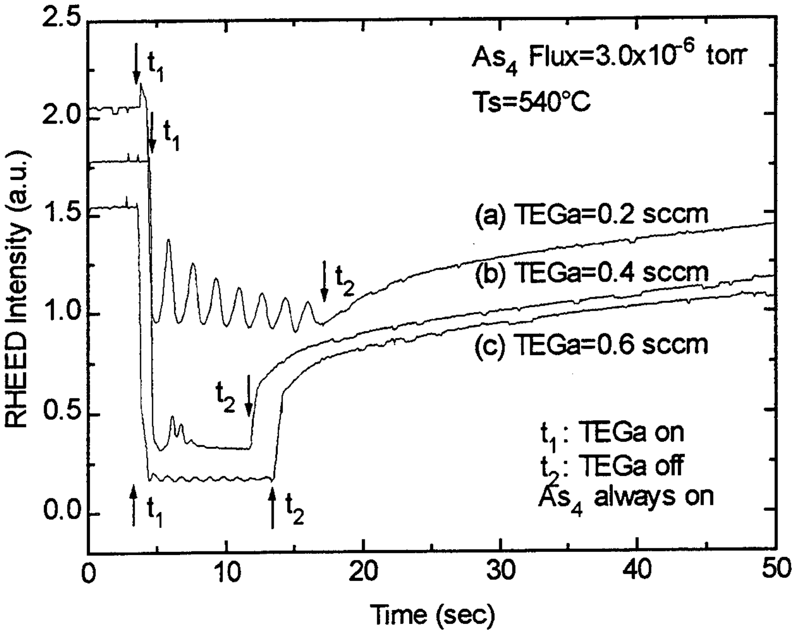

Fig.3.4 RHEED intensity oscillation data for (a) linear region, (b) transition region, and (c) stabilization region.

in MOMBE gallium accumulation occurs when only TEGa is supplied to the GaAs surface. This could be due to an enhanced desorption of excess TEGa on the surface when there are both TEGa and As_4 supplies.

Fig. 3.5 shows the arsenic incorporation rate as a function of substrate temperature. The arsenic incorporation rate is constant at low substrate temperatures and starts to decrease, due to arsenic desorption, when the substrate temperature is above 520°C. The activation energy for arsenic incorporation is calculated to be about 0.35 eV, which is smaller than that obtained in solid-source MBE[3.8]. This could be due to the surface chemical reaction between TEGa and As_4. The arsenic incorporation rate is about 0.9 ML/sec, 1ML/sec, and 1.5 ML/sec, when the arsenic flux is 2.5, 3.0 and 4.0×10^{-6} Torr, respectively. Comparing to the growth rates at the transition points (Fig. 3.3) mentioned previously, we conclude that the V/III incorporation ratio is about unity at the transition point. When the V/III ratio is greater than unity, the growth is Ga-controlled. When the V/III ratio is less than unity, the growth becomes very complicated, including arsenic-controlled growth and the transition between Ga-controlled and As-controlled growth.

The data denoted by solid symbols are obtained from the group-V induced RHEED intensity oscillation study as shown in Fig. 3.1, while the data denoted by open symbols are the arsenic-controlled growth rates in the stabilization region as shown in Fig. 3.3. The arsenic flux is the same for the symbols with the same shape (square, circle, or triangle). In each case, the solid line shows a higher arsenic incorporation rate than the dashed line. In taking data, TEGa is introduced in order to obtain Ga accumulation on the substrate surface, and no TEGa is supplied after the arsenic shutter is opened again. The accumulated gallium could physisorb on the surface and form clusters. When the arsenic atoms arrive, they could directly incorporate into the lattice among the clusters, and the physisorbed gallium atoms will migrate and chemisorb with arsenic atoms. The arsenic incorporation rate will be the arrival rate of arsenic atoms minus the desorption rate. For the data taken in the stabilization region, however, TEGa and arsenic are supplied at the

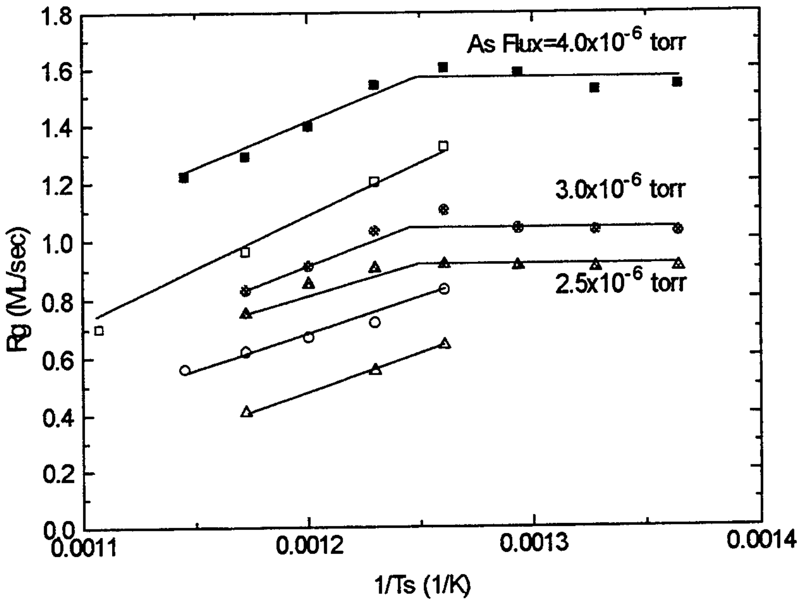

Fig. 3.5 Arsenic-induced growth rate versus 1/T_S at a TEGa flow rate of 0.35 sccm for different arsenic fluxes.

same time. The adsorbed TEGa molecules on the substrate surface could retard the arsenic incorporation, and hence the incorporation rate will be smaller than the above one.

3.3 Laser-Assisted MOMBE of GaAs

Recently, laser-assisted crystal growth of III-V compound semiconductors has attracted much attention because of its great potential for selective-area growth and doping, and possible application to optoelectronic devices. Both excimer laser and Ar^+ laser irradiation have been employed in MOMBE and MOCVD[3.5-7, 3.15-22]. So far, three models have been proposed for the mechanism of photo-assisted epitaxy: catalytic (or electronic), pyrolytic and photolytic decomposition of metalorganic molecules. Donnelly *et al.*[3.5] explained their results with excimer laser irradiation using the pyrolytic decomposition model. In Ar^+ laser-assisted CBE where AsH_3 was used, the heating effect is minor and Aoyagi *et al.*[3.15] proposed a catalytic process since the growth rate enhancement depends on substrate conductivity. Similarly for Ar^+ laser-assisted CBE of GaAs and GaP, Sugiura *et al.*[3.18] concluded that the mechanism involved is most likely a photolytic decomposition of the metalorganic molecules since enhanced growth on GaP, which is transparent to the Ar^+ laser beam, exhibits the same behavior as on GaAs. With Ar^+ laser irradiation, the decomposition rate of triethylgallium (TEGa) on the As plane is enhanced very much in comparison to that on the Ga plane[3.16], and the epitaxial GaAs layer shows lower carbon incorporation and better optical property[3.20]. So far in the literature, there are only reports on laser-induced TEGa decomposition. The role of arsenic species during laser-assisted MOMBE growth has not been mentioned. In this work, the enhancement of TEGa decomposition and arsenic desorption with Ar^+ laser irradiation is investigated by observing the RHEED specular-beam intensity oscillations. The laser power density used in this experiment was 400 W/cm^2, which corresponds to a substrate temperature rise of about 20°C as discussed in section 2.6.3.

We have used RHEED oscillations to study the behavior of Ar^+ laser-assisted GaAs growth in the substrate temperature range of 330-450°C with the laser turned on and off. Fig. 3.6 shows RHEED oscillations with and without Ar^+ laser irradiation during TEGa and As_4 exposure at a substrate temperature of 365°C. After a 2000 Å GaAs buffer layer was grown with solid Ga and As_4 at 580°C, the substrate was cooled down to 365°C with the Ga shutter closed and the arsenic flux lowered (by closing one of the two arsenic cells in the system). When the temperature was stabilized, TEGa was introduced into the growth chamber. The upper curve in Fig. 3.6, obtained under Ar^+ laser irradiation, is totally different from the lower curve with no laser irradiation. The results clearly show that there is GaAs growth with laser irradiation while there is no growth without laser irradiation. This RHEED result is verified by Dektak stylus profiler and Nomarski microscope measurements.

Fig. 3.7 shows the RHEED intensity oscillation pattern with and without Ar^+ laser irradiation with TEGa and As_4 supply at a substrate temperature of 410°C. After the substrate temperature was stabilized at 410°C, TEGa was introduced into the growth chamber and the Ar^+ laser was turned on at the same time. After seven layers were grown, the Ar^+ laser was turned off. The oscillations with laser irradiation have much higher amplitudes and slower damping than those without laser irradiation, which indicates the enhancement of the surface migration of TEGa molecules and/or Ga adatoms on the surface with laser irradiation. The growth rate under laser irradiation is a little larger than that without laser irradiation, showing the enhancement of TEGa decomposition under laser irradiation.

The growth rate as a function of substrate temperature is shown in Fig. 3.8. At temperatures in the range 340-420°C, the enhancement of TEGa decomposition with laser irradiation compared to that without laser irradiation is observed. When the substrate temperature is lower than 370°C, there is only laser-assisted growth. There is no laser-assisted growth for substrate temperature lower than 340°C, and there is no change of

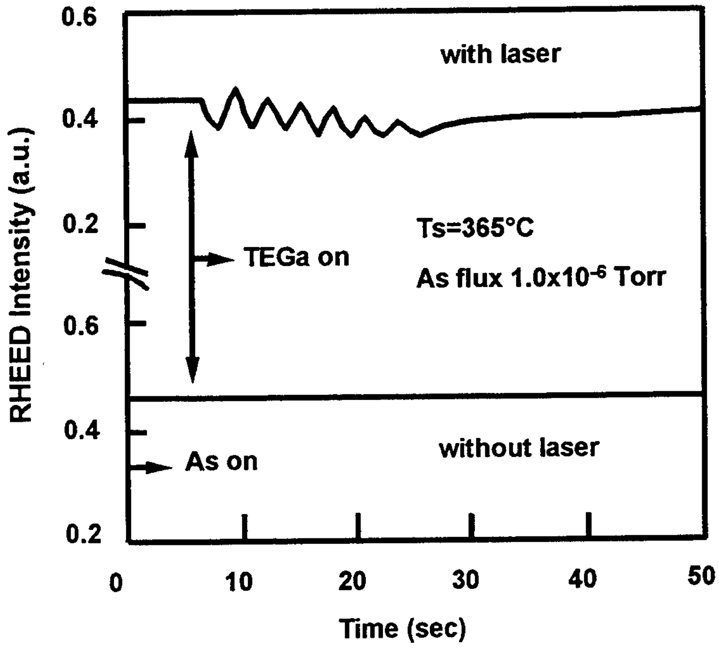

Fig. 3.6 RHEED oscillations with and without laser irradiation at a substrate temperature of 365°C. Enhanced growth of GaAs is observed with laser irradiation, while no growth is observed without laser irradiation.

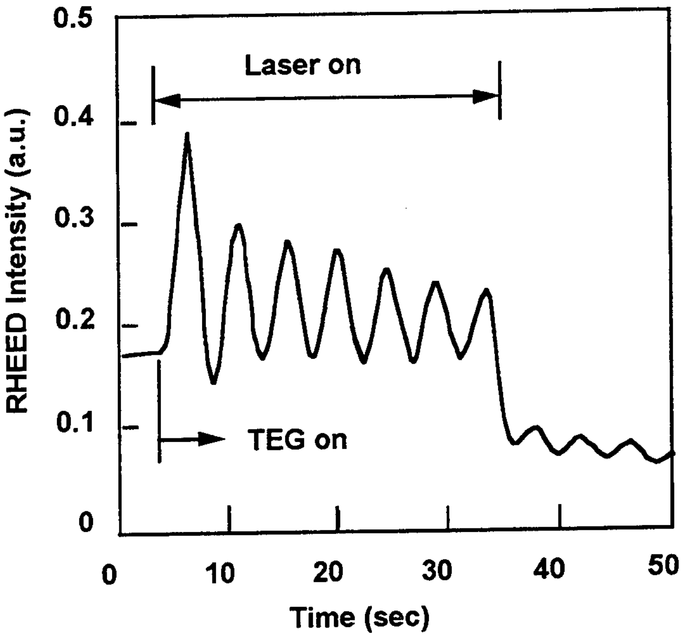

Fig. 3.7 RHEED oscillations with and without laser irradiation with TEGa and arsenic supply at a substrate temperature of 410°C.

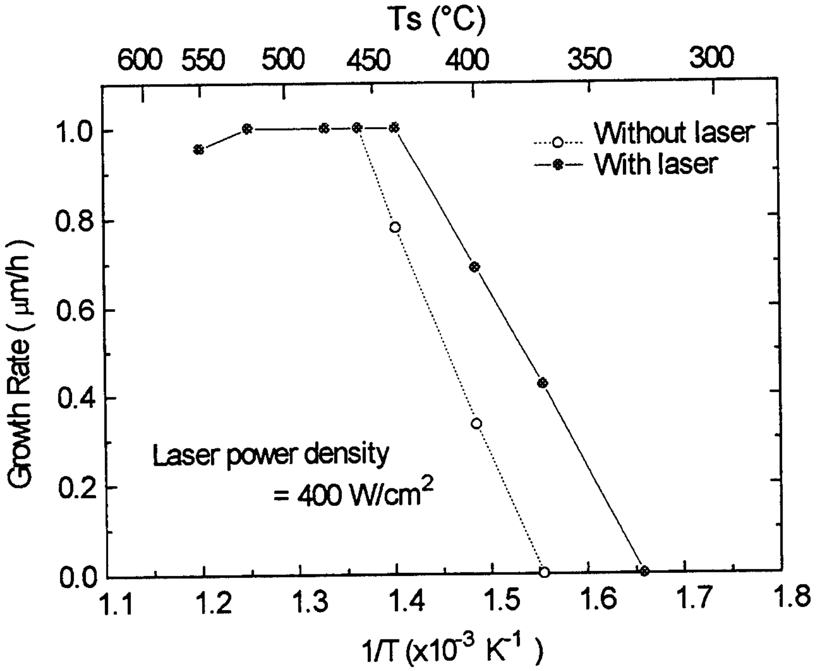

Fig. 3.8 The growth rate as a function of substrate temperature with and without laser irradiation.

growth rate for substrate temperature higher than 420°C with or without laser irradiation. Since the substrate temperature rise due to laser irradiation is about 20°C, the pyrolytic decomposition of TEGa alone is not likely. However, as we see in Fig. 3.9, the TEGa absorption cross section is almost negligible when the laser wavelength is above 320 nm. Therefore, photolytic decomposition of TEGa is unlikely. Catalytic effect from laser irradiation, which we do not have direct proof yet, is another possibility for the further enhanced GaAs growth rate apart from the pyrolytic effect. We propose that both pyrolytic and catalytic decomposition of TEGa play roles in Ar^+ laser-assisted MOMBE growth of GaAs. The enhancement of growth rate with laser irradiation in comparison to that without laser irradiation becomes smaller with increasing substrate temperature, because the thermal decomposition of TEGa becomes more important.

Fig. 3.10 shows the RHEED data of arsenic desorption behavior under 5W Ar^+ laser irradiation at a substrate temperature of 500°C. Only As_4 was used, and the arsenic cell shutter was always open during the study. The laser effect is clearly seen from the decrease of the RHEED intensity while the laser is turned on and from the recovery of the RHEED intensity while the laser is turned off. Similar behavior of RHEED data is obtained in studying the desorption of arsenic from GaAs without laser irradiation. In this case, we close the arsenic cell shutter (instead of turning on the laser) and then open the arsenic cell shutter (instead of turning off the laser). When we block the As_4 beam (although there may still be some flux leaking out), the surface arsenic concentration is lowered and the surface becomes rougher because of the desorption of arsenic from the heated surface so that the RHEED intensity decreases. When we restore the As_4 beam, the RHEED intensity recovers. The same kind of experiment is also done at lower substrate temperatures, and similar behavior, but with a smaller change of RHEED intensity, is observed. Therefore we conclude that Ar^+ laser irradiation enhances the desorption of arsenic. Liang and Tu[3.2] have already found that group-III and group-V species are equally important in the surface chemical reactions in MOMBE growth. The

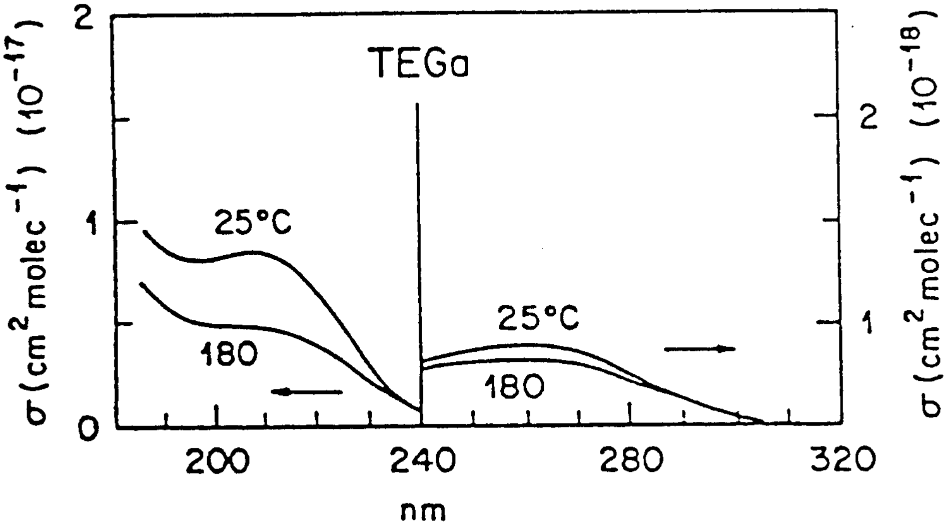

Fig. 3.9 TEGa absorption cross section as a function of laser wavelength.

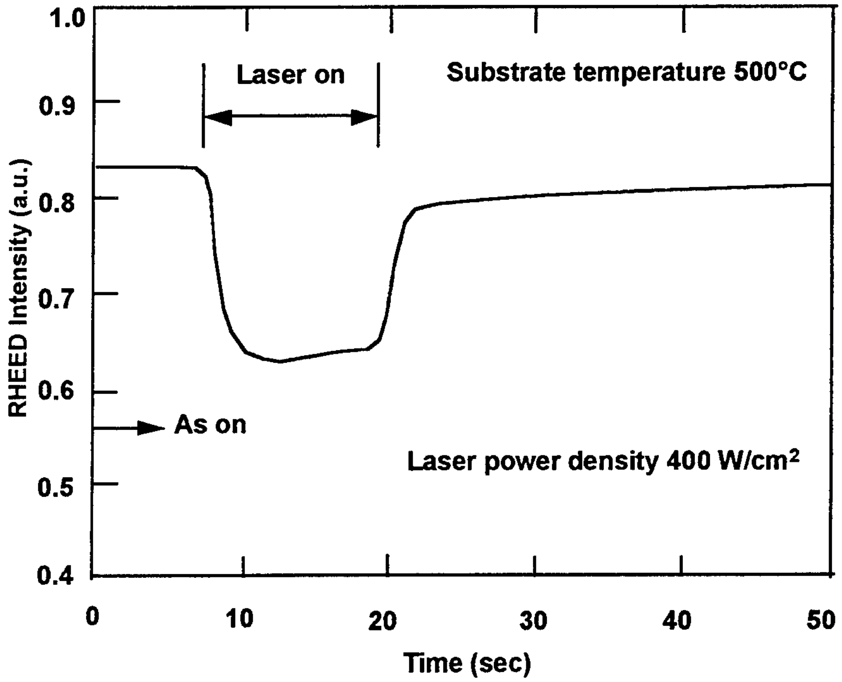

Fig. 3.10 RHEED data showing arsenic desorption behavior under laser irradiation and arsenic exposure.

growth rate of GaAs changes with arsenic surface concentration, and growth can become arsenic-controlled. In this case, increasing the arsenic flux results in increasing the growth rate. On the other hand, too high an arsenic concentration results in site blocking or enhanced desorption of TEGa molecules, and hence, lowers the growth rate. With Ar^+ laser irradiation, the arsenic surface concentration is decreased, resulting in a growth-rate change.

In laser-assisted MOMBE growth of GaAs, both decomposition of TEGa and desorption of As_4 play a role in the surface chemical reaction. As shown in Fig. 3.11, the growth study was done at a substrate temperature of 390°C with different arsenic fluxes, but the same TEGa flow, under different laser power. For arsenic flux values of 2.0×10^{-6} and 2.5×10^{-6} Torr, the growth rate increases monotonically at low laser power and becomes saturated at high laser power. Both the decomposition rate of TEGa and the desorption rate of arsenic increase with increasing laser power. The decomposition of TEGa raises the growth rate, while the desorption of arsenic lowers the growth rate. As seen in the figure, the growth rate increases with increasing arsenic flux in the case with no laser irradiation which indicates that we are in the arsenic-controlled growth regime. At low laser power density, the growth rate is mainly determined by the decomposition of TEGa, so the growth rate increases monotonically. At high laser power density, arsenic desorption becomes severe and balances the decomposition of TEGa, so the growth rate becomes almost constant. Except for the case of 1.0×10^{-6} Torr As_4 and 600 W/cm^2 laser power, which is not understood yet, this explanation of saturated growth rate seems correct.

3.4 References

3.1 A. Robertson, Jr., T. H. Chiu, W. T. Tsang, and J. E. Cunningham, J. Appl. Phys. *64*, 877 (1988).

3.2 B. W. Liang and C. W. Tu, Appl. Phys. Lett. *57*, 689 (1990).

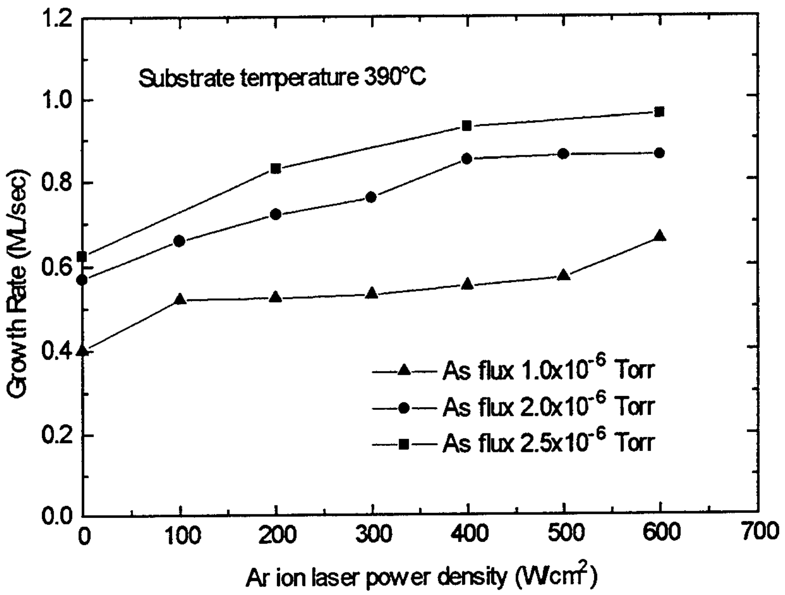

Fig. 3.11 Growth rate versus Ar ion laser power density at constant TEGa flow but under different arsenic flux at a substrate temperature of 390°C.

3.3 H. Asahi, T. Kaneko, Y. Okuno, and S. Gonda, Jpn. J. Appl. Phys. *32*, 2786 (1993).

3.4 Y. M. Houng, Y. C. Pao, and P. McLeod, Mat. Res. Soc. Proc. *145*, 63 (1989).

3.5 V. M. Donnelly, C. W. Tu, J. C. Beggy, V. R. McCrary, M. G. Lamont, T. D. Harris, F. A. Baiocchi, and R. C. Farrow, Appl. Phys. Lett. *52*, 1065 (1988).

3.6 H. Sugiura, R. Iga, and T. Yamada, J. Cryst. Growth *120*, 389 (1992).

3.7 H. K. Dong, B. W. Liang, M. C. Ho, S. Hung and C. W. Tu, J. Crystal Growth *124*, 181 (1992).

3.8 R. Chow and R. Fernandez, Mat. Res. Soc. Proc. *145*, 13 (1989).

3.9 T. H. Chiu, W. T. Tsang, J. E. Cunningham, J. Appl. Phys. *62*, 2302 (1987).

3.10 N. Kobayashi, J. L. Benchimol, F. Alexandre and Y. Gao, Appl. Phys. Lett. *51*, 1907 (1987).

3.11 H. K. Dong, S. C. H. Hung, C. W. Tu, Mat. Res. Soc. Proc. *340*, 193 (1994).

3.12 T. P. Chin, B. W. Liang, H. Q. Hou, M. C. Ho, C. E. Chang, and C. W. Tu, Appl. Phys. Lett. *58*, 254 (1991).

3.13 T. H. Chiu, J. E. Cunningham, and A. Robertson, J. Cryst. Growth *95*, 136 (1989).

3.14 D. E. Lacklison, C. T. Foxon, J. Zhang, B. A. Joyce, and E. M. Gibson, J. Cryst. Growth *120*, 50 (1992).

3.15 Y. Aoyagi, M. Kanazawa, A. Doi, S. Iwai, and S. Namba, J. Appl. Phys. *60*, 3131 (1986).

3.16 K. Nagata, Y. Iimura, Y. Aoyagi, S. Namba, and S. Den, J. Crystal Growth *105*, 52 (1990).

3.17 Y. Aoyagi, T. Meguro, S. Iwai, and A. Doi, Mater. Sci. & Engi. *B10*, 121 (1991).

3.18 H. Sugiura, T. Yamada, and R. Iga, Jpn. J. Appl. Phys. *29*, L1 (1990).

3.19 H. Sugiura, R. Iga, T. Yamada, and M. Yamaguchi, Appl. Phys. Lett. *54*, 335 (1989).

3.20 R. Iga, H. Sugiura, T. Yamada, and K. Wada, Appl. Phys. Lett. *55*, 451 (1989).

3.21 R. Iga, H. Sugiura, and T. Yamada, Jpn. J. Appl. Phys. *29*, 475 (1990).

3.22 R. Iga, H. Sugiura, and T. Yamada, Jpn. J. Appl. Phys. *30*, L4 (1991).

4 Laser-Modified MOMBE of InGaAs/GaAs MQWs

4.1 Introduction

In this chapter we are going to discuss MOMBE and laser-assisted MOMBE of InGaAs on (001) GaAs substrate. Iga *et al.*[4.1] studied Ar ion laser-assisted CBE of InGaAs on InP, and found that laser irradiation decreased the InGaAs growth rate and the Ga fraction of the InGaAs film at substrate temperatures above 500°C. They suggested that the reduction in the As coverage of the surface caused by laser-induced heating could enhance the reevaporation of triethylgallium (TEGa) molecules from the surface, and hence reduced the growth rate. The same kind of suppression was also observed in Ar ion laser-assisted CBE of $In_{1-x}Ga_xAs_{1-y}P_y$.[4.2] The photoluminescence (PL) wavelength of an InGaAsP/InP multiple quantum well (MQW) structure shifts to longer wavelength by 1300 Å with laser irradiation during the growth of the InGaAsP wells. An InGaAsP/InP double-wavelength laser has been fabricated successfully by laser-assisted CBE[4.3].

So far, no one has performed laser-assisted or modified MOMBE of InGaAs on a GaAs substrate. In recent years, $In_xGa_{1-x}As$/GaAs strained-layer heterostructures have been used in the fabrication of high-performance devices, such as near-infrared lasers[4.4] and high-speed two-dimensional electron gas field-effect transistors[4.5]. In this work, we study the growth behavior of InGaAs on GaAs by RHEED and investigate the effects of Ar ion laser irradiation on the growth of InGaAs/GaAs strained MQW structures.

4.2 MOMBE of InGaAs

By studying both the group III- and group V-induced RHEED oscillations, we have already established a quantitative method of obtaining the actual V/III incorporation ratio for GaAs and InAs during MOMBE growth.[4.6] However, it is more complicated for InGaAs because the surface chemical reactions involve all species (group III metalorganics and As_4). Hence the group III fluxes are not simply additive.

Fig. 4.1 shows the RHEED intensity oscillation data for InGaAs and GaAs grown on a (100) GaAs substrate. By comparing the growth rate of InGaAs with that of GaAs at each period of intensity oscillation, we find that the InGaAs growth rate gradually decreases below that of GaAs as time proceeds. This is similar to what has been observed in CBE of InGaAs[4.7], and is different from the case of solid-source MBE-grown InGaAs. Figs. 4.2a and 4.2b show the transient growth behavior for different TMIn flow rates and substrate temperatures, respectively. Since the TEGa and TMIn flow rates become stabilized within 4-5 seconds after the run/vent switch, only 1-2 oscillations were affected by the flow transient. Here, we plot the InGaAs growth rate normalized by the GaAs growth rate of the corresponding period versus the number of oscillations. It is shown that the InGaAs growth rate decreases with time to a stabilized value, and is lower for higher substrate temperature or higher TMIn flow rate. Surface segregation of indium during growth and a lower sticking coefficient of TEGa molecules on an indium-covered surface are believed to be the reason that the InGaAs growth rate becomes lower than that of GaAs with the same TEGa flow rate and arsenic supply[4.7]. The activation energy of TEGa desorption from the indium-covered surface (E_{In}) is lower than that from the gallium- or arsenic-covered surface (E_{Ga} or E_{As}), so the presence of indium on the surface lowers the Ga incorporation[4.8]. A higher TMIn flow rate causes more indium surface coverage, and hence lowers the growth rate. As the substrate temperature increases, more TEGa and TMIn will desorb from the surface. Therefore, the stabilized InGaAs growth rate decreases when the substrate temperature is increased.

Two 20-period $In_xGa_{1-x}As$/GaAs MQW structures were grown at 500°C and 550°C, respectively, under the same TEGa and TMIn flow rates, arsenic beam equivalent pressure, and time duration for well and barrier growth. They were characterized by X-

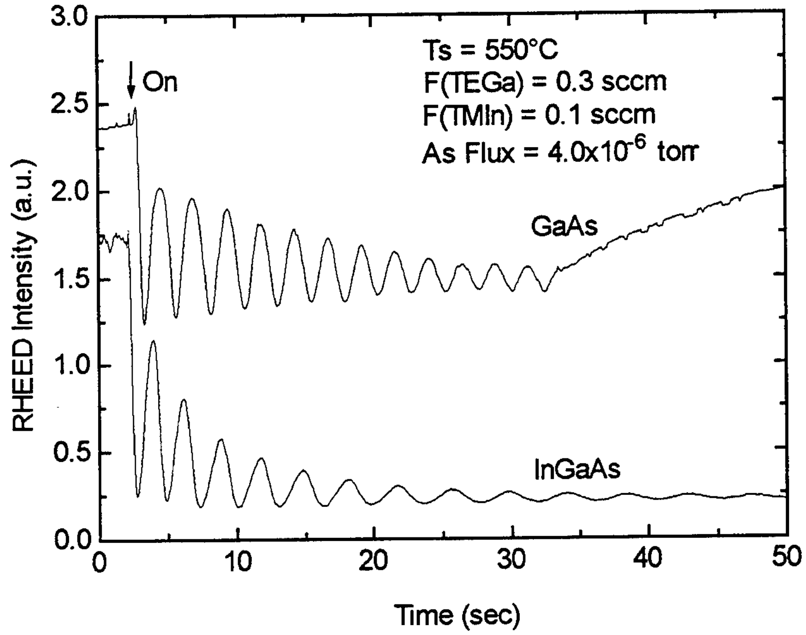

Fig. 4.1 RHEED intensity oscillation data for InGaAs and GaAs grown on (100) GaAs substrate.

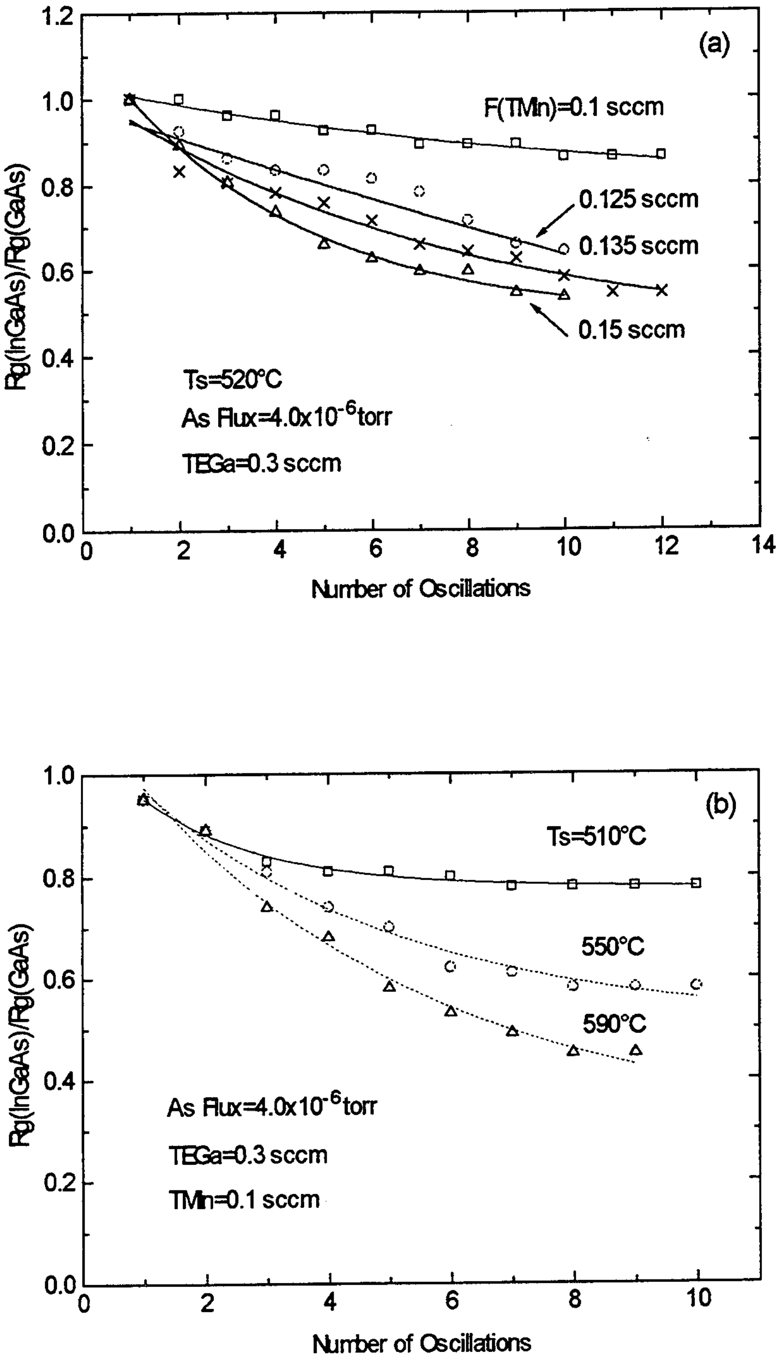

Fig. 4.2 InGaAs transient growth behavior
(a) with changing TMIn flow rate
(b) with changing substrate temperature.

ray rocking curve measurements, and the well composition and thickness were determined by simulations based on the dynamic theory[4.9]. Fig. 4.3 shows the X-ray rocking curve (a) and the simulation results (b and c) for the MQW structure grown at 500°C. Curve (b) assumes a uniform distribution of well thickness and composition throughout the MQW structure, and both peak intensities and peak positions fit quite well. The simulation suggests that the MQW consists of 20 periods of $In_{0.25}Ga_{0.75}As$(85Å)/GaAs(140Å). However, the peaks in curve (b) are much narrower than those in the actual rocking curve (a). Curve (c) assumes that the well widths vary by +/– one monolayer and the indium contents change between 24% and 26% randomly within the MQW structure. The simulation gives a much better fit than curve (b), and the peak widths are very close to the experimental data. Therefore, we propose that a nonuniform distribution of well thickness (± one monolayer) and indium concentration (25%±1%) occurred during the CBE growth of the InGaAs/GaAs MQW structure. Similarly, computer simulations for the sample grown at 550°C show that the MQW structure is a 20-period $In_{0.35}Ga_{0.65}As$(20Å)/GaAs(180Å), also with a similar extent of thickness and composition nonuniformity as the 500°C sample.

Based on the model proposed by Houghton *et al.*[4.10, 4.11], the number of stable periods (or the maximum stable MQW thickness) as a function of the strain in the quantum wells can be calculated for the $In_xGa_{1-x}As$/GaAs MQW structure. Fig. 4.4 shows the critical number of MQW periods vs. the indium concentration in the quantum well for three MQW structures with different well and/or barrier thicknesses. As we can see in the figure, the critical number of periods for the $In_{0.25}Ga_{0.75}As$(85Å)/GaAs(140Å) and the $In_{0.35}Ga_{0.65}As$(20Å)/GaAs(180Å) MQW is 7 and 24, respectively. Therefore, the 500°C sample with a well width of 85Å and 20 periods exceeds stable limit, but the 550°C sample with a well width of 20Å and 20 periods is still within the limit.

The InGaAs growth rate at 550°C is only about 1/4 of that at 500°C, and the indium concentration x at 550°C is 10% higher than that at 500°C. From the CBE study of

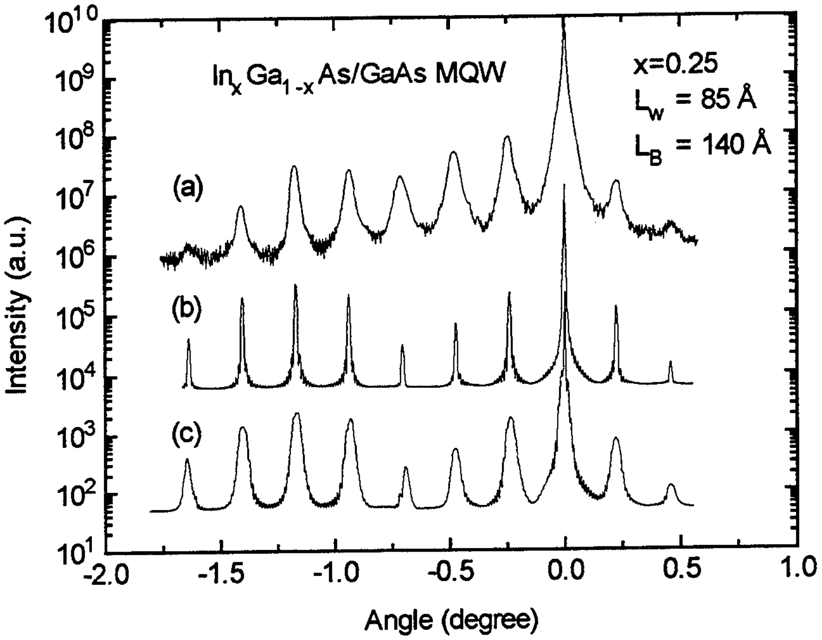

Fig. 4.3 X-ray rocking curves for the InGaAs/GaAs MQW structure grown at 500°C. (a) experimental result, (b) simulation result (uniform distribution of well thickness and indium concentration), and (c) simulation result (nonuniform distribution of well thickness and indium concentration).

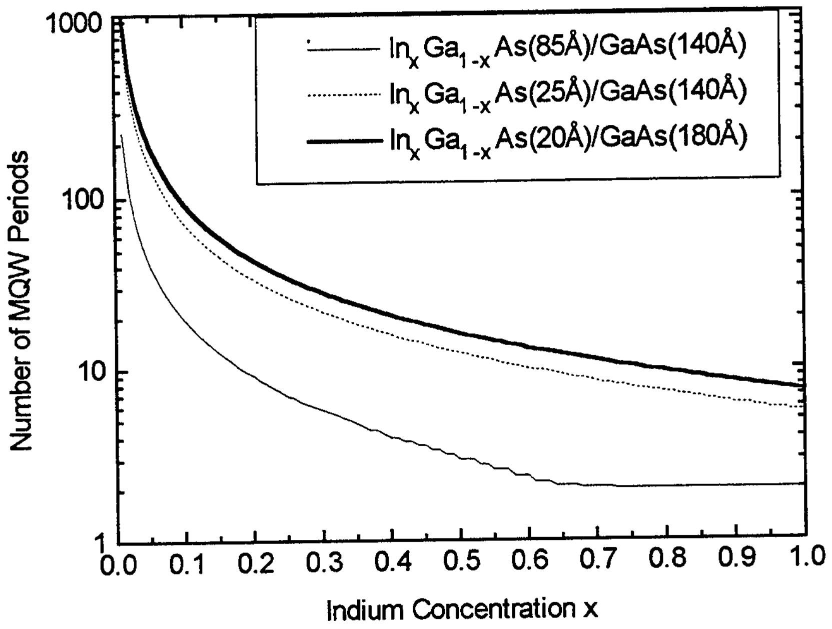

Fig. 4.4 The critical number of MQW periods as a function of indium concentration for $In_xGa_{1-x}As$(85Å)/GaAs(140Å), $In_xGa_{1-x}As$(25Å)/GaAs(140Å), and $In_xGa_{1-x}As$(20Å)/GaAs(180Å) MQW structures.

InGaAs on InP by Skevington and Amin[4.12], the indium concentration (as determined by data extrapolation) would increase by 8% as the substrate temperature increases from 500 to 550°C. Therefore, the 10% increase in the indium concentration (from 25% to 35%) is reasonable. The thicker GaAs barrier grown at 550°C is due to a higher GaAs growth rate at this temperature.

4.3 Laser-Modified MOMBE of InGaAs/GaAs MQWs

Based on the InGaAs and GaAs growth-rate data, determined from RHEED intensity oscillations, we grew several InGaAs/GaAs MQW structures. A 0.5 μm GaAs buffer layer was grown at a substrate temperature of 550°C, followed by 20-period $In_xGa_{1-x}As/GaAs$ MQWs grown under two different substrate temperatures, 500°C and 550°C. During growth, the flow rates of TEGa and TMIn were kept at 0.4 sccm and 0.12 sccm, respectively, and the arsenic beam equivalent pressure was 4.0×10^{-6} Torr. The samples were irradiated by the Ar ion laser only during the growth of the InGaAs wells. The growth was interrupted for about 10 seconds between wells and barriers. The laser power density was 400 W/cm^2, which gives a substrate temperature rise of about 20°C, according to the infrared laser interferometric measurement. The well composition and thickness of the non-irradiated area were determined accurately from X-ray rocking curve measurements and simulations using the dynamical theory[4.9]. Structural and optical properties were characterized by Nomarski microscopy, Dektak stylus profiler and low-temperature photoluminescence (PL) measurements.

Fig. 4.5a shows the morphology of a laser-irradiated sample grown at 500°C. The laser irradiated areas (***a*** and ***b***) can be clearly distinguished from the surrounding unirradiated area ***c***, which is rough (the number of MQW periods exceeds the critical limit). Area ***a*** shows a better morphology than area ***c***, but it has strain-induced cross-hatches. At the center of laser-irradiated spot, area ***b***, the surface is also rough, similar to

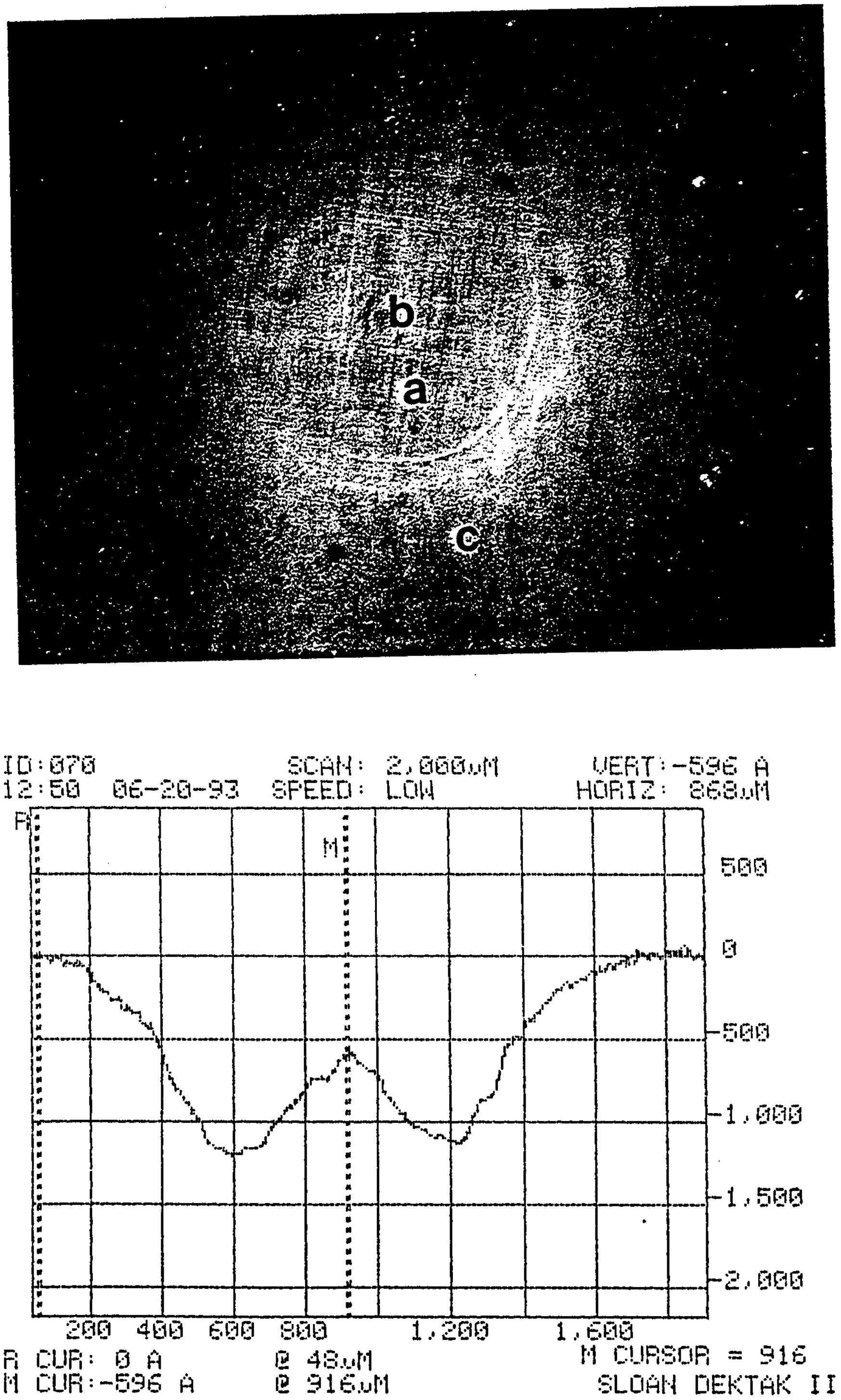

Fig. 4.5 Effects of Ar ion laser irradiation on InGaAs/GaAs multiple quantum wells. (a) Surface morphology by Nomarski microscopy (50x), (b) Dektak depth profile.

area ***c***. This is due to the fact that the homemade mirror that reflects the laser light onto the sample was damaged by the high power at the center of the laser beam, which is Gaussian in shape. As a result, the power density in the center of the beam impinging on the sample was lower, and the surface morphology is similar to the unirradiated area. Fig. 4.5b shows a DEKTAK depth profile of the sample shown in Fig. 4.5a. The diameter of the laser irradiated area is about 1.5 mm. We see the laser irradiation lowers the InGaAs growth rate in the two wells, corresponding to area ***a*** in Fig. 4.5a. The center bump corresponds to area ***b***, where the impinging laser power density is lower. The quantum well thickness is calculated to be 25 Å at the bottom of area ***a*** and 55 Å at the top of area ***b***.

Fig. 4.6 shows the low-temperature PL spectra (10 K) of the sample shown in Fig. 4.5. Spectra (a), (b) and (c) correspond to the areas ***a***, ***b***, and ***c*** in Fig. 4.5a, respectively. In the laser-irradiated area ***a*** the PL peak has a blue shift of about 2000 Å with respect to spectrum (c). The integrated peak intensity is almost doubled that in the unirradiated area ***c***, and the FWHM of the PL peak is improved from 42 meV in (c) to 17 meV in (a). The large FWHM values are caused by the strain relaxation and nonuniform distribution of well thickness and indium concentration in the MQW structure as discussed earlier. The PL peak position is influenced by changes of both well thickness and indium concentration. Iga *et al.*[4.1] have reported recently that TEGa molecules preferentially desorb under laser irradiation, so the indium concentration in area ***a*** should be higher. This should result in a red shift in PL, but we observe a blue shift. Therefore, the 2000 Å blue shift is mainly due to the much thinner quantum wells under laser irradiation. From the calculation based on the envelope-function model[4.13] (strain included), we conclude that a 20-period $In_{0.28}Ga_{0.72}As$(25Å)/GaAs(140Å) MQW structure was grown in area ***a*** under laser irradiation. We see that the indium concentration increases only 3% as compared to that in the nonirradiated area. A period number of 20 is still within the critical limit for the $In_{0.28}Ga_{0.72}As$(25Å)/GaAs(140Å) MQW, as shown in Fig. 4.4.

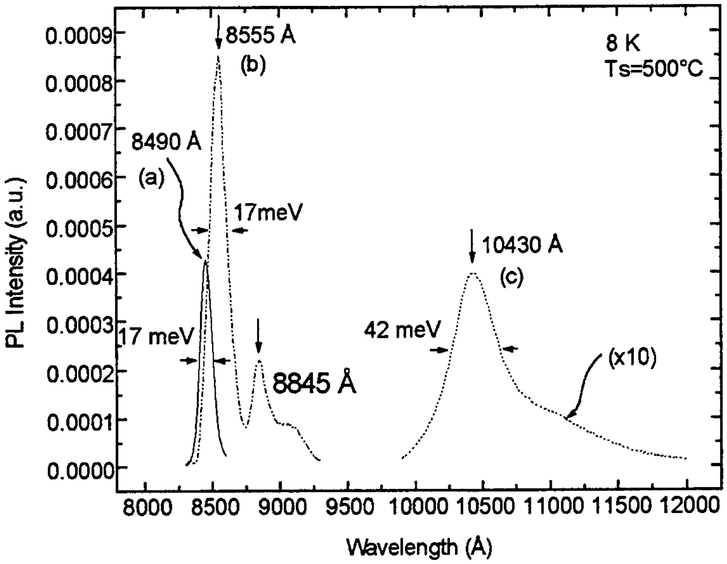

Fig. 4.6 Low temperature photoluminescence spectra of InGaAs/GaAs MQW structure grown at a substrate temperature of 500°C.

Therefore, the FWHM is narrower in area ***a***. Spectrum (b) in Fig. 4.6 shows three peaks because the PL pumping laser spot, about 200 μm in diameter, covers an area with different InGaAs well thicknesses. The integrated PL peak intensity in spectrum (a) is only about one-third as much as that at a wavelength of 8555 Å in spectrum (b). This may be due to a nonoptimal growth condition in area ***a***, where the substrate temperature increased by 20°C (Ar ion laser irradiation). From calculation, we find that the peak at 8555 Å in spectrum (b) can be obtained by adding one monolayer InGaAs to the well width used in area ***a***. By adding another four or eight monolayer InGaAs (which makes the well thickness to be 39 Å or 51 Å), the other two peaks in spectrum (b) can be deduced. The well thickness of 51 Å is very close to that at the top of area ***b*** (55 Å). This confirms that the multiple PL peaks come from the different InGaAs well widths.

For the 20-period $In_{0.35}Ga_{0.65}As/GaAs$ MQW structure grown at a substrate temperature of 550°C, both the morphology and growth rate were not influenced by the laser irradiation. No cross-hatches were observed on the sample under Nomarski microscope. Fig. 4.7 shows low-temperature PL spectra of this sample. In the laser-irradiated area ***a*** the PL peak has a blue shift of about 214 Å with respect to spectrum (c). The integrated peak intensity is about half of that in the unirradiated area ***c***, and the FWHM of the PL peak changed from 10 meV in (c) to 24 meV in (a). In the laser-irradiated area ***b*** the PL peak has a blue shift of about 86 Å with respect to spectrum (c). The integrated peak intensity is about the same as that in the unirradiated area ***c***, and the FWHM of the PL peak is 18 meV in (b). The small blue shift in this case is not caused by the change of thickness but by the decrease of indium concentration, since there is no change of growth rate observed with or without laser irradiation. From the calculation, we conclude that the indium concentration is 32.5% in area ***a*** and 34% in area ***b***. Since 550°C is almost the optimal growth temperature for $In_{0.35}Ga_{0.65}As$, epitaxial growth at a higher temperature will degrade the property of the MQW structure. This is consistent

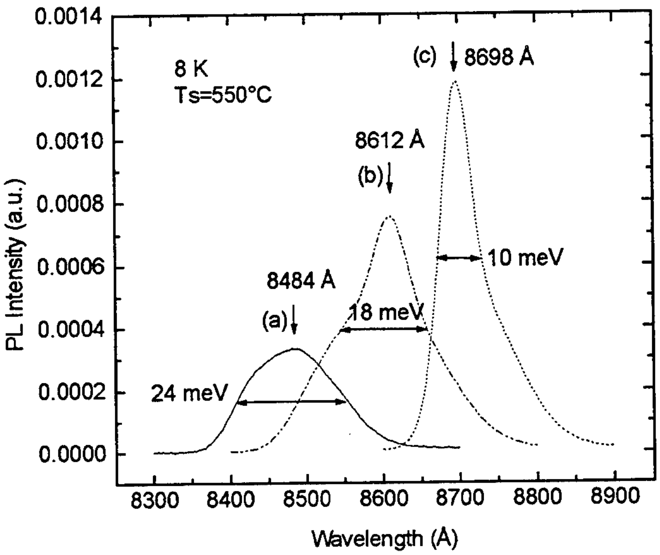

Fig. 4.7 Low temperature photoluminescence spectra of InGaAs/GaAs MQW structure grown at a substrate temperature of 550°C.

with the lower PL intensity and wider PL peak caused by the laser irradiation, which induces a temperature rise of about 20°C.

Laser irradiation is also expected to enhance desorption of both TEGa and TMIn. At low substrate temperature (500°C), 25 Å $In_{0.28}Ga_{0.72}As$ wells are grown in the laser-irradiated area, while 85 Å $In_{0.25}Ga_{0.75}As$ wells are grown in the nonirradiated area. The lower growth rate in the laser-irradiated area is caused by the enhanced desorption of TEGa and TMIn molecules. At high substrate temperature (550°C), laser irradiation has no effect on the quantum well thickness (20Å) and only a small effect on the indium composition (0.33 vs. 0.35). On the other hand, laser irradiation enhances desorption, and hence lowers the growth rate. French *et al.*[4.14] showed that indium loss by evaporation acts to limit the indium surface concentration at substrate temperatures greater than 550°C. A 20°C temperature rise caused by laser irradiation enhances indium loss from the surface, so the indium concentration on the surface would decrease and the reduction of growth rate due to indium segregation would be less. Therefore, the growth rate with laser irradiation should be higher than that without laser irradiation due to less indium segregation. In short, these two effects, enhanced desorption and less indium segregation, compensate each other and result in an unchanged growth rate and indium composition for the 550°C sample.

4.4 References

4.1 R. Iga, H. Sugiura and T. Yamada, Appl. Phys. Lett. *61*, 1423 (1992).

4.2 R. Iga, T. Yamada and H. Sugiura, Jpn. J. Appl. Phys. *32*, L473 (1993).

4.3 T. Yamada, R. Iga and H. Sugiura, Appl. Phys. Lett. *61*, 2449 (1992).

4.4 N. Chand, E. E. Becker, J. P. van der Ziel, S. N. G. Chu and N. K. Dutta, Appl. Phys. Lett. *58*, 1704 (1991).

4.5 K. Matsumura, D. Inoue, H. Nakano, M. Sawada, Y. Harada and T. Nakakado, Japan. J. Appl. Phys. *68*, L166 (1991).

4.6 H. K. Dong, S. C. H. Hung, C. W. Tu, Mat. Res. Soc. Proc. *340*, 193 (1994).

4.7 Y. Iimura, K. Nagata, Y. Aoyagi, S. Namba, J. Cryst. Growth *105*, 230 (1990).

4.8 E. T. FitzGerald, C. L. French and J. S. Foord, J. Cryst. Growth *120*, 57 (1992).

4.9 B. K. Tanner, Adv. X-ray Anal. *33*, 1 (1990).

4.10 D. C. Houghton, J. Appl. Phys. *70*, 2136 (1991).

4.11 D. C. Houghton, M. Davies, and M. Dion, Appl. Phys. Lett. *64*, 505 (1994).

4.12 P. J. Skevington and S. J. Amin, J. Cryst. Growth *120*, 135 (1992).

4.13 G. Bastard and J. A. Brum, IEEE J. Quantum Electron. *QE-22*, 1625 (1986).

4.14 C. L. French, A. T. S. Wee, and J. S. Foord, J. Cryst. Growth *107*, 1038 (1991).

5. Laser-Assisted CBE of GaAs Using a Novel Precursor

5.1 Introduction

Recently, great efforts have been undertaken to develop novel organometallic arsenic reagents as alternatives to AsH_3, which is highly toxic and compressed in high-pressure cylinders. Various liquid organometallic arsenic sources, such as phenylarsine ($PhAsH_2$)[5.1], triethylarsine[5.2], diethylarsine[5.3], tetraethylarsine[5.4], tertiarybutylarsine (TBA)[5.5], and trimethylarsine[5.6], have been explored. There are mainly three requirements for new precursors to be used in metalorganic molecular beam epitaxy (MOMBE) or chemical beam epitaxy (CBE), i.e., low but reasonable vapor pressure, low cracking temperature, and replacement of the As-H bond (which is believed to introduce the extremely toxic function) by other ligands. All of the alternatives mentioned above, except for TBA, yield a high carbon incorporation because of the direct As-C bonds, and hence are limited in applications. Successful growth of high-quality material has been achieved using TBA, but the precracking needed to break the carbon-arsenic bond still presents potential contamination problems.

Tris-dimethylaminoarsenic (TDMAAs, $As[N(CH_3)_2]_3$), with As directly bonded to N, has been proposed as another alternative source. Since there are no As-H and As-C direct bonds, one can expect TDMAAs to have lower carbon incorporation and lower toxicity. TDMAAs has been successfully used in MOMBE[5.7-14] and metalorganic chemical vapor deposition (MOCVD)[5.15,16] growth of GaAs or AlGaAs. Abernathy *et al.*[5.7,8] used triethylgallium (TEGa), trimethylamine alane (TMAAl) and TDMAAs to grow GaAs and AlGaAs without precracking TDMAAs. Their results showed that carbon concentrations measured by secondary ion mass spectrometry (SIMS) analysis in GaAs layers were lower than those obtained using a similar flux of AsH_3. In addition, carbon was reduced more than two orders of magnitude in GaAs films grown with trimethylgallium (TMGa) and

TDMAAs as compared to TMGa and AsH_3. Carbon incorporation was found to decrease as the substrate temperature increased. Koui *et al.*[5.10-14] studied the decomposition mechanism of TDMAAs using reflection high-energy electron diffraction (RHEED) and quadruple mass spectrometer (QMS). The temperature range for atomic layer epitaxy (ALE) using TEGa and TDMAAs is greatly expanded as compared to using TEGa and AsH_3. Salim *et al.*[5.17] have shown that TDMAAs decomposition over a GaAs surface starts at about 250°C, and is complete at about 360°C. Both Koui *et al.*[5.10] and Zimmermann *et al.*[5.15] observed n-type conductivity for GaAs epitaxial layers grown by MOMBE or MOCVD.

To date, the growth results with TDMAAs suggest that As-H bonds are not always necessary for low carbon incorporation, and that this nitrogen-containing reagent has a unique surface chemistry to getter carbon from metal alkyls. The underlying growth mechanism has not yet been verified. In this chapter, we report the study of GaAs growth and various characterizations of these GaAs films.

5.2 TDMAAs Decomposition

Salim *et al.*[5.17] and Xi *et al.*[5.18] have used mass spectrometry and Fourier transform infrared (FTIR) spectroscopy to study the gas-phase and surface decomposition of TDMAAs (carried by H_2). Their results indicate that the gas-phase decomposition of TDMAAs starts at about 350°C, and is complete at about 450°C. The decomposition products, dimethylamine ($HN(CH_3)_2$) and methylmethyleneimine ($CH_3N{=}CH_2$), appear as soon as TDMAAs starts to dissociate. An observed decrease in the concentration of the two products above 500°C is presumably caused by the decomposition of dimethylamine radicals to form methyl radicals and methyleneimine ($CH_2{=}NH$)[5.19]. The following reactions are proposed to happen in the pyrolysis process, which is consistent with the experimental data.

$$As(N(CH_3)_2)_n \rightarrow As(N(CH_3)_2)_{n-1} + \bullet N(CH_3)_2 \qquad (n=1\text{-}3) \tag{1}$$

$$\bullet N(CH_3)_2 + As(N(CH_3)_2)_n \rightarrow As(N(CH_3)_2)_{n-1} + HN(CH_3)_2 + CH_3N{=}CH_2 \tag{2}$$

$$\bullet N(CH_3)_2 + \bullet N(CH_3)_2 \rightarrow HN(CH_3)_2 + CH_3N{=}CH_2 \tag{3}$$

$$\bullet N(CH_3)_2 \rightarrow CH_2{=}NH + \bullet CH_3 \tag{4}$$

The TDMAAs pyrolysis behavior over a GaAs surface shows that decomposition starts at about 250°C, and is complete at about 360°C[5.17]. In this case, as reported by Xi *et al.*[5.18] in their temperature-programmed desorption (TPD) study, methylmethyleneimine could result from a β-hydride elimination process on the GaAs surface:

$$AsN(CH_3)_2 \rightarrow As + CH_3N{=}CH_2 + H\bullet \tag{5}$$

As we can see, reaction (5) provides an additional pathway for TDMAAs decomposition, and hence TDMAAs decomposition temperature is much lower on the GaAs surface than in the gas-phase. The atomic hydrogen released from the above reaction is very important for carbon reduction in GaAs epitaxial layers grown by CBE using TDMAAs, as will be discussed later.

In our study, we used both fully cracked and uncracked TDMAAs to investigate the growth, doping, and etching of GaAs. A quadruple mass spectrometry was used to record the mass spectra when TDMAAs was introduced into the chamber through the heated gas injector at different heating power. Figs. 5.1a and 5.1b show the mass spectra of uncracked and completely cracked TDMAAs, respectively. The mass peaks are assigned accordingly to different species, e.g., $AsN(CH_3)_2$ at 120, $AsNCH_3$ at 105, As at 75, As_2 at 150, CH_4 at 16, $CH_2{=}NH$ at 29, $HN(CH_3)_2$ at 45, and $CH_3N{=}CH_2$ at 43, as shown in the two figures. Gas-phase pyrolysis is responsible for TDMAAs decomposition in this case, and reactions (1)-(4) are involved. By comparing the two figures, we can see that the reactant peaks ($AsN(CH_3)_2$, $AsNCH_3$) totally disappear after cracking whereas the product peaks (As, As_2, CH_4, $CH_2{=}NH$, $HN(CH_3)_2$, and $CH_3N{=}CH_2$) increase significantly. Therefore, no amino-arsenic species are present when the cracked TDMAAs arrive at the GaAs surface, and hence no β-hydride elimination reaction will occur. In the

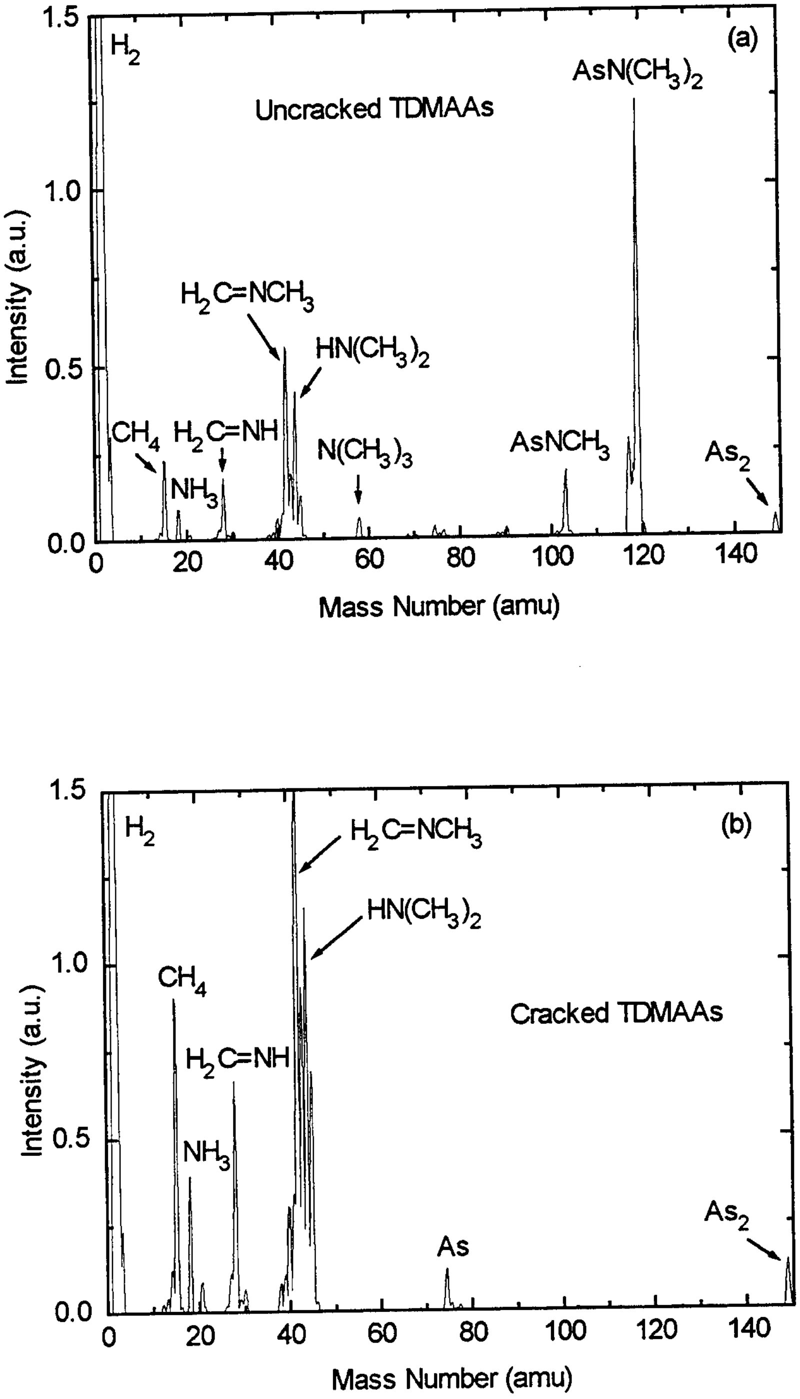

Fig. 5.1 Mass spectra resulting from (a) uncracked and (b) cracked TDMAAs.

following growth study, the same heating power, as was used in Fig. 5.1b, was employed to crack TDMAAs.

5.3 CBE of GaAs

We have used RHEED intensity oscillations to study the GaAs MOMBE growth behavior in the substrate temperature range of 300-550°C, where the TEGa flow rate was kept at 0.5 sccm and H_2 flow rate for TDMAAs at 2 sccm. Fig. 5.2 shows the GaAs growth rate as a function of substrate temperature, and the inserted figure shows typical Ga-induced RHEED intensity oscillations. Growth starts at about 350°C, and the growth rate increases as the substrate temperature increases until it reaches a stabilized value above 480°C. This temperature-independent growth rate region extends up to 550°C. When the growth temperature is above 550°C, it is difficult to observe RHEED intensity oscillations; therefore, the desorption-dominated region (the growth rate decreases at high temperatures) is not shown in this figure.

Fig. 5.3 shows the arsenic-controlled growth rate as a function of substrate temperature and the inserted figure shows the arsenic-induced RHEED intensity oscillations. The growth rate is almost constant as the substrate temperature changes from 370°C to 465°C, which indicates that TDMAAs decomposes completely below 370°C. This result agrees very well with the QMS result obtained by Salim et al.[5.17]. Hamaoka *et al.*[5.11], also demonstrated that the decomposition of TDMAAs on a GaAs surface was almost complete above 300°C. Therefore, we conclude that the complete decomposition of TDMAAs on a GaAs surface occurs at a substrate temperature between 300°C and 370 °C. When the substrate temperature is above 465°C, the arsenic incorporation rate decreases as the temperature increases. Under steady-state conditions, the product of the group V beam flux (F) and sticking coefficient (S) is the sum of incorporation (R_g) and desorption (R_d), i.e., $FS=R_g+R_d$. The desorption rate $R_d=ka_v$, where $k=A\exp(-E_d/kT)$, and

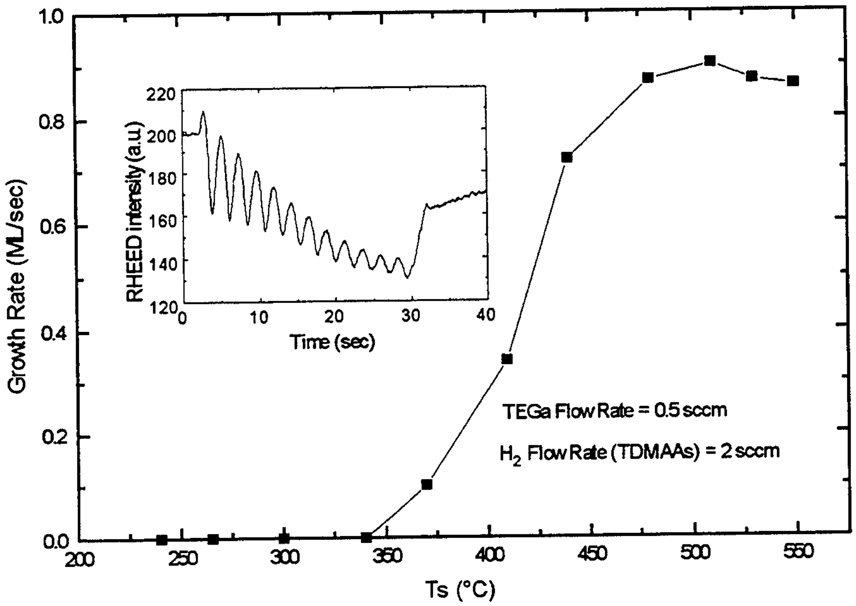

Fig. 5.2 GaAs growth rate as a function of substrate temperature with a TEGa flow rate of 0.5 sccm and a H_2 flow rate for TDMAAs of 2 sccm. The inserted figure shows the Ga-induced RHEED intensity oscillations.

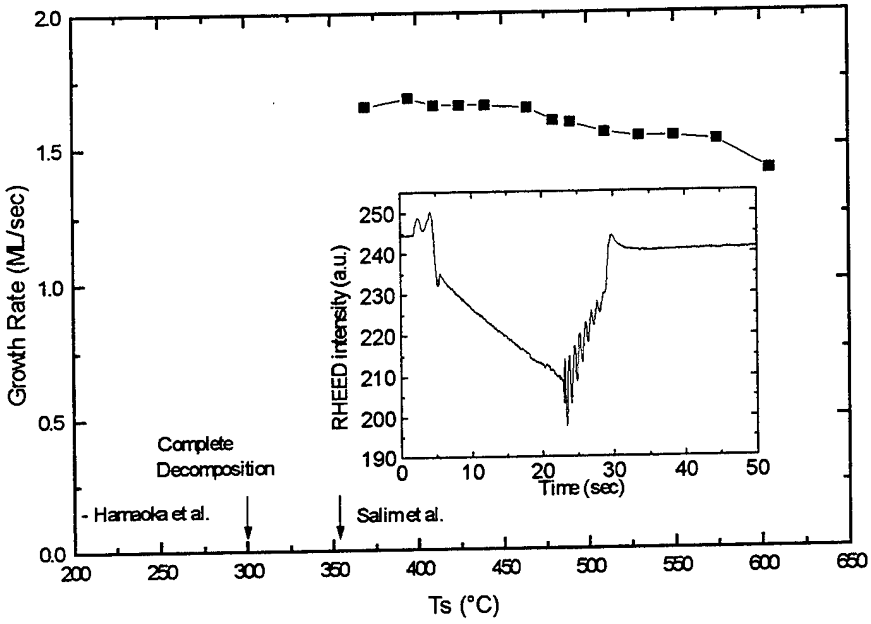

Fig. 5.3 Arsenic-controlled growth rate as a function of substrate temperature, with a TEGa flow rate of 0.5 sccm and a H_2 flow rate for TDMAAs of 2 sccm. The inserted figure shows the arsenic-induced RHEED intensity oscillations.

a_v is the group V surface atom activity[5.20]. Therefore, we can obtain the activation energy for TDMAAs desorption, E_a, from R_g as a function of substrate temperature in the high temperature range (465 to 605°C). The fitting to the experimental data gives an activation energy for TDMAAs desorption of 14 kcal/mol.

Based on the study of both group III- and group V-induced RHEED intensity oscillations, we can establish the actual V/III incorporation ratios on a substrate surface for different growth conditions. The GaAs growth rate was found to be affected by the V/III incorporation ratios, as shown in Fig. 5.4. The growth rate monotonically decreases as the V/III ratio increases, when the V/III ratio is greater than unity. This is probably due to the site-blocking effect, caused by excess arsenic atoms adsorbed on the GaAs surface, or the enhanced desorption of TEGa molecules from the GaAs surface at high arsenic surface concentration.

Thick GaAs epitaxial layers (2-3 μm) were grown at different substrate temperatures and V/III ratios, and were characterized by the standard Van der Pauw Hall effect measurement. In order to find out the influence of the source on the quality of the epitaxial material, two different batches of TDMAAs source were used. Specular surface morphologies were obtained for all the samples grown at V/III incorporation ratios greater than unity, regardless of the growth temperature.

Fig. 5.5 shows the dependence of the carrier concentration on the substrate temperature. For both TDMAAs sources without precracking, epitaxial layers grown at substrate temperatures above 490°C show n-type conduction, while films grown at lower temperatures show p-type conduction. SIMS measurements were used to characterize impurity levels in the epilayers. In all samples, H, C, N, O, Si, and S were analyzed. Low levels of C, Si and S were found, but no detectable level of H, N, or O was found in any of the epilayers. Fig. 5.6a and 5.6b show the SIMS profiles of a p-type sample grown at 440 °C and an n-type sample grown at 530°C using the Batch A TDMAAs source. The surface peaks are from exposure to air, and the interface peaks are from residual substrate

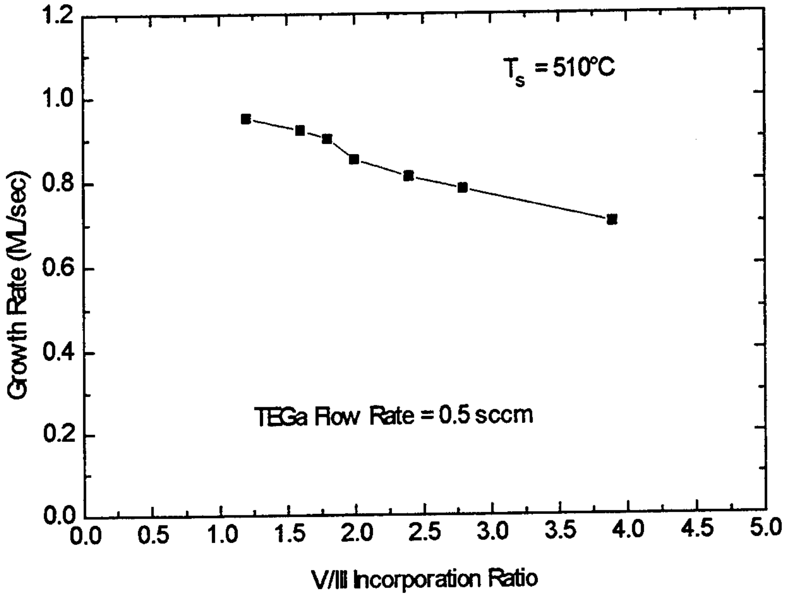

Fig. 5.4 GaAs growth rate as a function of V/III incorporation ratio, with a substrate temperature of 510°C and TEGa flow rate of 0.5 sccm.

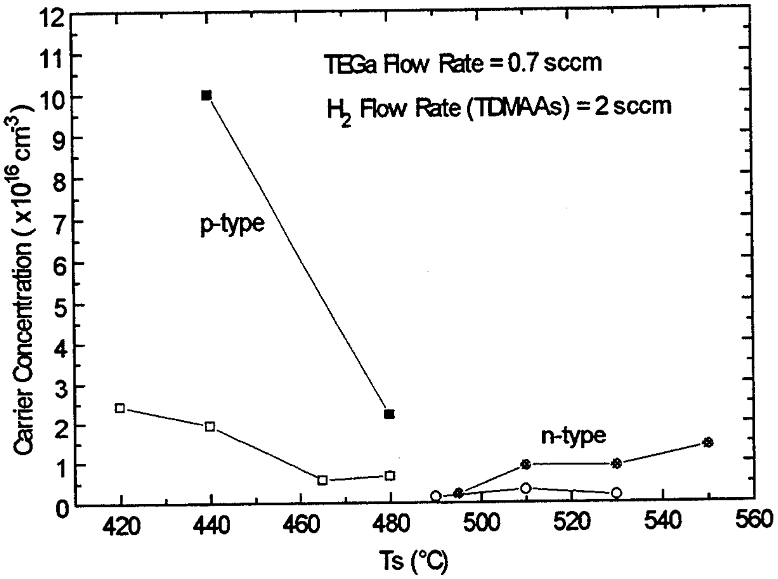

Fig. 5.5 The dependence of the carrier concentration on the substrate temperature. The TEGa and H_2 flow rates used for GaAs growth are 0.7 sccm and 2 sccm, respectively.

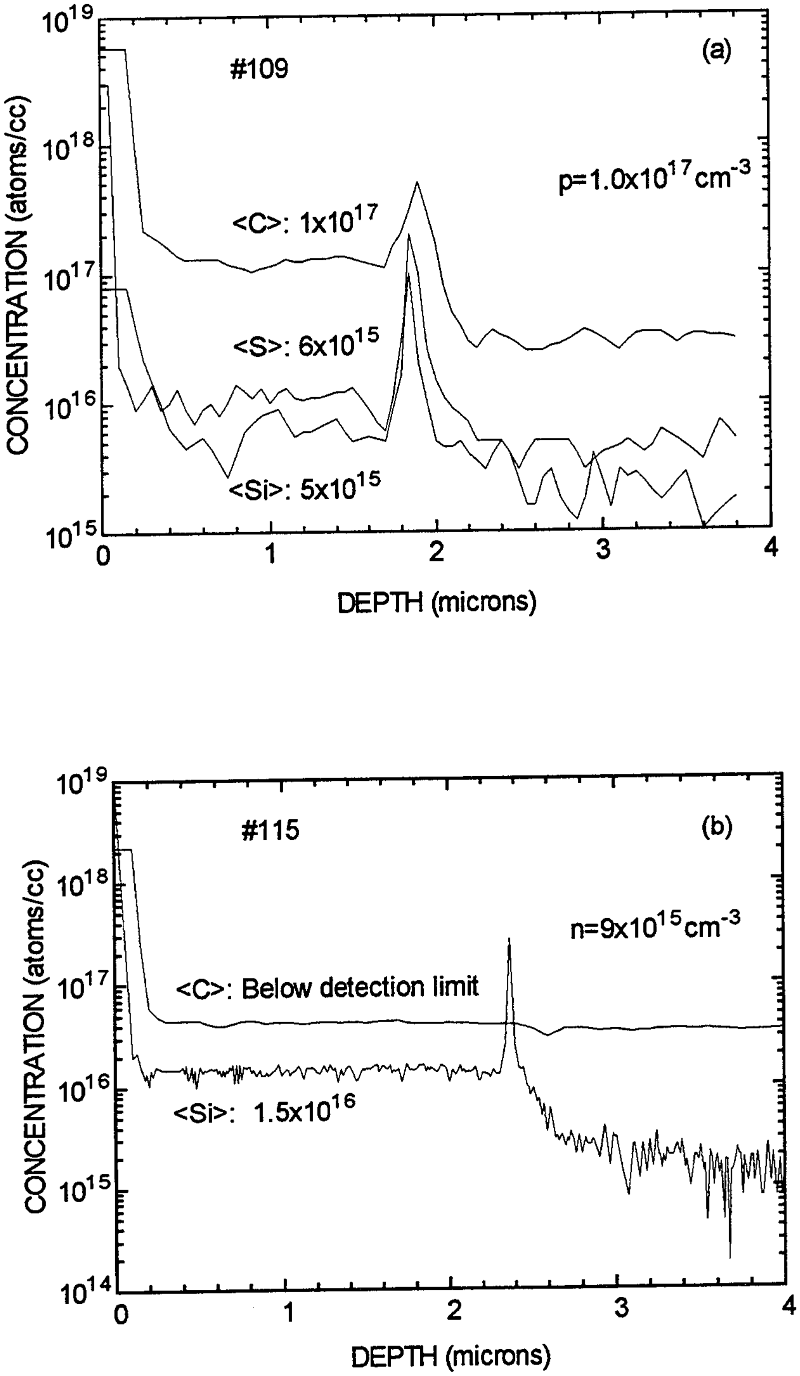

Fig. 5.6 (a) SIMS profile for the p-type GaAs sample grown at 440°C with a carbon concentration of 1×10^{17} cm^{-3}, a sulfur concentration of 6×10^{15} cm^{-3} and a silicon concentration of 5×10^{15} cm^{-3}. (b) SIMS profile for the n-type GaAs sample grown at 530°C with a silicon concentration of 1.5×10^{16} cm^{-3}.

impurities on the surface. A carbon concentration of 1.0×10^{17} cm^{-3}, along with a silicon concentration of 5×10^{15} cm^{-3} and a sulfur concentration of 6×10^{15} cm^{-3}, was found in the sample grown at 440°C, where the hole concentration was determined to be 1.0×10^{17} cm^{-3} by the Hall measurement. Presumably the p-type conduction of the film is caused by these carbon atoms but is compensated by donor impurities. The high degree of compensation is clearly seen from the low hole mobility for the p-type samples (211 cm^2/V·s for sample grown at 480°C and 32 cm^2/V·s at 440°C at 300 K). For sample grown at 530°C, a silicon concentration of 1.5×10^{16} cm^{-3} was found in the epilayer while the carbon concentration was below the SIMS detection limit. The electron concentration, determined by the Hall measurement, is 9×10^{15} cm^{-3}. Therefore, the n-type conduction is caused by the incorporation of silicon atoms. For samples grown by the Batch B TDMAAs source, SIMS measurements give similar results as those in Figs. 5.6a and 5.6b, but with much lower impurity concentrations.

From the above discussion, we see that 480°C is a critical temperature for the electrical property of the GaAs epilayers. As we noted in Fig. 5.2, the GaAs growth rate reaches a stabilized value at substrate temperatures above 480°C. Below 480°C, the growth rate increases as the substrate temperature increases, indicating that the TEGa molecules are not fully decomposed. Therefore, the ethyl radicals will incorporate into the lattice together with the gallium atoms. The lower the substrate temperature is, the more the ethyl radicals are incorporated, and hence the higher the carbon concentration will be. This is confirmed by the Hall and SIMS results as discussed above. When the substrate temperature is above 480°C, the TEGa molecules are fully decomposed, leaving ethyl radicals at the surface. It has been reported that the low carbon levels in GaAs samples grown with TDMAAs are a result of the efficient β-hydride elimination from the amide functionality[5.21]. The atomic hydrogen released from uncracked TDMAAs reacts with the ethyl species, minimizing ethyl transfer and/or decomposition into surface ethylene and carbon. Therefore, the carbon concentration is much lower at higher substrate temperatures. However, as the substrate temperature increases, the silicon incorporation, which possibly comes from the decomposition of residual silane in the TDMAAs source, increases significantly. Therefore, the electron concentration increases as the growth temperature increases. This is also confirmed by the experimental results. However, when we thermally crack TDMAAs molecules using a heating cell, we get p-type conduction with a hole concentration of about 9×10^{16} cm^{-3}, even at a substrate temperature of 530°C. This is because that the β-hydride elimination process is suppressed when TDMAAs is cracked as discussed in Section 5.1.

The electrical property is also influenced by V/III incorporation ratios, and the best results were obtained at a V/III ratio of 1.6-2.0. A higher V/III ratio introduces more gettering centers for carbon uptake, and hence lowers the carbon incorporation. Therefore, the electrical property is not as good when the V/III ratio is lower than 1.6. When the V/III ratio is too high, more silicon species from the TDMAAs source could be incorporated into the film, and hence the electron concentration in the GaAs epilayer increases.

Fig. 5.7 shows the variable temperature Hall-measurement result of a GaAs sample grown at 480°C. For a nondegenerate p-type semiconductor with an acceptor concentration N_A, a donor concentration N_D, and an acceptor activation energy E_a, the theoretical hole concentration p in the valence band at a temperature T, is given by[5.22]

$$\frac{p(p+N_D)}{(N_A-N_D-p)}=\frac{N_v}{G}\exp\left(\frac{-E_a}{k_BT}\right)$$

where G is the acceptor degeneracy factor; k_B is the Boltzmann constant; and N_v is the density of states in the valence band.

A computer simulation by adjusting N_A, N_D, and E_a to minimize the error between the calculated value and the experimental value was performed to determine these three parameters. No good fitting can be achieved if N_D is greater than 1×10^{14} cm^{-3}. From the Hall results, we know that the sample is highly compensated. There must exist some

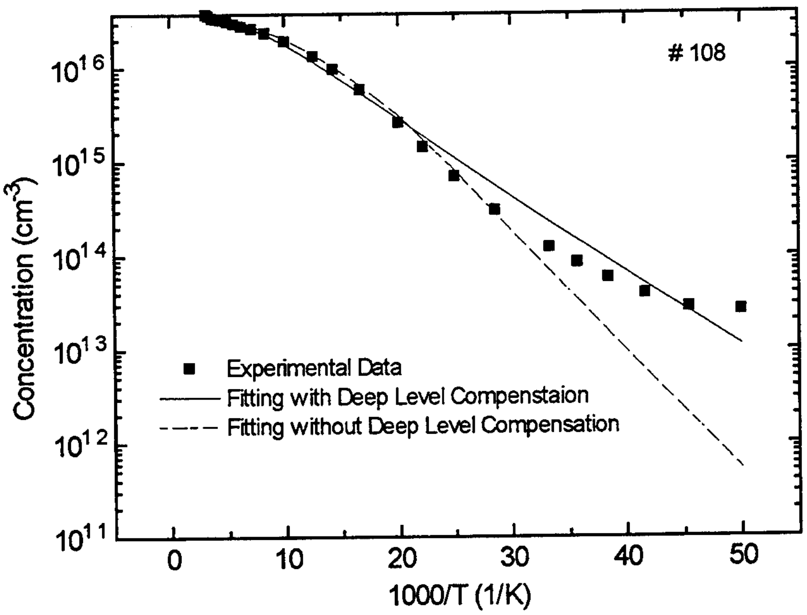

Fig. 5.7 Variation of the hole concentration with temperature for the GaAs sample grown at 480°C.

shallower acceptors so that the electrons from the donor states will first compensate the holes from these acceptor states. In fact, an effective donor concentration N_D^* (after compensation by shallower acceptors) was used in our simulation. A simulation without considering the deep level compensation is also plotted in the figure. The best fit to the experimental data gives N_A=3.7x10^{16} cm^{-3}, N_D=2.0x10^{13} cm^{-3}, and E_a=28 meV. The acceptor activation energy is very close to the carbon acceptor ionization energy (27.6 meV)[5.23]. Therefore, we conclude that the carbon acceptor concentration in the sample determines the p-type conduction.

The 300 K and 77 K Hall mobility for the samples grown with TEGa and TDMAAs is plotted as a function of electron concentration determined from Hall measurements in Figs. 5.8a and 5.8b, respectively. Also plotted in Fig. 5.8a are the 300 K Hall data from CBE work of Koui *et al.*[5.10] (TEGa, TDMAAs) and an empirical fit to the 300 K results from Si-doped MBE-grown layers presented by Hilsum[5.24]. Similarly, the 77 K Hall data from the MOCVD work of Zimmermann *et al.*[5.15] (TMGa, TDMAAs) and the empirical curve of Stillman and Wolfe[5.25] are included in Fig. 5.8b. Compared to these reported values, the samples from our work show the best electrical property for GaAs grown using TDMAAs. The improvement may be related to the source purity, system cleanliness, and better growth condition. In addition, the results from Batch B TDMAAs show higher Hall mobilities and lower electron concentrations than those from Batch A TDMAAs. This should be due to the difference in source purity. With Batch A TDMAAs, at a substrate temperature between 510°C and 530°C, and a V/III ratio of about 1.6-2.0, the unintentional doping concentration is n~1x10^{16} cm^{-3} with an electron mobility of 5,200 cm^2/V·s at 300 K and 16,000 cm^2/V·s at 77 K. With Batch B, at a substrate temperature between 490°C and 510°C, and a V/III ratio of about 1.6, the highest mobility we obtained is 5,700 cm^2/V·s at 300 K and 40,000 cm^2/V·s at 77 K with an electron concentration of about 1x10^{15} cm^{-3}.

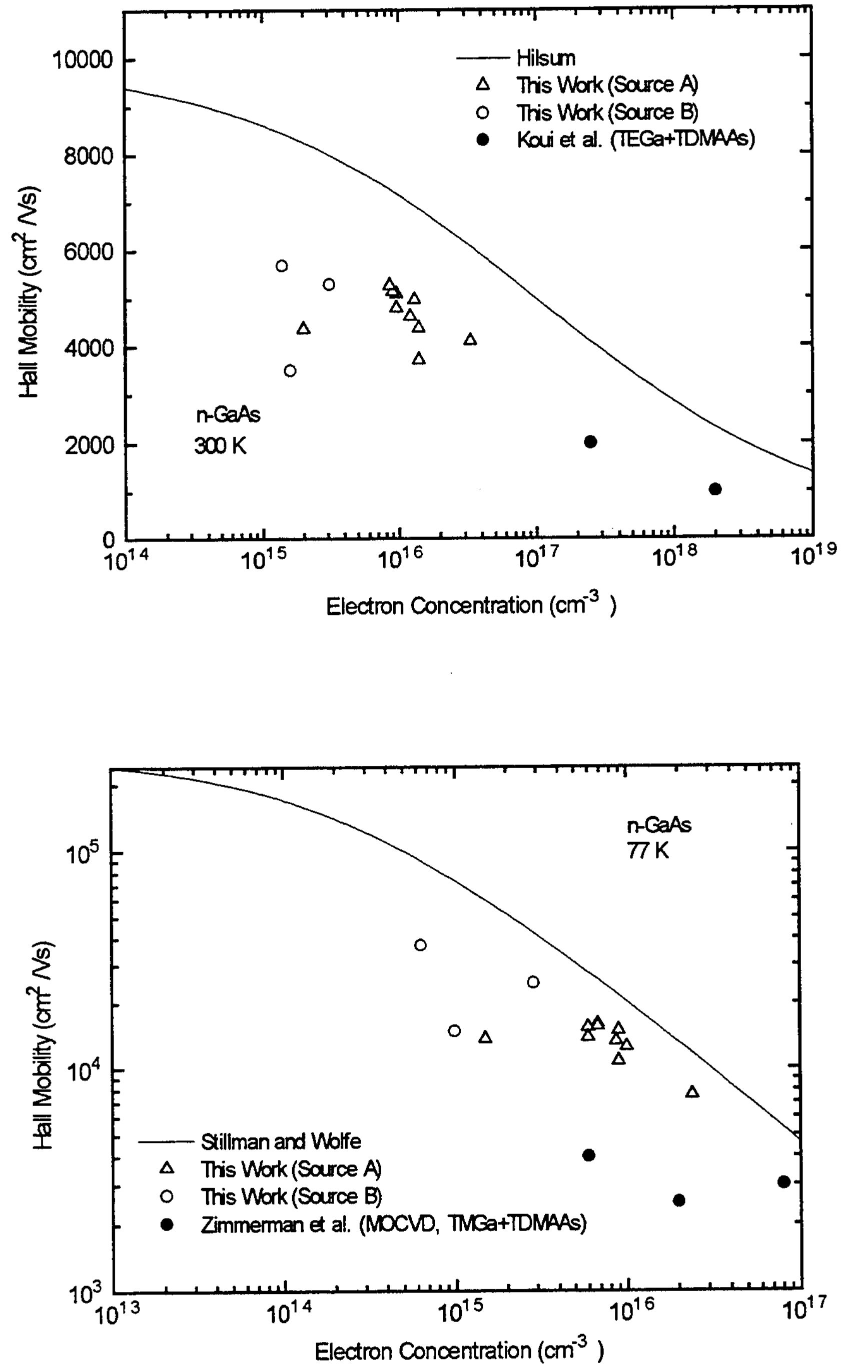

Fig. 5.8 (a) Concentration dependence of the Hall mobility in n-GaAs at 300 K.
(b) Concentration dependence of the Hall mobility in n-GaAs at 77 K.

5.4 Laser-Assisted CBE of GaAs

The effect of argon ion laser irradiation on CBE growth of GaAs was studied next. Both the 488 nm and 351 nm lines of a multiline 5-watt argon ion laser were used. To obtain the 351 nm line a UV optics was installed. The laser spot was focused to about 300 μm. The substrate temperature dependence of the growth rates of irradiated and unirradiated areas from this work, together with those using arsine[5.26] and solid arsenic[5.27], are shown in Fig. 5.9. The growth rate data are normalized to that at the high-temperature region (between 480°C and 510°C). The TEGa and H_2 (for TDMAAs) flow rates were 0.4 and 2 sccm, respectively. The laser power density used for all cases is about 400 W/cm^2, except that for 351 nm UV line is only 20 W/cm^2. The substantial differences between the laser-assisted growth using TDMAAs and arsine or solid arsenic are that the threshold temperature for enhanced growth is about 100°C lower and that the temperature range is about 100°C wider (more noticeable for the 488 nm line). Furthermore, there are two different substrate-temperature regions for laser-enhanced growth using the 488 nm line, 340 to 440°C and 265 to 340°C, as indicated by (a) and (b), respectively, in Fig. 5.9.

Based on the surface reaction models proposed by Robertson *et al.*[5.28], Liang and Tu[5.29], and Martin and Whitehouse[5.30], the rate-limiting reaction for GaAs growth is expected to be the reaction between diethylgallium (DEGa) and arsenic species. Therefore, the growth rate depends on the surface DEGa concentration. We propose that the growth enhancement in the higher temperature region (340 to 440°C) is determined by the enhanced DEGa formation due to laser-induced heating of about 20-25°C (calculated from a heat-flow equation and confirmed by infrared laser interferometry[5.27, 5.31]) and that in the lower temperature region (265 to 340°C) is determined by an additional chemical reaction between TEGa and TDMAAs or its decomposed arsenic species. In the higher temperature region, the activation energy of the GaAs deposition rate determined from the graph is 62 Kcal/mol, which is close to the bonding energy of Ga-C_2H_5 (59 Kcal/mol).

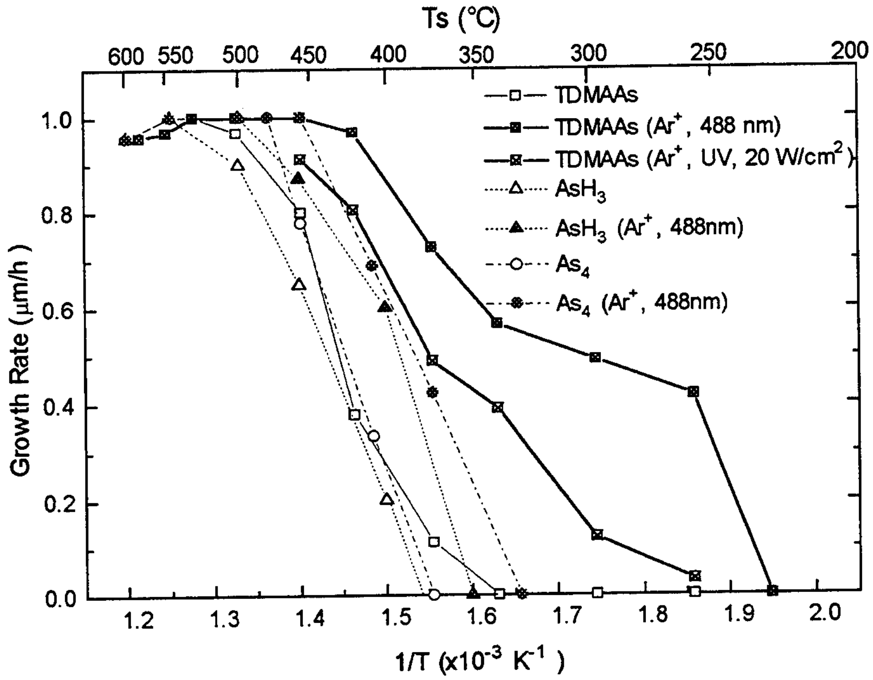

Fig. 5.9 The substrate temperature dependence of growth rates of laser-irradiated and non-irradiated areas. The solid lines denote the growth data obtained using TDMAAs, while the dashed and dotted lines denote the data from AsH_3 and As_4, respectively.

This value is also close to that in laser-assisted growth using AsH_3 or As_4. Therefore, in this region the growth rate enhancement is dominated by laser-enhanced decomposition of TEGa to form DEGa. In the lower temperature region, however, the activation energy is much smaller, 26 Kcal/mol, which is too small for TEGa decomposition. Therefore, a photocatalytic or photochemical reaction must have taken place, but its nature cannot be known without additional spectroscopic investigation. In the laser-assisted CBE growth of GaAs using AsH_3 or As_4, there is no similar photo-enhanced chemical reaction because only As dimers or tetramers are on the surface.

All of the selectively grown GaAs spots show a specular surface, and the surface morphology is independent of the substrate temperature and the laser power density in the range studied. Fig. 5.10a and 5.10b show a Nomarski micrograph and the cross-section profile of a line pattern generated by scanning the laser beam at about 2 Hz with a power density of 550 W/cm^2. The pattern, 0.5 mm x 2 mm, was grown at a substrate temperature of 340°C and shows a featureless morphology. The growth rate of the line pattern is the same as that of the spot pattern without laser-beam scanning. However, when we increase the scan length to 5 mm, the growth rate of the line pattern is lower than that of the spot pattern without laser-beam scanning. This indicates that the selective-area growth rate is limited by the laser-beam scan rate. By increasing the scan rate, the growth rate of line was found to become closer to the spot growth rate.

The laser-enhanced growth rate depends strongly on the laser power density. Fig. 5.11 shows the relationship between laser power density and the spot growth rate. The growth study was performed at a substrate temperature of 340°C with a TEGa flow rate of 0.5 sccm and a H_2 flow rate (TDMAAs) of 2 sccm. The growth rate increases as the laser power density increases and tends to saturate at high laser power density. This is similar to the results obtained with laser-assisted growth of GaAs using AsH_3[5.26] or As_4[5.27]. The growth rate saturation may be due to the complete decomposition of TEGa at high laser power density.

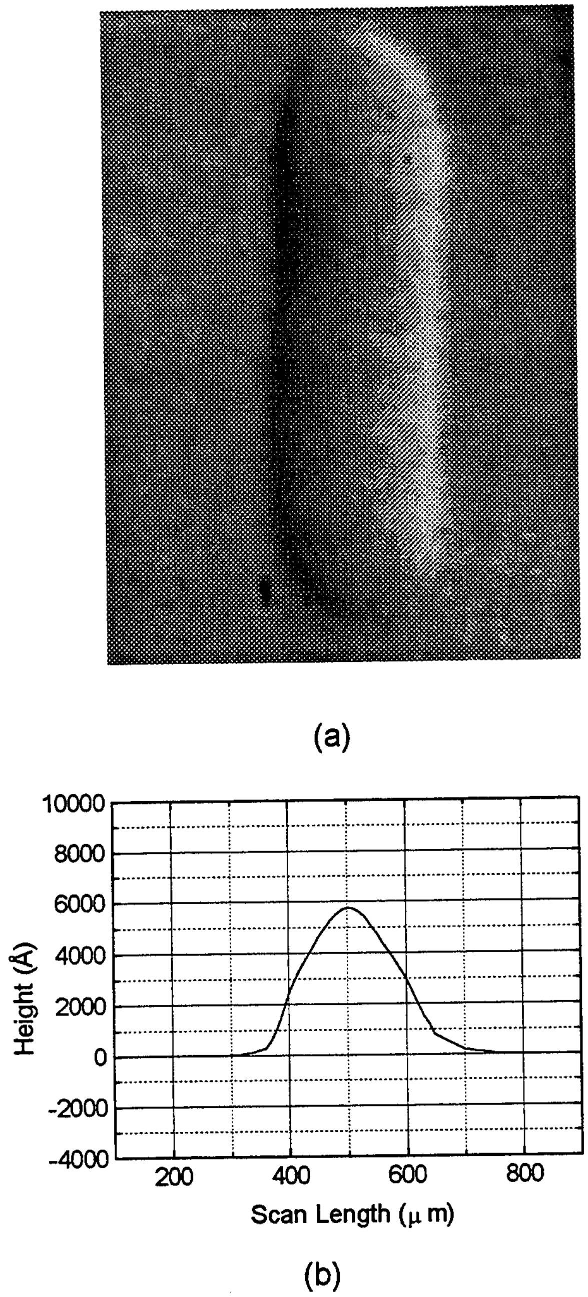

Fig. 5.10 (a) Nomarski micrograph (60x) of the GaAs line pattern grown by Ar-ion-laser-assisted CBE with the laser beam scanning at about 2 Hz and a laser power density of 550 W/cm^2. (b) The cross-section profile of the line pattern measured by a Dektak stylus profiler.

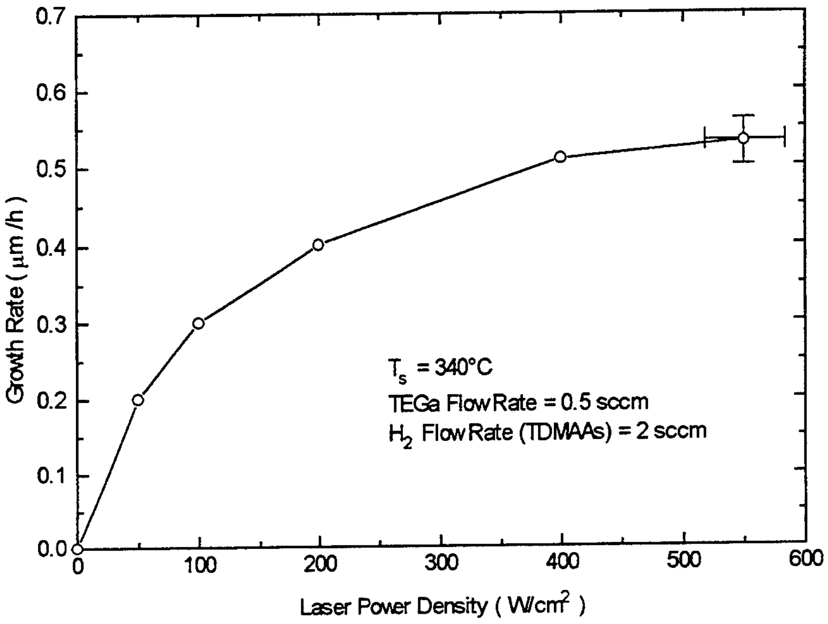

Fig. 5.11 The growth rate dependence of the laser power density at a substrate temperature of 340°C. The TEGa and H2 flow rates used for GaAs growth are 0.5 sccm and 2 sccm, respectively.

Fig. 5.12 shows an X-ray rocking curve of GaAs grown with or without laser irradiation and similarly low-temperature PL spectra. We see that the X-ray line width is only 15 arcsec, and the two cases give an identical rocking curve, indicating high structural perfection of laser-irradiated sample. (The substrate line width is 13 arcsec.) In the PL spectra the two peaks at wavelengths of 821 and 830 nm are assigned to excitons bound to neutral carbon acceptors (A^0X) and transitions between the conduction band and neutral carbon acceptors (eC^0), respectively. We see that laser irradiation improves the optical quality of GaAs films grown at low substrate temperatures. At a slightly higher substrate temperature, the bound exciton peak of the laser-irradiated region can be even much larger. One interesting point to note is the large carbon related peak of the laser-irradiated sample, which indicates that laser irradiation may crack TDMAAs, resulting in high carbon incorporation[5.32].

5.5 References

5.1 A. Schütze, J. Zacheja, M. Weyers and D. Kohl, J. Cryst. Growth *107*, 1036 (1991).

5.2 G. A. Miller, Solid State Technol. August, 59 (1989).

5.3 G. B. Stringfellow, J. Electron. Mater. *17*, 327 (1988).

5.4 A. Brauers, O. Kayser, R. Kall, H. Heinecke, P. Balk and H. Hofmann, J. Cryst. Growth *93*, 7 (1988).

5.5 R. Bhat, M. A. Koza, and B. J. Skromme, Appl. Phys. Lett. *50*, 1194 (1987).

5.6 H. J. Moon, T. G. Stoebe and B. K. Chadwick, J. Electron. Mater. *19*, 1351 (1990).

5.7 C. R. Abernathy, P. W. Wisk, D. A. Bohling, and G. T. Muhr, Appl. Phys. Lett. *60*, 2421 (1992).

5.8 C. R. Abernathy, P. W. Wisk, S. J. Pearton, F. Ren, D. A. Bohling, and G. T. Muhr, J. Cryst Growth *124*, 64 (1992).

5.9 S. Salim, J. P. Lu, K. F. Jensen, and D. A. Bohling, J. Cryst. Growth *124*, 16 (1992).

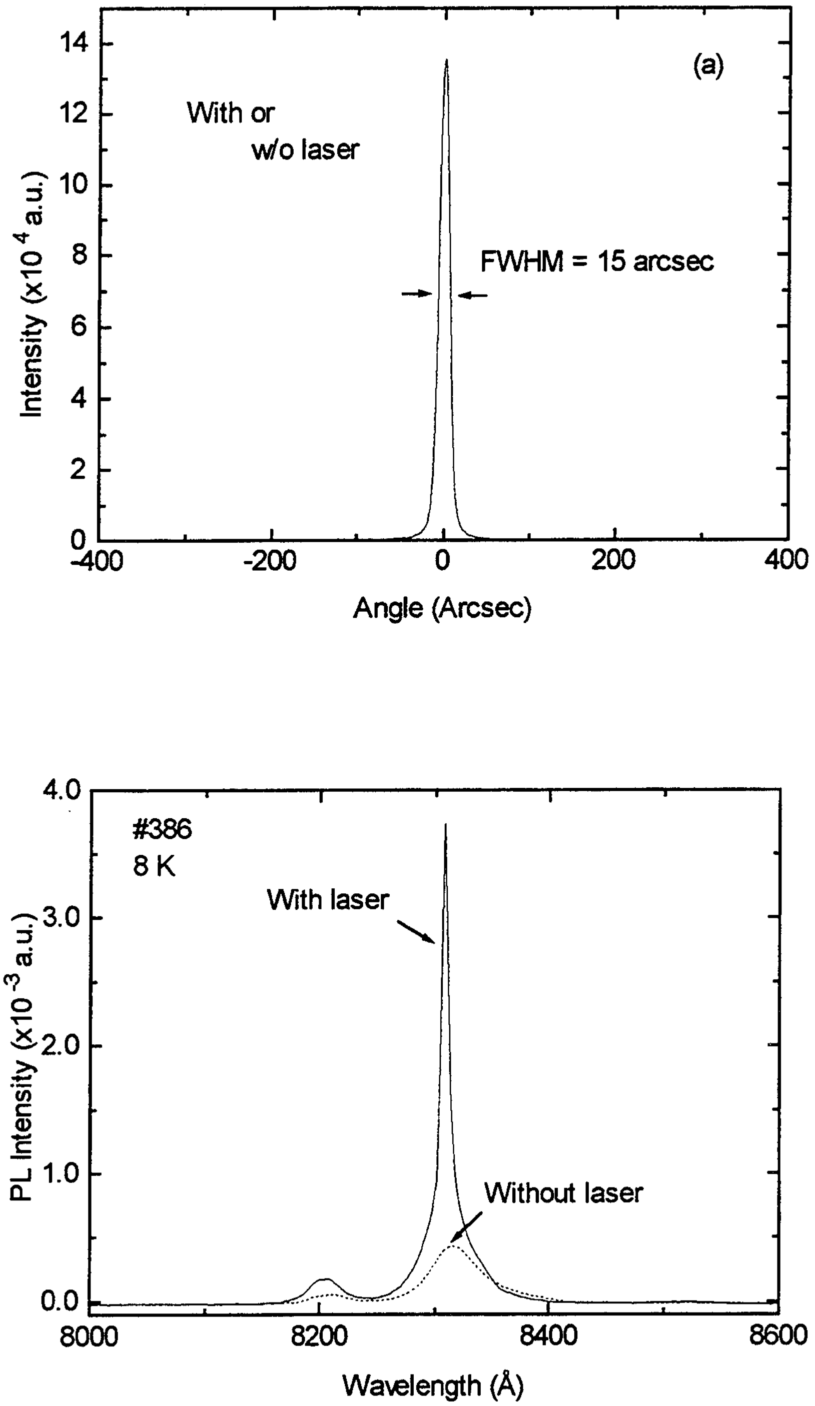

Fig. 5.12 (a) X-ray rocking curves, and (b) low-temperature PL spectra of GaAs grown with or without argon ion laser irradiation.

5.10 T. Koui, I. Suemune, K. Hamaoka, K. Fujii, A. Kishimoto, Y. Honda, and M. Yamanishi, Extended Abstracts of the 1991 International Conference on Solid State Devices and Materials, Yokohama, p. 408 (1991).

5.11 K. Hamaoka, I. Suemune, K. Fujii, T. Koui, A. Kishimoto, and M. Yamanishi, Jpn. J. Appl. Phys. *30*, L1579 (1991).

5.12 K. Fujii, I. Suemune, and M. Yamanishi, Appl. Phys. Lett. *61*, 2577 (1992).

5.13 K. Fujii, I. Suemune, T. Koui, and M. Yamanishi, Appl. Phys. Lett. *60*, 1498 (1992).

5.14 T. Koui, I. Suemune, K. Miyakoshi, K. Fujii, and M. Yamanishi, Jpn. J. Appl. Phys. *31*, L1272 (1992).

5.15 G. Zimmermann, H. Protzmann, T. Marschner, O. Zsebök, W. Stolz, E. O. Göbel, P. Gimmnich, J. Lorberth, T. Filz, P. Kurpas, and W. Richter, J. Cryst. Growth *129*, 37 (1993).

5.16 M. H. Zimmer, R. Hövel, W. Brysch, A. Brauers, J. Cryst. Growth *107*, 348 (1991).

5.17 S. Salim and K. F. Jensen, to be published in Chemistry of Materials (1995).

5.18 M. Xi, S. Salim, K. F. Jensen, and D. A. Bohling, Mater. Res. Soc. Proc. *334*, 169 (1994).

5.19 J. Seetula, K. Kalliorinne, and J. Koskikallio, J. Photochem. Photobio. *A43*, 31 (1988).

5.20 B. W. Liang, H. Q. Hou, and C. W. Tu, Mater. Res. Soc. Symp. Proc. *222*, 145 (1991).

5.21 D. A. Bohling, C. R. Abernathy, and K. F. Jensen, J. Crystal Growth *136*, 118 (1994).

5.22 D. E. Hill, J. Appl. Phys. *41*, 1815 (1970).

5.23 M. H. Kim, S. S. Bose, B. J. Skromme, B. Lee, and G. E. Stillman, J. Electron. Mater. *20*, 671 (1991).

5.24 C. Hilsum, Electron Lett. *10*, 259 (1974).

5.25 G. E. Stillman and C. M. Wolfe, Thin Solid Films *31*, 69 (1976).

5.26 H. Sugiura, R. Iga, and T. Yamada, J. Cryst. Growth *120*, 389 (1992).

5.27 H. K. Dong, B. W. Liang, M. C. Ho, S. Hung and C. W. Tu, J. Crystal Growth *124*, 181 (1992).

5.28 R. Robertson, Jr., T. H. Chiu, W. T. Tsang, and J. E. Cunningham, J. Appl. Phys. *64*, 877 (1988).

5.29 B. W. Liang and C. W. Tu, Appl. Phys. Lett. *57*, 689 (1990).

5.30 T. Martin, and C. R. Whitehouse, J. Cryst. Growth *105*, 57 (1990).

5.31 S. C. H. Hung, H. K. Dong, and C. W. Tu, Mater. Res. Soc. Symp. Proc. *340*, 35 (1994).

5.32 H. K. Dong, N. Y. Li, W. S. Wong, and C. W. Tu, submitted to Appl. Phys. Lett. (1995).

6 Laser-Modified CBE of InGaAs/GaAs MQWs

6.1 RHEED Study on CBE of InGaAs

Epitaxially grown InGaAs/GaAs pseudomorphic strained-layer heterostructures are very important because of their potential applications in high-speed transistors[6.1] and optoelectronic devices[6.2]. The feasibility of using TDMAAs in growing these structures was also investigated. $In_xGa_{1-x}As/GaAs$ MQW structures (10 periods) were grown using cracked or uncracked TDMAAs at different substrate temperatures (440-550°C). During growth, the flow rates of TEGa and TMIn were kept at 0.4 and 0.06 sccm, respectively, and the hydrogen flow rate for TDMAAs was 2 sccm. The growth was interrupted for 10 seconds between wells and barriers with TDMAAs supplied constantly.

Good InGaAs/GaAs interfaces can be achieved using cracked TDMAAs for the substrate temperature range studied, as indicated by the sharp satellite peaks in the XRC graph (curve a) of an InGaAs/GaAs MQW in Fig. 6.1. Since carbon incorporation is higher with cracked TDMAAs, it is desirable to grow these structures with uncracked TDMAAs. In order to obtain a good interface for InGaAs/GaAs MQWs using uncracked TDMAAs, the substrate temperature must be lower, within the range of 440-500°C. As shown in Fig. 6.1, the sample grown at 550°C shows only two broad peaks apart from the substrate peak (curve b), indicating poor interfaces. From RHEED study of InGaAs on GaAs using TDMAAs[6.3], we found that the InGaAs growth is non-uniform as time proceeds when the substrate temperature is higher than 500°C. Apart from the non-uniform InGaAs well growth, the etching effect of uncracked TDMAAs could also be a source of roughening the InGaAs/GaAs interfaces. For the $In_xGa_{1-x}As/GaAs$ MQWs grown at different substrate temperatures from 440 to 500°C, the indium composition varies from 20 to 25% while the InGaAs well thickness varies from 32 to 50 Å. However, the structures we grew are still within the stable limit from the calculation based on the

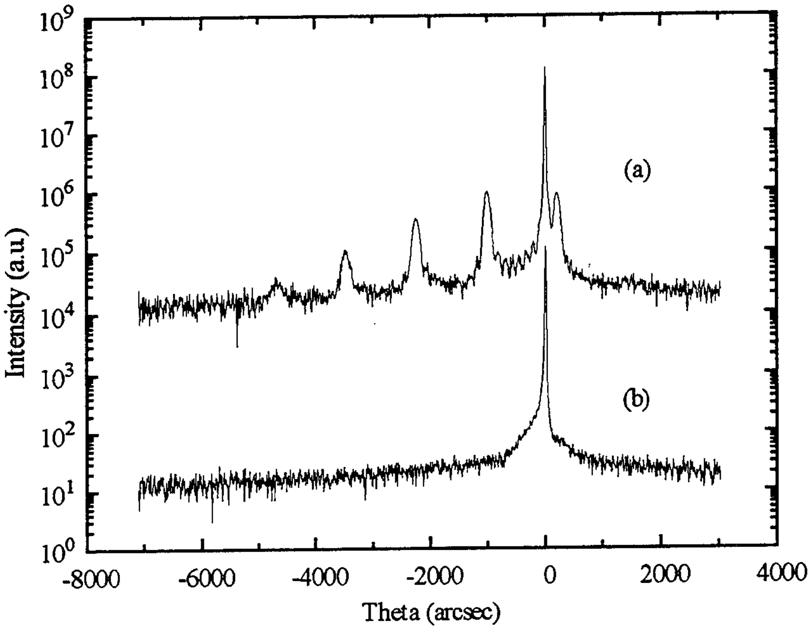

Fig. 6.1 X-ray rocking curves for InGaAs/GaAs MQWs grown at 550°C with (a) cracked TDMAAs, and (b) uncracked TDMAAs.

model proposed by Houghton *et al.*[6.4, 6.5]. This tells us that the pseudomorphic condition was maintained for all the MQW structures. From low-temperature photoluminescence (PL) measurements, the full width at half maximum (FWHM) of the PL exciton peak decreases as the substrate temperature increases. This is due to a better crystal quality at higher growth temperature. The smallest FWHM obtained is 6.5 meV at 500°C.

In CBE growth of InGaAs, the group III fluxes are not simply additive because of the complicated surface chemical reactions which involve all species (TEGa, TMIn, TDMAAs and their decomposed species). In our earlier MOMBE study of InGaAs using TMIn, TEGa, and As_4[6.6], we have found that the InGaAs growth rate decreases with time to a stabilized value, and is lower for higher substrate temperature or higher TMIn flow rate. Surface segregation of indium during growth and a lower sticking coefficient of TEGa molecules on an indium-covered surface are believed to be the reason that the InGaAs growth rate becomes lower than that of GaAs with the same TEGa flow rate and arsenic supply. Here in CBE using TDMAAs, both the substrate temperature and the TMIn flow still play important roles. In order to find the optimal growth condition of InGaAs/GaAs MQWs, we also use RHEED intensity oscillations to study the InGaAs growth behavior at different conditions.

Fig. 6.2 shows the RHEED intensity oscillation data for InGaAs grown on a (100) GaAs substrate at substrate temperatures of 500 and 525°C with flow rates of TEGa, TMIn, and H_2 (for TDMAAs) kept at 0.4, 0.06, and 2 sccm, respectively. As we can see, when the substrate temperature is at 500°C (or lower), the RHEED oscillations last within the entire 40-second growth time. However, when the temperature is at 525°C (or higher), the oscillations disappear at about 20 seconds after the introduction of TMIn and TEGa and the RHEED intensity increases gradually afterwards possibly because the surface structure changes gradually as indium segregation happens. In Fig. 6.3, we plot the growth rate of InGaAs at each period of intensity oscillation versus the number of oscillations. The transient growth behavior for InGaAs grown at a substrate temperature

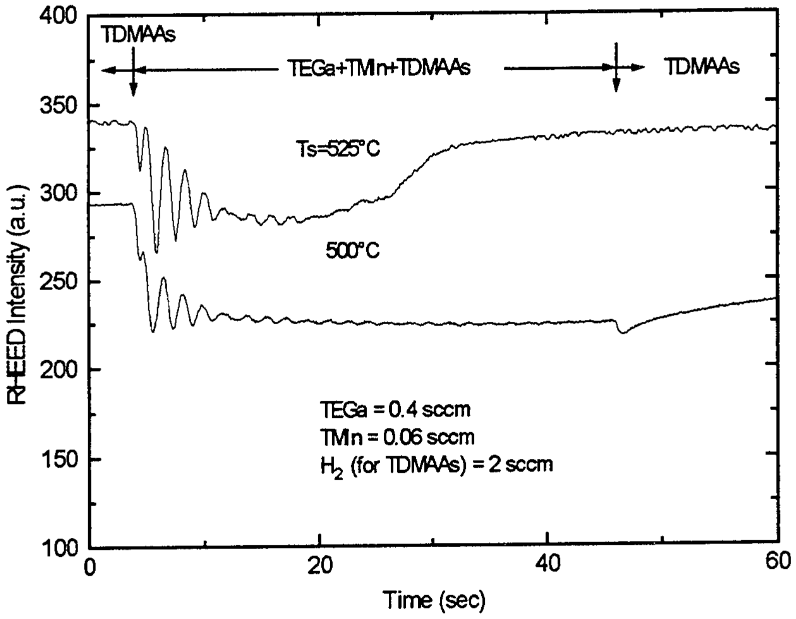

Fig. 6.2 The RHEED intensity oscillation data for InGaAs grown on a (100) GaAs substrate at substrate temperatures of 500 and 525°C with flow rates of TEGa, TMIn, and H2 (for TDMAAs) kept at 0.4, 0.06, and 2 sccm, respectively.

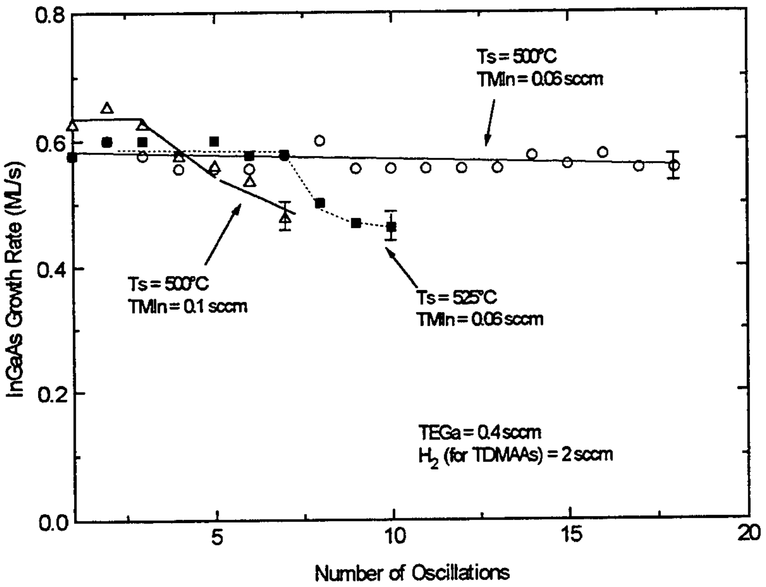

Fig. 6.3 The growth rate of InGaAs at each period of intensity oscillation versus the number of oscillations.

of 500°C and a TMIn flow rate of 0.1 sccm is also included. For InGaAs grown at 500°C (or lower) with a TMIn flow rate of 0.06 sccm, the growth rate is almost constant as time proceeds. This implies that the ternary growth is quite uniform throughout the 40-second growth time. When the growth temperature is changed to 525°C while keeping the TMIn flow rate at 0.06 sccm, or when the TMIn flow rate is changed to 0.1 sccm while keeping the substrate temperature at 500°C, the InGaAs growth rate will start to decrease gradually after seven or eight RHEED intensity oscillations, respectively. Therefore, the growth is non-uniform as time proceeds when the substrate temperature is too high (>500 °C) or when the TMIn flow rate is too high (>0.06 sccm). The lower InGaAs growth rate is caused by surface segregation of indium during growth and a lower sticking coefficient of TEGa molecules on an indium-covered surface. Since the TEGa and TMIn flow rates became stabilized within 4-5 seconds after the run/vent switch, only 1-2 oscillations were affected by the flow transient. From the above discussion, we conclude that we should keep the substrate temperature at 500°C or lower and the TMIn flow rate at 0.06 sccm or less during the CBE growth of InGaAs in order to maintain a uniform InGaAs growth.

The RHEED study is also confirmed by the X-ray rocking curve results for InGaAs/GaAs MQWs grown at various conditions. For the samples grown at high substrate temperatures (525 or 550°C) or at high TMIn flow rates (0.1 sccm or higher), no satellite peaks were observed in the XRC graph. As shown in Fig. 6.4, the sample grown at 500°C shows sharp satellite peaks indicating good InGaAs/GaAs interfaces, while the sample grown at 525°C shows only two broad peaks (apart from the substrate peak), indicating poor interfaces. The poor InGaAs/GaAs interfaces are probably due to the non-uniform InGaAs well growth. The etching effect of TDMAAs as discussed in section 7.3 could also be a source of roughening the InGaAs/GaAs interfaces. Therefore, in order to obtain good interfaces for InGaAs/GaAs MQWs, laser-modified CBE was performed only at substrate temperatures from 440°C to 500°C.

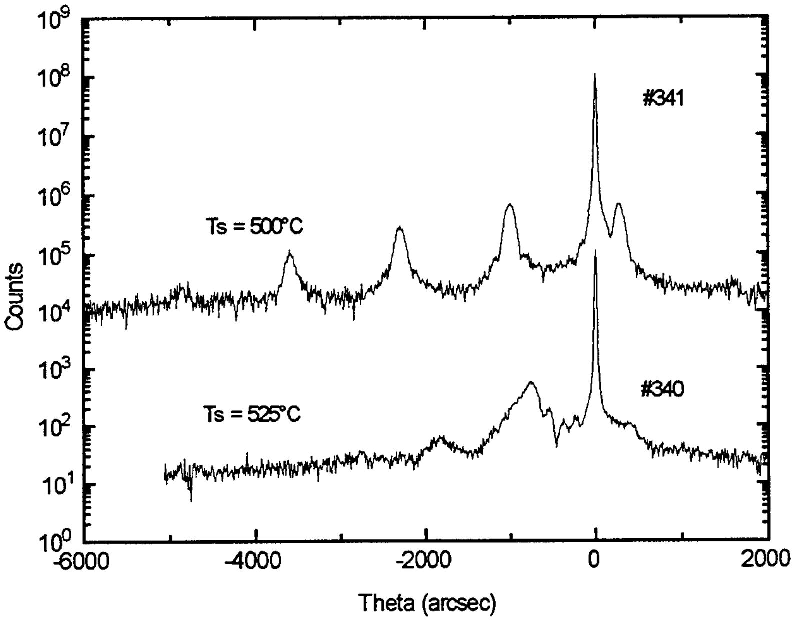

Fig. 6.4 X-ray rocking curves for InGaAs/GaAs MQWs grown at 500 and 525°C.

6.2 Laser-modified CBE of InGaAs/GaAs MQWs

Fig. 6.5 shows double-crystal XRCs and simulations based on the dynamical theory for a 10-period InGaAs/GaAs MQW structure grown at 500°C. Curves (a) and (c) are the XRCs of the InGaAs/GaAs MQWs with and without laser irradiation on the InGaAs wells, respectively, while curves (b) and (d) are the corresponding simulation results. We can clearly see that the separation between the satellite peaks is much smaller in curve (a) than that in curve (c), indicating a larger period with laser irradiation. By fitting the superlattice satellite peak positions and the relative intensities, the InGaAs well composition, well thickness, and the GaAs barrier thickness were deduced. These values are used in the envelope-function model (strain included) to calculate the exciton energy of the MQW structure, which agrees with the PL peak very well.

Fig. 6.6a shows the indium composition in the quantum wells as a function of substrate temperature with and without laser irradiation. The indium composition decreases monotonically as the substrate temperature increases without laser irradiation, whereas with laser irradiation, the indium composition does not change much with the substrate temperature. For all the samples, the indium composition with laser irradiation is lower than that without laser irradiation. Fig. 6.6b shows the InGaAs well thickness as a function of substrate temperature. The well thickness for both irradiated and non-irradiated samples has a maximum at 480°C. For all the samples, the well thickness with laser irradiation is much larger than that without laser irradiation. Therefore, we conclude that laser irradiation decreases the indium concentration in the InGaAs well while increasing the InGaAs growth rate. Based on the model proposed by Houghton *et al.*[6.4, 6.5], the number of stable periods (or the maximum stable MQW thickness) as a function of the strain in the quantum wells can be calculated for the $In_xGa_{1-x}As/GaAs$ ($x=0.13-0.25$) MQW structure. From calculation, we found that all the 10-period InGaAs/GaAs samples with the indium composition and well thicknesses as determined in Fig. 6.6 are still within

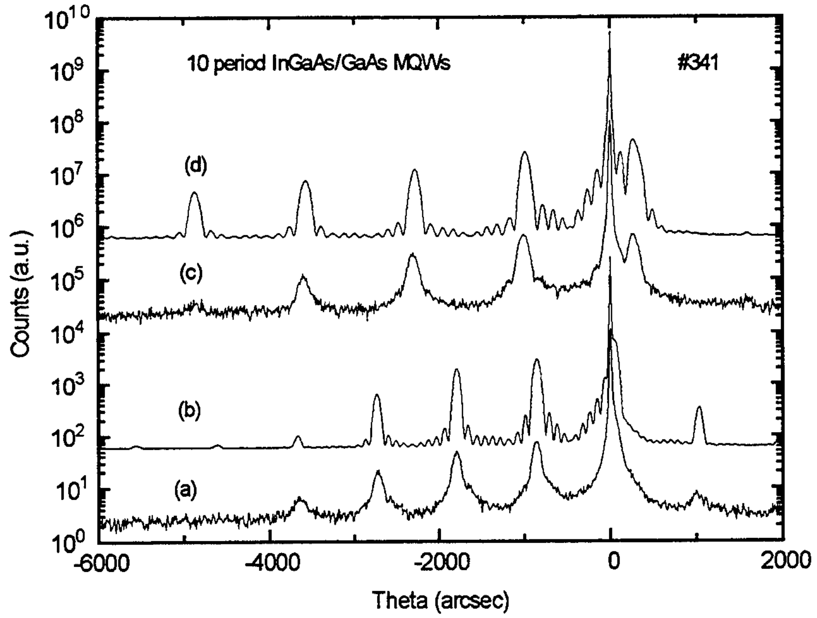

Fig. 6.5 X-ray rocking curves (a and c) and simulations (b and d) based on the dynamical theory for a 10-period InGaAs/GaAs MQW structure grown at 500°C with (a and d) and without (c and d) laser irradiation.

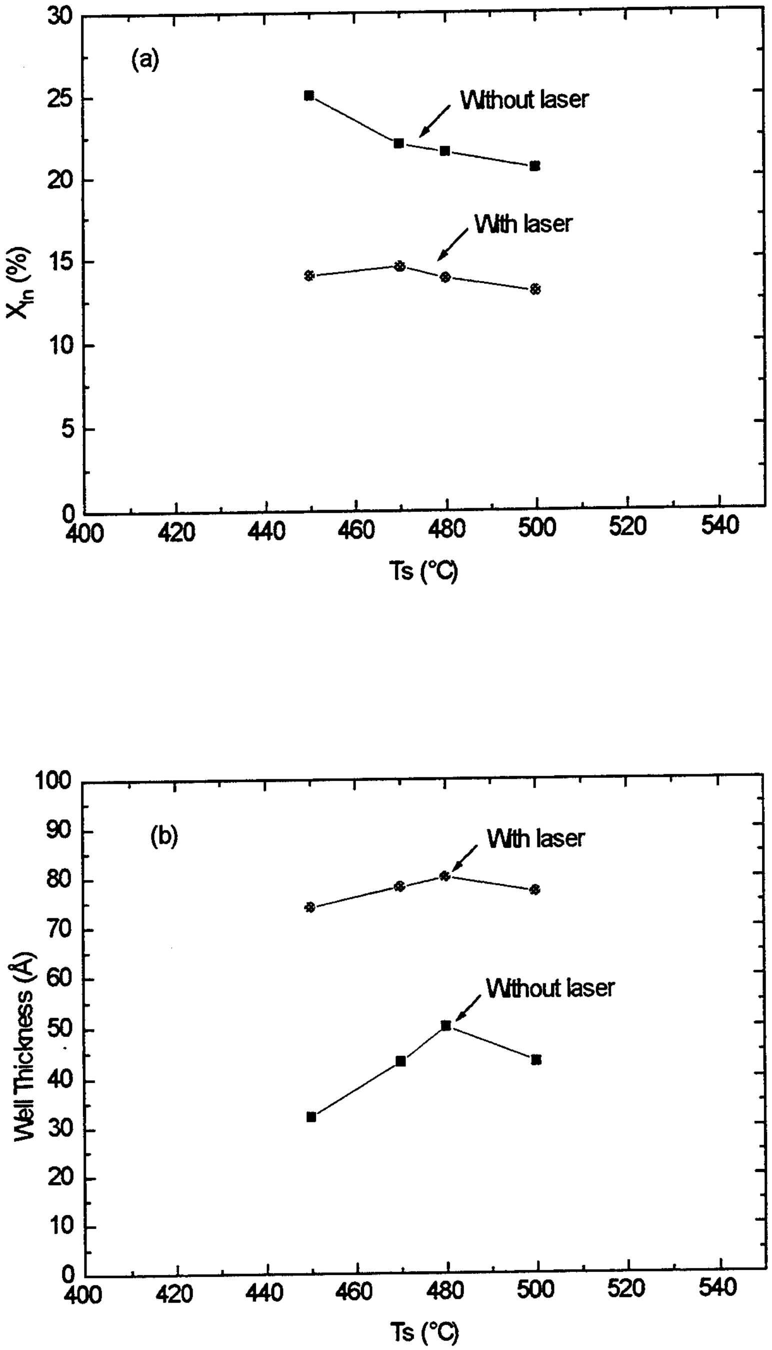

Fig. 6.6 (a) In composition, and (b) InGaAs well thickness as a function of substrate temperature with and without laser irradiation.

the stable limit. This tells us that the pseudomorphic condition was maintained for all the MQW structures.

To determine why there is a lateral variation of indium composition and InGaAs well thickness, we plot the GaAs growth rate (with the same TEGa flow rate as that used in MQW growth) as a function of substrate temperature with and without laser irradiation[6.7] in Fig. 6.7. The GaAs growth rate increases as the substrate temperature increases, and is saturated above 500°C, indicating a complete decomposition of TEGa. Since the complete decomposition of TMIn happens below 440°C, the incomplete decomposition of TEGa in the low substrate temperature range results in a high indium composition and low InGaAs growth rate, as shown in Fig. 6.6. When the substrate temperature is lower than 500°C, the GaAs growth rate is enhanced with laser irradiation due to the laser-enhanced decomposition of TEGa molecules, as seen in the figure. Moreover, the GaAs growth rate is also a function of the V/III incorporation ratio, as was shown in Fig. 5.4. As the V/III ratio increases, the growth rate decreases, indicating a site-blocking effect from big TDMAAs molecules. As we have observed enhanced arsenic desorption by laser irradiation in our MOMBE study[6.8], laser irradiation in CBE is expected to enhance the TDMAAs (or its decomposed species) desorption from the surface. From the RHEED study on CBE growth of GaAs[6.9] and InAs[6.10] using TEGa and TMIn, the growth rate almost does not change in the temperature region of 440-500°C, indicating a small change of TEGa and TMIn desorption behavior. Since laser irradiation only introduces a temperature rise of about 20°C, the influence of laser irradiation on the desorption of TMIn and TEGa is very small in the substrate temperature range studied. A higher GaAs growth rate will be expected because laser-enhanced desorption of TDMAAs will lower the V/III ratio. Therefore, both the enhanced decomposition of TEGa and the enhanced desorption of TDMAAs caused by laser irradiation will increase the GaAs growth rate. This, in turn, will result in a lower indium composition in the quantum well and a larger InGaAs well thickness.

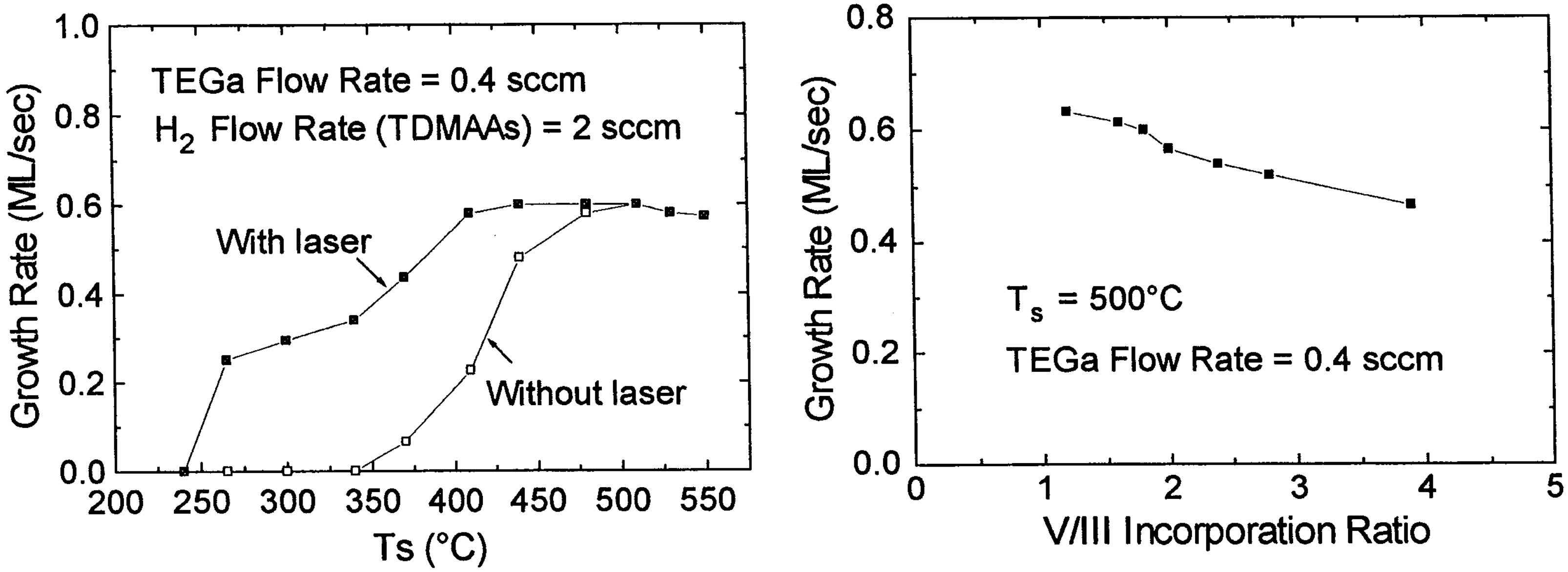

Fig. 6.7 GaAs growth rate as a function of (a) substrate temperature with and without laser irradiation, (b) V/III incorporation ratio.

Next we explore the effects of laser power density on InGaAs/GaAs MQWs. Figs. 6.8a and 6.8b show the indium composition in the quantum wells and the InGaAs well thickness as a function of laser power density at a substrate temperature of 500°C with and without laser irradiation. As we can see, the indium composition decreases while the InGaAs well thickness increases monotonically as the laser power density increases from 0 to 400 W/cm^2. Therefore, we can tune the indium composition and well thickness to desired values in selected areas by changing the laser power density. Since the enhanced GaAs growth rate increases as the laser power density increases as discussed in Chapter 5, higher laser power density will result in lower indium composition and larger InGaAs well thickness. Since the enhancement of the GaAs growth is greater at low laser power densities and the enhanced GaAs growth rate tends to saturate at high power densities, the change in the indium composition and InGaAs well thickness is more significant at low power densities.

Lateral variation of PL exciton peaks was also observed in the laser-irradiated samples, as illustrated by the blue shift (115Å) of PL peaks in Fig. 6.9a. The integrated peak intensity in the irradiated sample is about 5 times that in the non-irradiated sample. Fig 6.9b is a plot of the full width at half maximum (FWHM) of PL peaks as a function of substrate temperature for MQWs with and without laser irradiation. As we noticed, the FWHM decreases as the substrate temperature increases for both laser-irradiated and non-irradiated cases. This is due to a better crystal quality at higher growth temperature. The smallest FWHM for laser-irradiated and nonirradiated samples is 4.7 and 6.5 meV, respectively. Furthermore, laser-irradiated samples show lower FWHM than the non-irradiated samples, because wider well and lower indium concentration generally give smaller FWHM. The beneficial effects of laser irradiation on the optical properties of InGaAs/GaAs MQWs indicate potential novel-device applications, such as a multiple-wavelength laser from a single wafer.

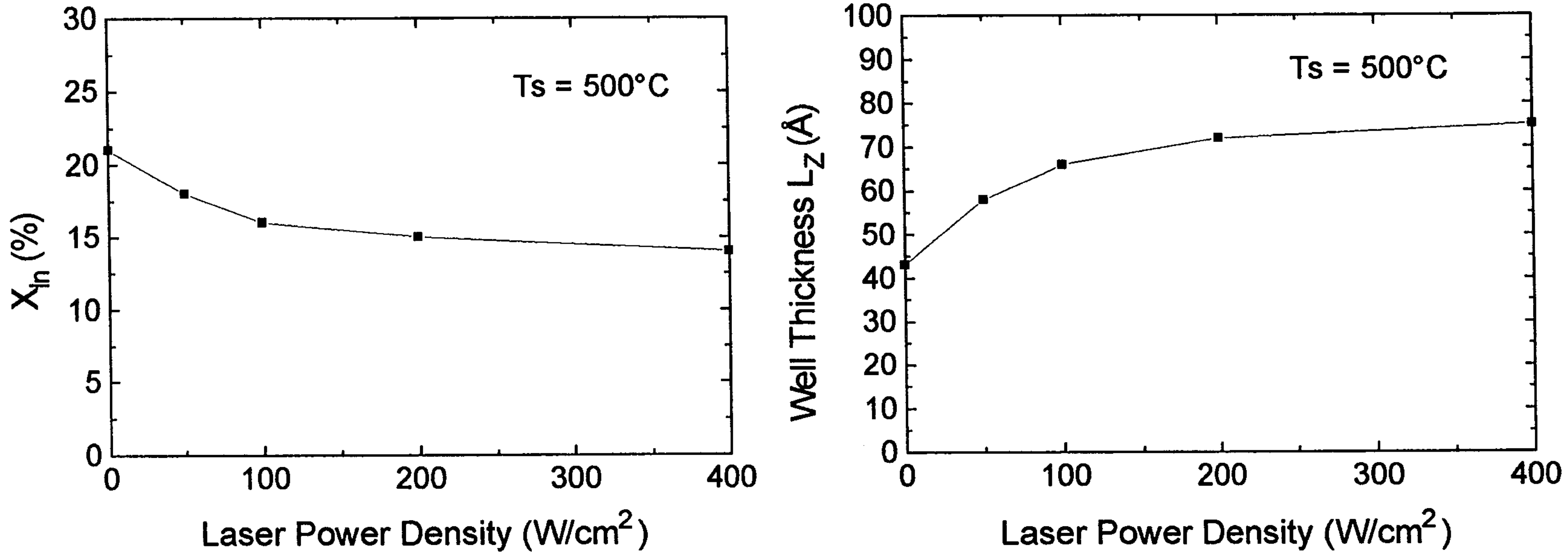

Fig. 6.8 (a) Indium composition, and (b) InGaAs well thickness as a function of laser power density with and without laser irradiation.

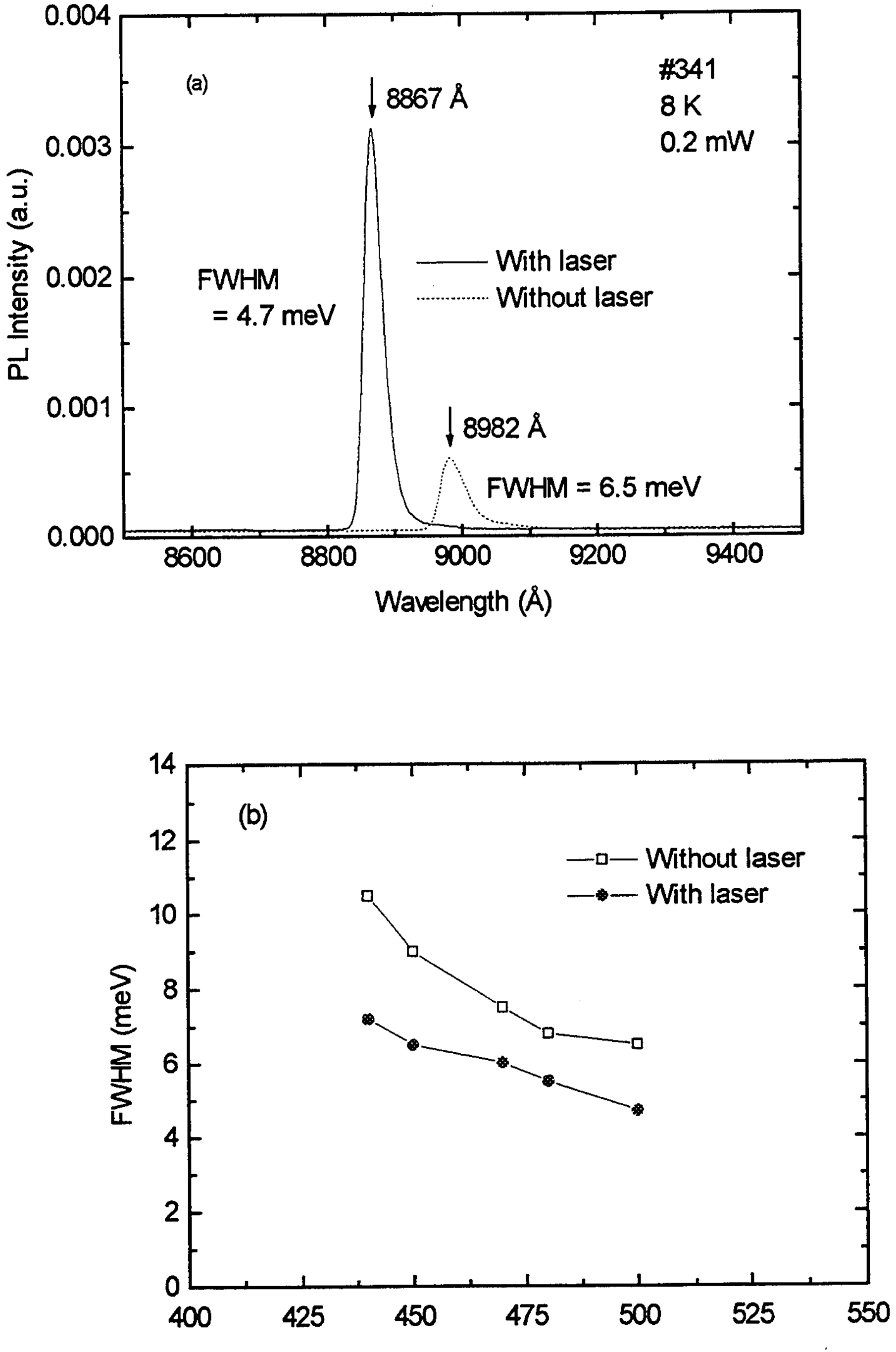

Fig. 6.9 (a) Low-temperature PL spectra of InGaAs/GaAs MQWs grown at a substrate temperature of 500°C, and (b) FWHM of PL exciton peaks as a function of substrate temperature.

6.3 References

6.1 K. Matsumura, D. Inoue, H. Nakano, M. Sawada, Y. Harada and T. Nakakado, Japan. J. Appl. Phys. *68*, L166 (1991).

6.2 N. Chand, E. E. Becker, J. P. van der Ziel, S. N. G. Chu and N. K. Dutta, Appl. Phys. Lett. *58*, 1704 (1991).

6.3 H. K. Dong, N. Y. Li, and C. W. Tu, to be published in J. Electron. Mater. (1995).

6.4 D. C. Houghton, J. Appl. Phys. *70*, 2136 (1991).

6.5 D. C. Houghton, M. Davies, and M. Dion, Appl. Phys. Lett. *64*, 505(1994).

6.6 H. K. Dong, S. C. H. Hung, and C. W. Tu, to be published in J. Electron. Mater. (1995).

6.7 H. K. Dong, N. Y. Li, W. S. Wong, and C. W. Tu, submitted to Appl. Phys. Lett. (1995).

6.8 H. K. Dong, B. W. Liang, M. C. Ho, S. Hung and C. W. Tu, J. Crystal Growth *124*, 181 (1992).

6.9 T. H. Chiu, Mater. Res. Soc. Symp. Proc. *145*, 47 (1989).

6.10 B. W. Liang, L. Y. Wang, and C. W. Tu, Proc. State-of-the-Art Prog. on Comp. Semicond. *12*, 107 (1990).

7. Laser-Enhanced Doping and Etching with Novel Gas Sources

7.1 Carbon Doping by a Novel Dopant Precursor CI_2H_2

Due to its much lower diffusivity and extremely high substitutional concentration in GaAs based compound semiconductors, carbon has been shown to be an attractive p-type dopant to replace the commonly used beryllium or zinc[7.1] for heterojunction bipolar transistors (HBTs) and nonalloyed ohmic contacts in devices[7.2-4]. Initially, Malik *et al.*[7.5] used a graphite filament to dope GaAs epitaxial layers by conventional solid-source MBE. The highest hole concentration of GaAs:C layers obtainable is $5x10^{19}$ cm^{-3}, and the minority carrier life time is extremely low. Konagai *et al.*[7.6] reported that a free carrier concentration in excess of $1x10^{20}$ cm^{-3} can be achieved in MOMBE using As_4 and TMGa as a carbon source, and Abernathy *et al.*[7.7] demonstrated HBTs using TDMAAs and TMGa for the GaAs:C base. However, using TMGa has problems of memory effect and a dependence of growth rate on doping concentration, making it difficult to control the doping profile precisely. Therefore, an extrinsic and efficient carbon doping source for direct control of doping level is very desirable.

Recently, de Lyon *et al.*[7.8, 7.9] reported the use of halomethanes, such as carbon tetrachloride (CCl_4) and carbon tetrabromide (CBr_4), as carbon-doping sources in gas-source MBE (GSMBE). The ratio of the doping efficiencies of CBr_4 to CCl_4 at a growth temperature of 600°C is reported to be 150 to 1. The higher efficiency of CBr_4 is due to the bond strength between C and Br (66 Kcal/mol) being weaker than that between C and Cl (78 Kcal/mol)[7.9, 7.10]. Consequently, direct injection of CBr_4 without a carrier gas has gained popularity in doping GaAs and InGaAs grown by MBE, GSMBE, or CBE[7.11-14]. However, because Cl_2 and Br_2 etch GaAs and possibly filaments in the growth chamber, the long-term use of CCl_4 and CBr_4 could be a concern. Therefore, a less corrosive alternative carbon precursor is desirable. We have reported carbon tetraiodide (CI_4)[7.12] as a carbon-doping source in GSMBE, but despite its weaker bond strength between C and I (50 Kcal/mol), its lower vapor pressure (1.5 Torr at 135°C) limits the hole concentration to only about $2x10^{18}$ cm^{-3}. Here, we evaluate the use of a safer carbon-doping precursor, diiodomethane (CI_2H_2) in MBE, MOMBE, and CBE because of its comparable vapor pressure to CBr_4 and its weaker average bond strength (72 Kcal/mol)[7.10] than that of CCl_4. The effect of Ar ion laser irradiation on carbon incorporation in GaAs is also investigated, and selective-area doping modification is achieved.

7.1.1 Carbon doping in GaAs by MBE, MOMBE, and CBE

The carbon doping experiments were performed in MBE using solid Ga and As_4 (at 580°C), MOMBE using TEGa and As_4 (at 510°C), and CBE using TEGa and cracked (at 510 and 540°C) or uncracked TDMAAs (at substrate temperatures from 460 to 530°C). During growth, the TEGa and H_2 (for TDMAAs) flow rates were kept at 0.4 and 2 sccm, respectively. High purity (99.999%) CI_2H_2) without a carrier gas was delivered into the growth chamber through an ultrahigh vacuum variable leak valve, as shown in Fig. 7.1. The vapor pressure of CI_2H_2 upstream to the leak valve was controlled by a Baratron pressure sensor, and the CI_2H_2 flux was adjusted using the leak valve. The CI_2H_2 injector was kept at 50°C to prevent condensation. The typical growth rate and V/III incorporation ratio of GaAs:C samples were 1μm/hr and 1.6 for MBE and MOMBE, whereas those of CBE were 0.3-0.75 μm/hr and 1.6-4.3. The films were characterized by the Van der Pauw Hall Measurement, and double crystal X-ray rocking curves.

Fig. 7.2a shows that for a fixed leak valve setting, the hole concentration of carbon-doped GaAs layer grown by MBE is a linear function of the upstream CI_2H_2 vapor pressure. Fig. 7.2b shows that for a fixed CI_2H_2 upstream pressure, the hole concentration also behaves linearly as the opening of the leak valve. A hole concentration of $9.1x10^{19}$ cm^{-3} in GaAs is achieved when the vapor pressure of CI_2H_2 is kept at 1 Torr and the leak

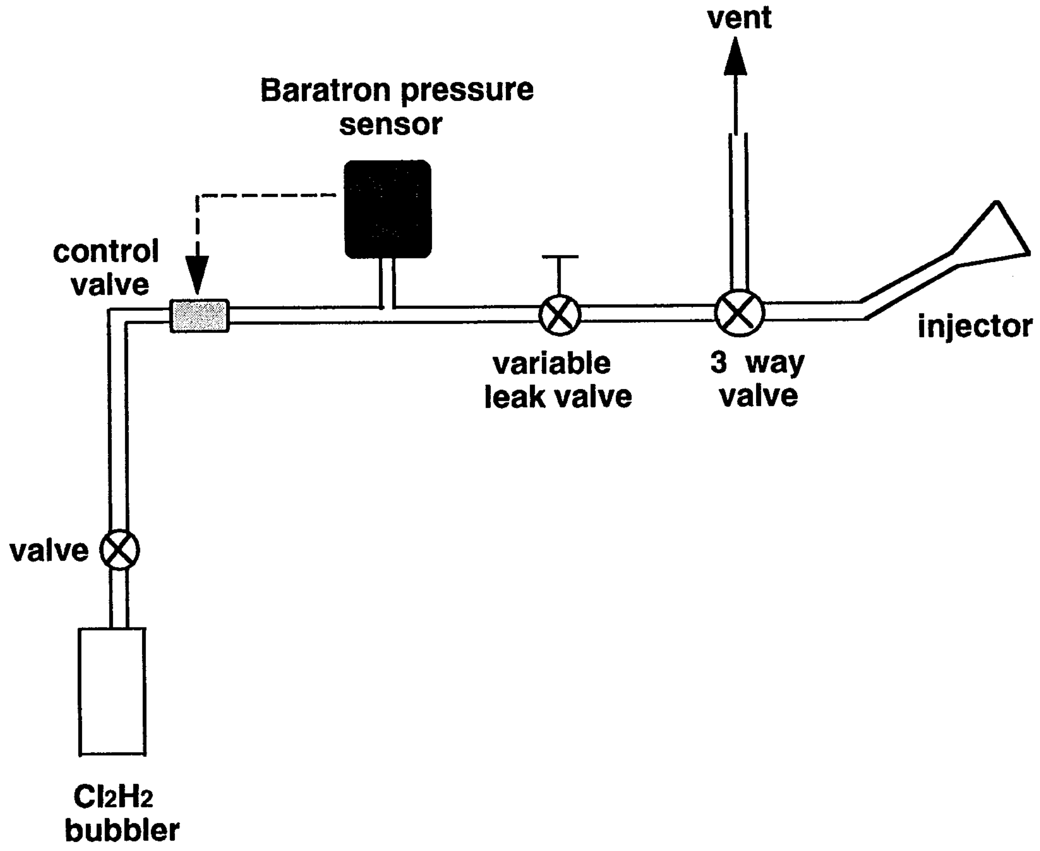
vent
Baratron pressure sensor
control valve
variable leak valve
3 way valve
injector
valve
Cl2H2 bubbler

Fig. 7.1 A schematic of the Cl_2H_2 doping line.

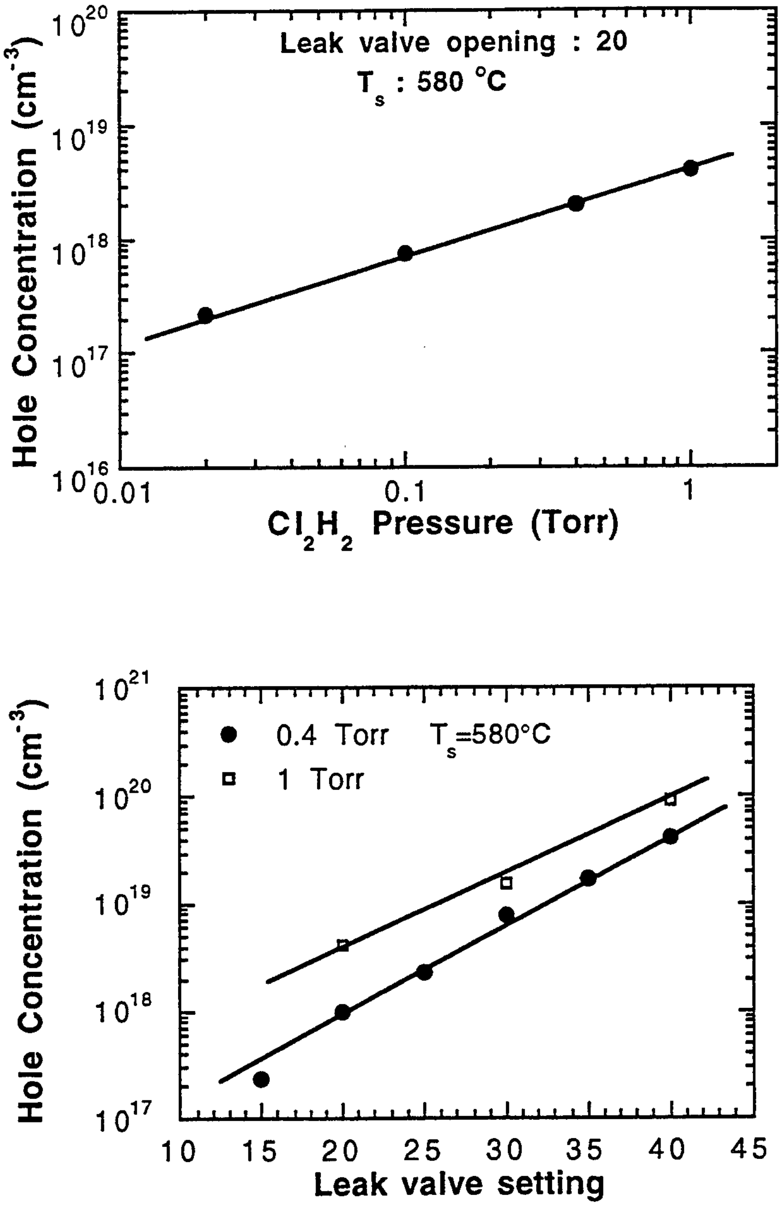

Fig. 7.2 Hole concentration of GaAs as a function of (a) the upstream Cl_2H_2 vapor pressure, and (b) the leak valve.

valve setting is at 40. We did not try to increase the doping concentration further. All of the carbon-doped GaAs samples exhibit a specular surface morphology.

To understand the electrical activation of carbon atoms in GaAs layers, we estimate the number of carbon atoms incorporated into GaAs films by using double-crystal X-ray diffracometer. As reported previously, lattice contraction is observed in highly carbon-doped GaAs due to the smaller covalent radius of carbon[7.15]. Fig. 7.3 shows a typical (400) X-ray rocking curves of a heavily carbon-doped GaAs film with the thickness of 0.5 μm and a hole concentration of 8.8×10^{19} cm^{-3}. Pendellösung fringes are clearly observed, indicating a good structural quality of the film. If we assume that all carbon atoms are substitutional and occupy only arsenic sites[7.16], and that the lattice constant follows Vegard's law, we obtain an upper limit on the number of carbon atoms, C_{As}, from the perpendicular lattice contraction, $\Delta a_\perp$, measured from a (400) rocking curve[7.15]:

$$C_{As} = 2.3256\times10^{22}\Delta a_\perp \ \ cm^{-3}$$

For the samples grown in the low 10^{19} cm^{-3} range, almost all the carbon atoms are electrically activated; and at least 91% is activated at a concentration 9.1×10^{19} cm^{-3}.

The hole concentration in GaAs layers follows the trend MBE>MOMBE>CBE for the same CI_2H_2 leak valve setting, as shown in Fig. 7.4. Site-blocking effects from the large organometallic molecules may result in a lower carbon level in MOMBE and CBE than that in MBE.

In CBE, with uncracked TDMAAs, the carbon concentration is much lower than that in MBE or MOMBE. The highest hole concentration is only 5×10^{18} cm^{-3} for Ts = 460°C, whereas it is 9×10^{19} cm^{-3} in MBE and 4×10^{19} cm^{-3} in MOMBE. Again, this result is consistent with the β-hydride elimination process of TDMAAs on the GaAs surface as we have discussed in Chapter 5. When TDMAAs is cracked, carbon incorporation efficiency is increased significantly because the β-hydride elimination reaction is suppressed in this case. The highest hole concentration achieved with cracked TDMAAs is 6.6×10^{19} cm^{-3} with a hole mobility of 61 cm^2/V s.

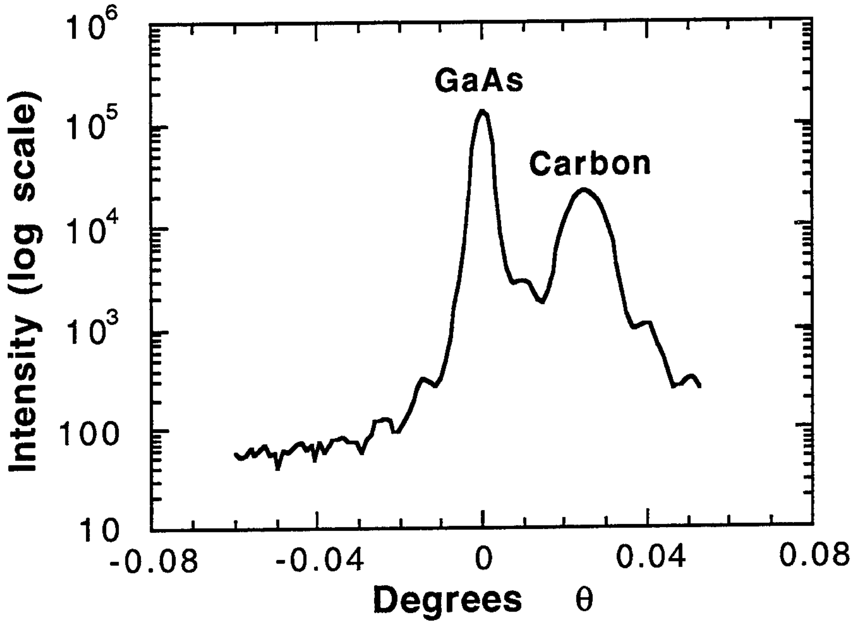

Fig. 7.3 Typical (400) X-ray rocking curve of a highly carbon-doped\ GaAs film with the thickness of 0.5 μm and a hole concentration of 8.8×10^{19} cm^{-3}.

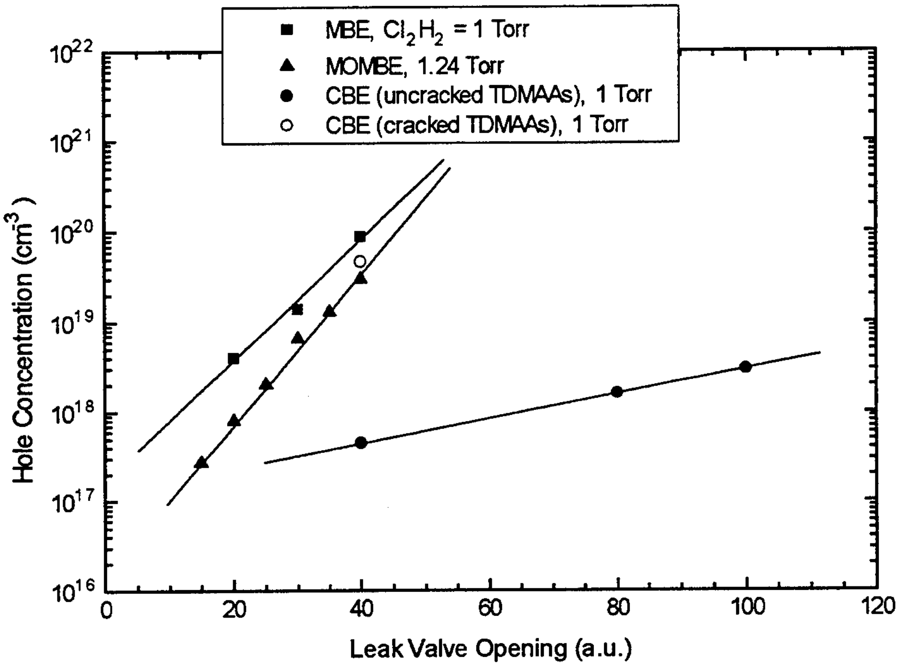

Fig. 7.4 Hole concentration of carbon-doped GaAs samples grown by MBE, MOMBE, and CBE as a function of the leak valve setting.

The room-temperature Hall mobility as a function of hole concentration for as-grown GaAs layers grown by MBE, MOMBE, and CBE using CI_2H_2 as a doping source is shown in Fig. 7.5. The MBE and MOMBE data follow the Hilsum formula, but the CBE data deviate from it when the hole concentration is below $1x10^{19}$ cm^{-3}, indicating a compensation. This compensation effect is still not clear, and further investigation is needed.

Since CI_2H_2 contains hydrogen and we also use hydrogen as a carrier gas for TDMAAs in CBE growth, we investigated possible hydrogenation effect by annealing MBE samples at 600°C (20°C above the growth temperature) and MOMBE and CBE samples at 550°C (40 and 10°C above the growth temperature, respectively) for 5 minutes in forming gas. We conclude that post-growth anneal of GaAs:C samples has no effect on the hole concentration in all samples, indicating no hydrogen passivation effect using CI_2H_2. The memory effect using CI_2H_2 was also investigated. Since we have used metalorganics sources as well as solid sources, the results are not conclusive.

7.1.2 Laser-enhanced carbon doping

For the laser-modified carbon doping study, we varied the substrate temperature from 460 to 530°C while keeping the TEGa and H_2 (for TDMAAs) flow rates at 0.4 and 2 sccm, respectively. The vapor pressure of CI_2H_2 upstream to the leak valve was kept at 1 Torr. The laser power density was set at 600 W/cm^2, and the mirror scan rate was about 50 Hz. All of the carbon-doped GaAs samples exhibit specular surface morphology. Fig. 7.6a shows the hole concentration, determined from Hall measurements, as a function of substrate temperature. As we can see, when the substrate temperature increases from 460 to 530°C, the hole concentration in the laser-irradiated area increases monotonically up to $9x10^{19}$ cm^{-3} while that in the non-irradiated area decreases monotonically from $5x10^{18}$ to $6x10^{17}$ cm^{-3}. We see that the carbon incorporation into GaAs with laser irradiation is much higher (as high as two orders of magnitude) than that without laser irradiation. The

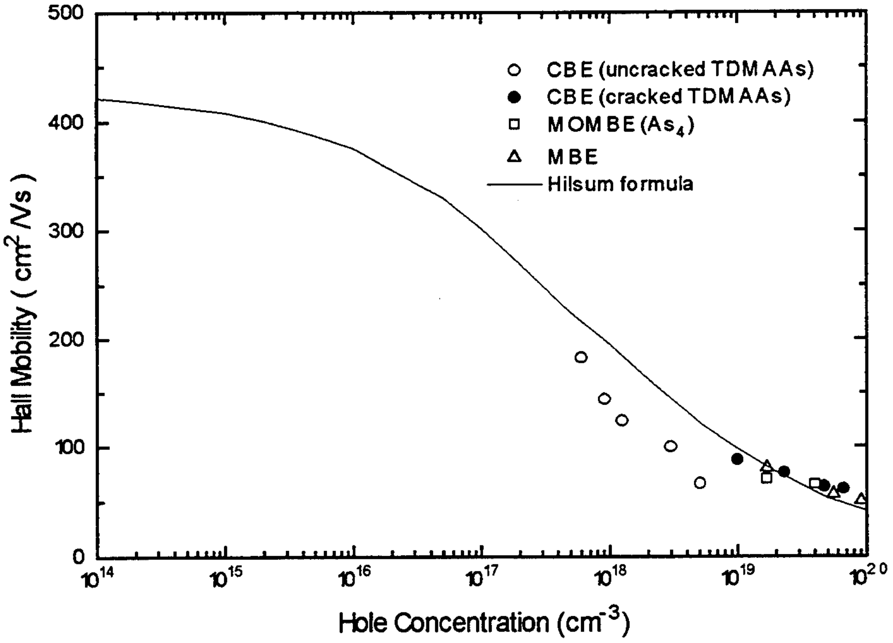

Fig. 7.5 The room-temperature hole mobility as a function of hole concentration for as-grown GaAs samples. The solid line is the Hilsum Curve.

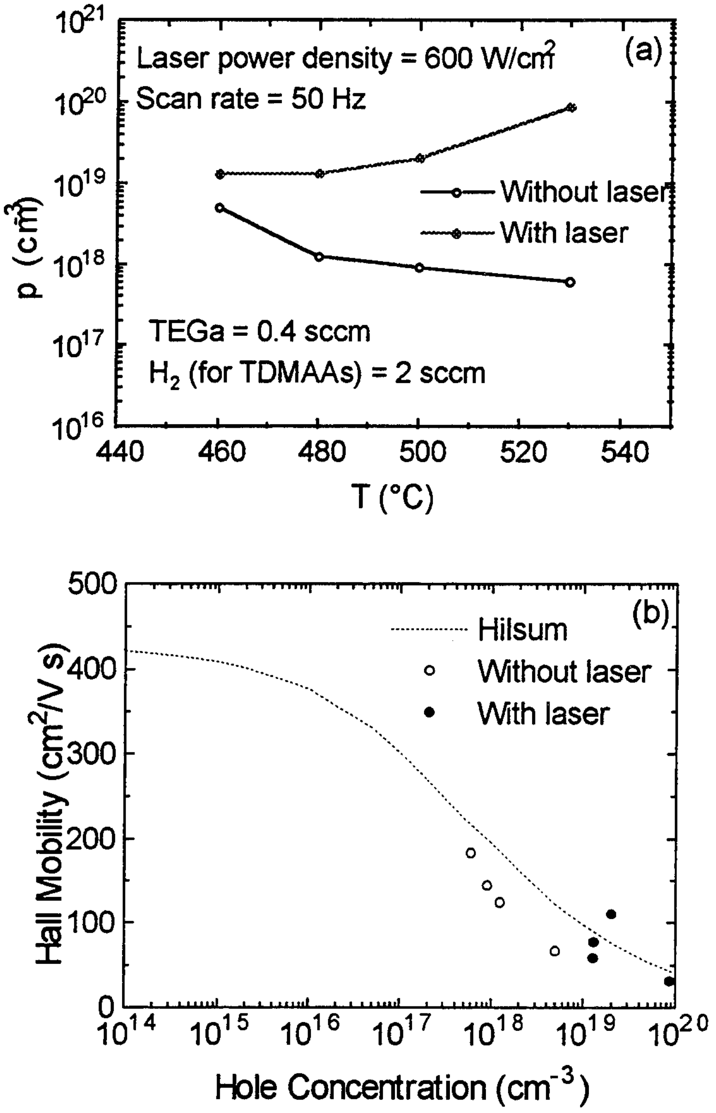

Fig. 7.6 (a) Hole concentration as a function of the substrate temperature, and (b) room-temperature Hall mobility as a function of hole concentration for carbon-doped GaAs samples with and without laser irradiation.

carbon doping study in the last section has shown that the carbon incorporation is about two orders of magnitude lower in CBE (with TEGa and uncracked TDMAAs) than that in MBE (with solid Ga and As_4), MOMBE (with TEGa and As_4), or CBE (with TEGa and cracked TDMAAs) with the same CI_2H_2 settings. So far the highest hole concentration obtained in CBE with TEGa and uncracked TDMAAs is only 5×10^{18} cm^{-3}. As discussed earlier, the low carbon level in GaAs samples grown with uncracked TDMAAs is a result of atomic hydrogen released from the efficient β-hydride elimination process on the GaAs surface. The atomic hydrogen released from TDMAAs could react with cracked carbon species from CI_2H_2 and form volatile gases, e.g., methane. Therefore, the carbon incorporation is limited. As the substrate temperature increases, the surface reaction (5) is more active, and hence the carbon concentration becomes lower. However, with laser irradiation, the surface β-hydride elimination process could be suppressed because the TDMAAs molecules are already cracked by the laser irradiation, and hence the carbon incorporation is much higher. As the substrate temperature increases, more CI_2H_2 will be decomposed, resulting in higher carbon concentration. One thing we are sure is that the laser-enhanced carbon doping is definitely not due to the photothermal effect; otherwise, the carbon incorporation should be even lower because of the temperature rise caused by laser irradiation.

The room temperature Hall mobility as a function of hole concentration for carbon-doped GaAs samples with and without laser irradiation is shown in Fig. 7.6b. The highest hole concentration achieved with laser irradiation is 9×10^{19} cm^{-3} with a hole mobility of 32 cm^2/Vs in this work. Postgrowth anneal of the carbon-doped samples has no effect on the hole concentration, indicating no hydrogenation effect using CI_2H_2 as a dopant source. This selective-area carbon-doping modification by laser irradiation could lead to novel device applications in the future.

7.2 Silicon Doping by Disilane

Silicon doping in GaAs using Si_2H_6 was also investigated in CBE growth with TDMAAs. Since cracked TDMAAs introduces a higher carbon level in a GaAs epitaxial layer, as shown in Fig. 5.5, TDMAAs was not cracked in the silicon doping study. The growth temperature was varied from 460 to 550°C while the Si_2H_6 flow rate was changed from 0.6 to 3 sccm. TEGa and H_2 (for TDMAAs) flow rates were 0.4 and 2 sccm, respectively. Fig. 7.7a and 7.7b show electron concentration as a function of Si_2H_6 flow rate and substrate temperature, respectively. As we can see, the electron concentration increases linearly as the Si_2H_6 flow rate increases for both laser-irradiated and non-irradiated samples at a substrate temperature of 500°C. With laser irradiation, the electron concentration shows a slight increase at higher Si_2H_6 flow. At high substrate temperature, the electron concentration is almost the same with and without laser irradiation. However, at lower substrate temperature, laser irradiation gives higher electron concentration because of its thermal effect. Fig. 7.8 shows the room temperature Hall mobility as a function of electron concentration for Si-doped GaAs layers. Also plotted are an empirical fit to the 300 K results from Si-doped MBE-grown GaAs layers presented by Hilsum[6.18] and the computed values of electron mobility as a function of electron concentration at different compensation ratios presented by Walukiewicz *et al.*[7.19]. All the Si-doped GaAs samples show a compensation ratio of about 0.6, and the highest carrier concentration achieved is 1.3×10^{18} cm^{-3}. Since the carbon level is quite low in the undoped GaAs samples with similar growth conditions, as seen in Fig. 5.5, the high compensation ratio may come from some other mechanism and further investigation is needed.

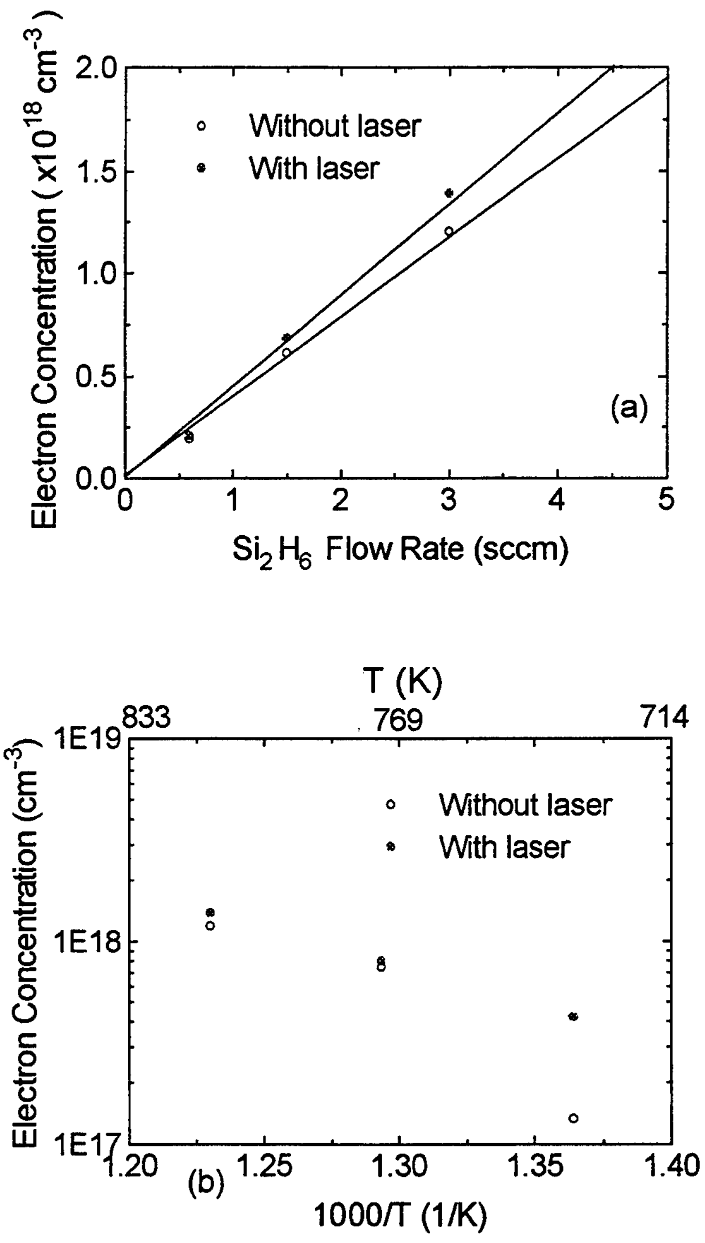

Fig. 7.7 Electron concentration as a function of (a) Si_2H_6 flow rate, and (b) substrate temperature.

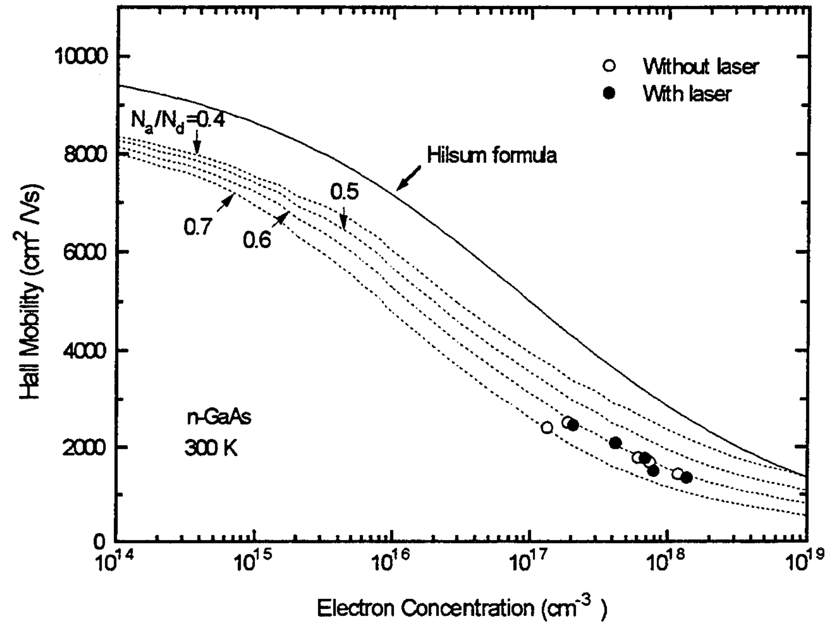

Fig. 7.8 Room-temperature Hall mobility as a function of electron concentration for silicon-doped GaAs samples with and without laser irradiation.

7.3 Laser-Enhanced *In Situ* GaAs Etching

We have already demonstrated the capability of using TDMAAs in CBE growth and doping of GaAs. Moreover, a unique feature associated with TDMAAs, i.e., *in situ* etching effect, was also explored. The GaAs oxide layer was removed at a much lower substrate temperature (Ts = 450°C) when we thermally desorb the GaAs native oxide under an uncracked TDMAAs supply, as evidenced by the RHEED pattern change. The GaAs (2x4) reconstruction pattern appears clearly at about 450°C after exposure to uncracked TDMAAs for 20 minutes. The time needed to remove the oxide layers is shorter as the substrate temperature increases, indicating a higher reaction rate at a higher substrate temperature. However, when we desorb oxide under a cracked TDMAAs supply, the change from the diffused pattern (as expected for the amorphous native oxide layers) to the (2x4) pattern cannot be achieved until the substrate temperature is close to 580°C, the normal desorption temperature under an arsenic overpressure. The dissimilar behavior between uncracked and cracked TDMAAs is due to the different surface chemical reactions with and without pre-cracking TDMAAs. Uncracked TDMAAs provides a large amount of reactive free radicals e.g., $\bullet N(CH_3)_2$, $\bullet H$, and $\bullet CH_3$, to the GaAs surface when it decomposes on the surface, and these reactive radicals could attack the oxide layer. Etching of GaAs by $\bullet H$ and $\bullet CH_3$ has been demonstrated by Kobayashi *et al.*[7.20] and Spencer *et al.*[7.21], respectively. On the other hand, by cracking TDMAAs, these free radicals could disappear through reactions (2)-(4) and reaction

$$\bullet H + \bullet CH_3 \rightarrow CH_4$$

in the gas phase before they arrive at the GaAs surface. Therefore, cracked TDMAAs will not attack the oxide layer.

In order to further explore the TDMAAs etching effect, patterned GaAs substrates masked by SiO_2 were exposed to uncracked TDMAAs alone at substrate temperatures from 500 to 650°C. A constant H_2 (for TDMAAs) flow rate (4 sccm) was maintained during the experiment. Fig. 7.9a shows an SEM picture of a SiO_2-masked GaAs patterned substrate etched by TDMAAs at 650°C. The etching effect is quite obvious, and the etch rate can be measured. From the SEM study, we also noticed that the surface morphology was rougher at higher etching temperatures, probably due to different etching rates on different surface orientations. As was observed in MBE[7.22], the GaAs (411)A micro-facets formed at substrate temperatures higher than 580°C, and the etching rate for the flat (411)A surface is only 10-50% of that for the (100) surface. As shown in Fig. 7.9b, the GaAs surface etched by TDMAAs at 550°C is much smoother compared to that etched by TDMAAs at 650°C.

Fig. 7.10 shows the GaAs etch rate with and without laser irradiation as a function of substrate temperature. The etch rate increases as the substrate temperature increases for both cases, and laser irradiation enhances the etch rate. From the fitted curves in Fig. 7.10, we find that the GaAs etch rate (with laser irradiation) at a substrate temperature T_0 is almost the same as that (without laser irradiation) at a substrate temperature T_0+35°C, where 35°C is about the temperature rise caused by an Ar ion laser irradiation at a power density of 600 W/cm^2 (calculated from a heat-flow equation and confirmed by infrared laser interferometry[7.23]). Therefore, we conclude that the photothermal effect contributes to the laser-enhanced *in situ* GaAs etching by TDMAAs. The GaAs etching activation energy obtained for the case with laser irradiation is about 15 Kcal/mol, while that obtained for the case without laser irradiation is about 16 Kcal/mol. Again, the etching effect may be caused by those reactive free radicals mentioned above. The activation energy of GaAs etching by atomic hydrogen has been deduced to be about 50 Kcal/mol[7.20], while the activation energy for etching in a $\cdot H/\cdot CH_3$ mixture environment ranges from 2.3 to 7.2 Kcal/mol[7.21]. Therefore, the etching activation energy deduced from Fig. 7.10 should be related to etching caused by the active amino species originated from the TDMAAs surface decomposition. However, more work needs to be done to

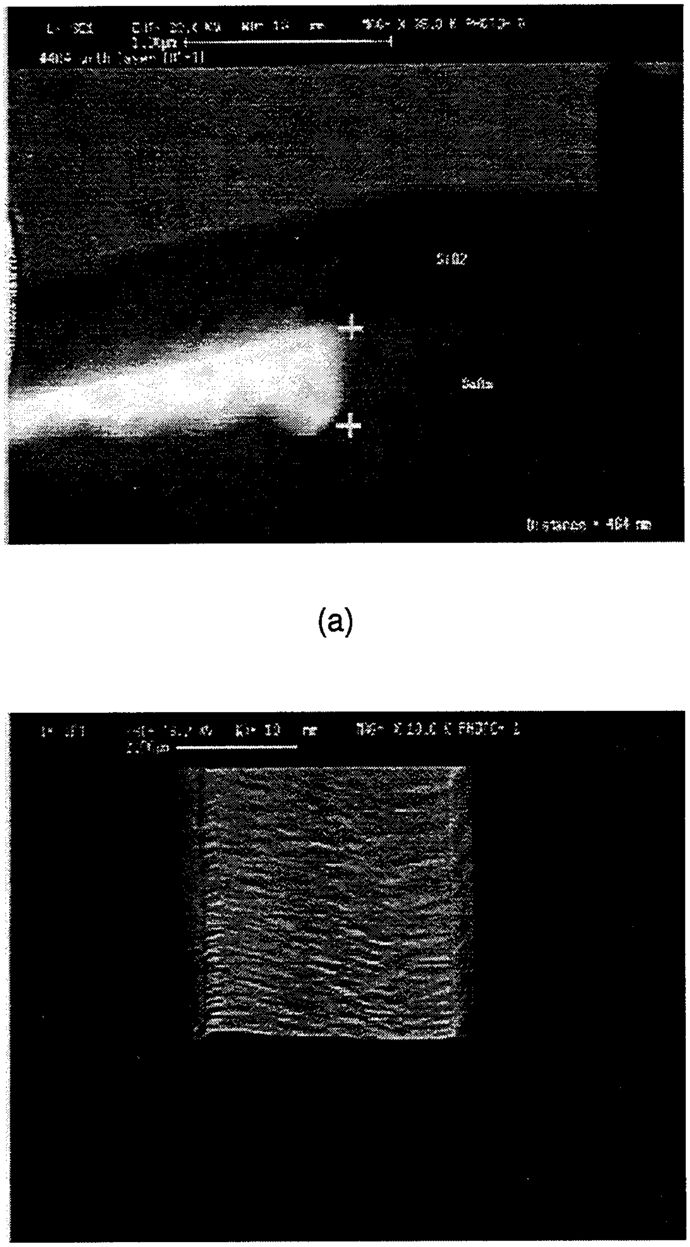
SiO2
GaAs
Distance = 464 nm

(a)

(b)

Fig. 7.9 (a) The SEM picture showing the TDMAAs etching effect at 650°C on a SiO2-masked GaAs patterned substrate. (b) The SEM picture showing the GaAs surface etched by TDMAAs at 550°C.

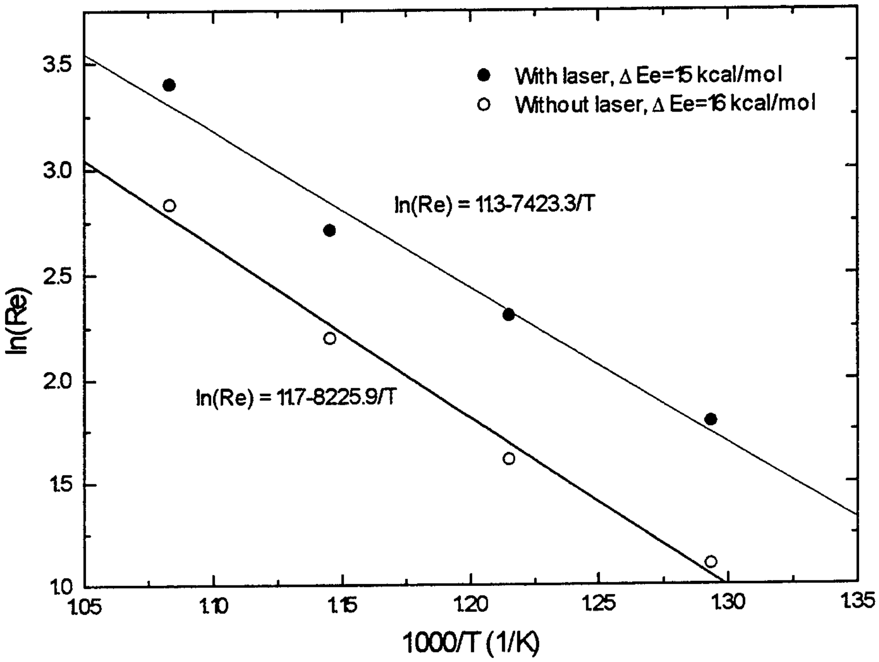

Fig. 7.10 GaAs etch rate with and without laser irradiation as a function of substrate temperature.

confirm this. The etching effect was not observed when cracked TDMAAs was used because no free amino radicals are involved in the surface reactions.

Selective-area epitaxy (SAE) is a very promising technique for the fabrication of planar, monolithic electronic and photonic integrated circuits. SAE is often used in regrowth of various devices. In order for the SAE not to affect the device quality, low growth temperature is highly desirable. Complete selective-area growth of GaAs was achieved at a substrate temperature of 420°C using TEGa and TDMAAs, which is much lower than the 600°C in the case of using TEGa and AsH_3[7.24]. The low selective growth temperature is probably caused by the catalytic decomposition of both TEGa and TDMAAs on GaAs surfaces and absence of such effects on SiO_2 masked surfaces[7.25]. The surface morphology of GaAs samples selectively grown at different conditions was investigated by SEM. Figs. 7.11a, 7.11b, and 7.11c show the surface morphology of the samples grown by uncracked TDMAAs at 420°C, 460°C, and 540°C, respectively. As we can see, the surface is quite smooth at 420°C, and becomes rougher as the temperature increases. The surface is always highly textured when the substrate temperature is higher than 500°C, as shown in Fig. 7.11c. The roughness is probably caused by the etching effect using uncracked TDMAAs. As the substrate temperature increases, the etching effect is more significant and hence the surface is rougher. Moreover, with cracked TDMAAs, a specular surface morphology can be achieved even at a substrate temperature of 540°C, as shown in Fig. 7.11d, since no etching effect is induced by cracked TDMAAs.

7.4 References

7.1 B. T. Cunningham, L. J. Guido, J. E. Baker, J. S. Major, J. N. Holonyak, and G. E. Stillman, Appl. Phys. Lett. *55*, 687 (1989).

7.2 M. Konagai, T. Yamada, T. Akatsuka, K. Saito, E. Tokumitsu, and K. Takahashi, J. Cryst. Growth *98*, 167 (1989).

7.3 P. M. Enquist, Appl. Phys. Lett. *57*, 2348 (1990).

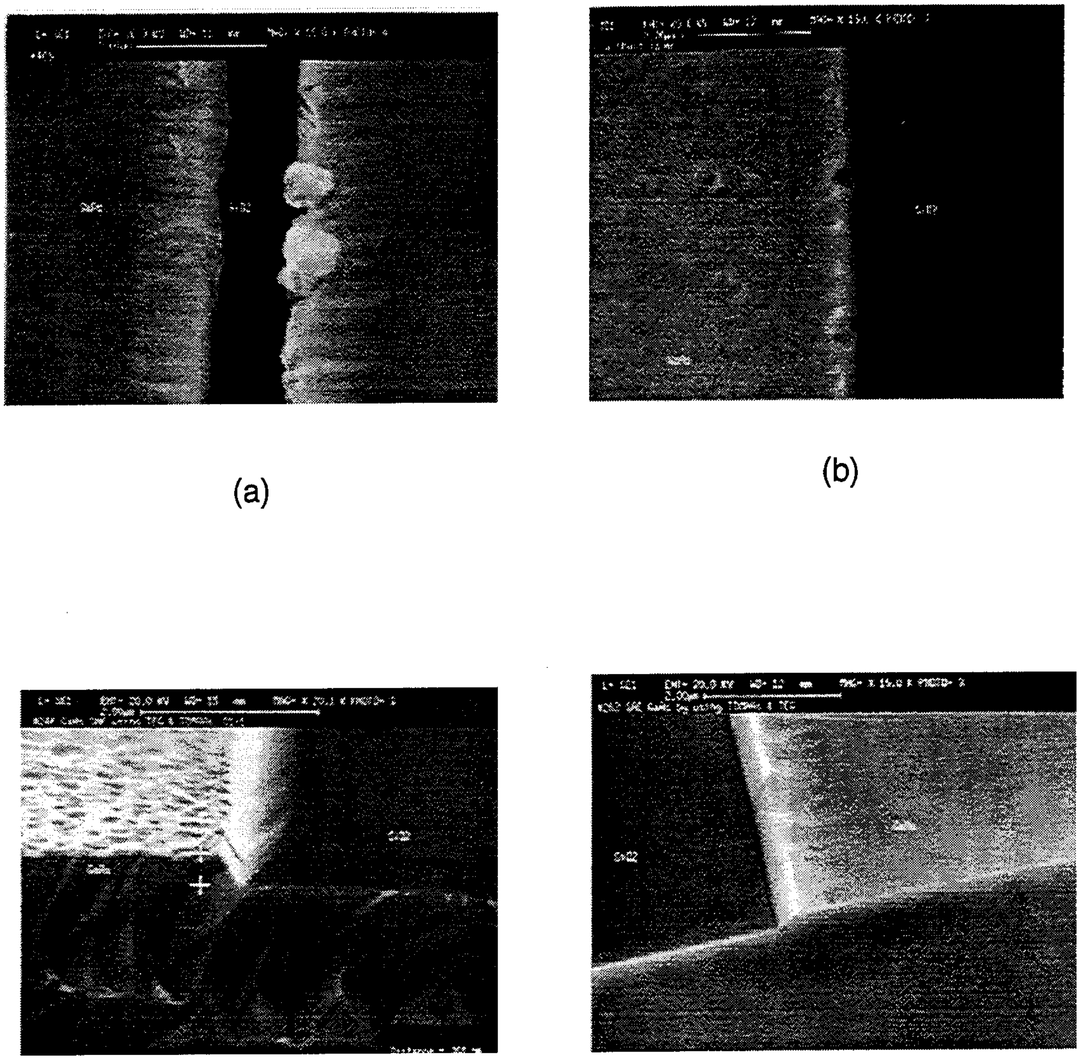

(a) (b)

(c) (d)

Fig. 7.11 SEM pictures showing the surface morphology of the samples grown by (a) uncracked TDMAAs at 420°C, (b) uncracked TDMAAs at 460°C, (c) uncracked TDMAAs at 540°C, and (d) cracked TDMAAs at 540°C.

7.4 B. T. Cunningham, G. E. Stillman, and G. S. Jackson, Appl. Phys. Lett. *56*, 361 (1990).

7.5 R. J. Malik, R. N. Nottenberg, E. F. Schuber, J. F. Walker, and R. W. Ryan, Appl. Phys. Lett. *53*, 2661 (1988).

7.6 M. Konagai, T. Yamada, T. Akatsuka, S. Nozaki, R. Miyake, K. Saito, T. Fukamachi, E. Tokumitsu, and K. Takahashi, J. Cryst. Growth 105, 359 (1990).

7.7 C. R. Abernathy, F. Ren, S. J. Pearton, T. R. Fullowan, R. K. Montgomery, P. W. Wisk, J. R. Lothian, P. R. Smith, and R. N. Nottenburg, J. Cryst. Growth *120*, 234 (1992).

7.8 T. J. de Lyon, N. I. Buchan, P. D. Kirchner, J. M. Woodal, D. T. Mcinturff, G. J. Scilla, and F. Cardone, J. Cryst. Growth *111*, 564 (1991).

7.9 T. J. de Lyon, N. I. Buchan, P. D. Kirchner, J. M. Woodal, G. J. Scilla, and F. Cardone, Appl. Phys. Lett. *58*, 517 (1991).

7.10 N. I. Buchan, T. F. Kuech, G. Scilla, and F. Cardone, J. Cryst. Growth 110, 405 (1991).

7.11 Y. M. Houng, S. D. Lester, D. E. Mars, and J. N. Miller, J. Vac. Sci. Tech. *B 11*, 915 (1993).

7.12 C. W. Tu, B. W. Liang, and T. P. Chin, J. Cryst. Growth *136*, 1991 (1994).

7.13 P. J. Lemonias, W. E. Hoke, D. G. Weir, and H. T. Hendriks, J. Vac. Sci. Tech. *B 12*, 1190 (1994).

7.14 K. Zhang, W. Y. Hwang, D. L. Miller, and L. W. Kapitan, Appl. Phys. Lett. *63*, 2399 (1993).

7.15 T. J. de Lyon, J. M. Woodal, M. S. Goorsky, and P. D. Kirchner, Appl. Phys. Lett. *56*, 1040 (1990).

7.16 I. Fujimoto, S. Nishine, T. Yamada, M. Konagai, and K. Takahashi, Jpn. J. Appl. Phys. *31*, L296 (1992).

7.17 C. R. Abernathy, D. A. Bohling, G. T. Muhr, and P. W. Wisk, Mat. Res. Soc. Symp. Proc. (1994).

7.18 C. Hilsum, Electron Lett. *10*, 259 (1974).

7.19 W. Walukiewicz, L. Lagowski, L. Jastrzebski, M. Lichtensteiger, and H. C. Gatos, J. Appl. Phys. *50*, 899 (1979).

7.20 R. Kobayashi, K. Fujii, and F. Hasegawa, Jpn. J. Appl. Phys. *30*, L1447 (1991).

7.21 J. E. Spencer, T. R. Schimert, J. H. Dinan, D. Endres, and T. R. Hayes, J. Vac. Sci. Technol. *A8*, 1690 (1990).

7.22 G. Laurence, F. Simondet, and P. Saget, Appl. Phys. *19*, 63 (1979).

7.23 S. C. H. Hung, H. K. Dong, and C. W. Tu, Mater. Res. Soc. Symp. Proc. *340*, 35 (1994).

7.24 E. Tokumitsu, Y. Kudou, M. Konagi, and K. Takahashi, Jpn. J. Appl. Phys. *24*, 1180 (1989).

7.25 T. Hidaka and I. Suemune, Jpn. J. Appl. Phys. *33*, 3500 (1994).

8. Growth of Phosphorous-Based Materials by Chemical Beam Epitaxy

8.1. Introduction

Toward the end of the contract we embarked on CBE of phosphides with alternative precursors, although phosphides were not specifically included in the contract. Due to lack of time, we did not perform laser-assisted growth. In this chapter we present preliminary results on CBE of InP and InGaP using TBP and TDMAP.

Recently, phosphorus-based materials have been studied extensively for optoelectronics device applications. PH_3 is commonly used as a group-V source in MOVPE, GSMBE, and CBE. For safety considerations, less hazardous and lower vapor pressure alternatives are highly desirable. Among these alternatives, TBP and TDMAP are two promising metalorganic sources to replace PH_3.[8.1-5] We used these two sources for growth of phosphides.

The group-III source used are solid Ga, TEGa, and TMIn. TEGa and TMIn are introduced into the growth chamber without carrier gas through vapor-source mass flow controllers, whereas TDMAP is carried by hydrogen and injected into the chamber through a leak valve. High-purity (99.999%) TBP without a carrier gas is delivered into the growth chamber through a mass flow controller. For the InGaP and InP growth, a home-made cracker is used to thermally crack TBP and TDMAP. The cracker consists of a tantalum tube and tantalum baffles to increase the cracking efficiency. A quadruple mass spectrometer is used to study the TBP and TDMAP decomposition pattern. The growth rate of the epilayers and V/III incorporation ratios were determined by group III- and group V-induced RHEED intensity oscillations. The films were characterized by Van der Pauw Hall measurement, double-crystal X-ray diffraction, PL, and SEM.

8.2 Growth of InP by CBE

Initially, TMIn and TDMAP were used as the group III and group V source, respectively, to grow undoped InP. As Abernathy *et al.*[8.1] reported earlier, we also find that InP can not be grown without thermally cracking TDMAP, due to possible indium-enhanced desorption of phosphorus species from the growing surface. As indicated in Fig. 8.1a, the intensity of the TDMAP, $P[N(CH_3)_2]_2$, and $PN(CH_3)_2$ species in the quadruple mass spectrum dramatically decreases at a cracker temperature of about 850°C. On the other hand, the intensity of P_2 increases to a maximum at 850°C, indicating that the TDMAP source can be completely decomposed at this cracker temperature. However, as shown in Fig. 8.1b, an abundance of N^+, CH_3^+ and $(CH_3)_2N^+$ species is simultaneously generated from the dissociation of amine radicals.

When the cracker temperature is at 850°C, the growth rate of InP is limited to 0.35 μm/h. Such a low growth rate of InP is due to insufficient phosphorous species supplied at this higher cracker temperature. The InP growth rate, however, can be increased to 1.1 μm/h when the cracker temperature is lowered to 750°C. Typical indium-induced RHEED intensity oscillations for InP grown at 470°C with a V/III incorporation ratio of 1.3 are shown in Fig. 8.2. Undoped InP epitaxial layers with a typical thickness of 2 μm were grown at different V/III ratios and were characterized by Van der Pauw Hall measurements. All of the unintentionally doped InP layers are n-type, and the background room-temperature electron concentration varies from $2x10^{16}$ to $4x10^{16}$ cm^{-3} with the mobility ranging from 2850 to 2600 $cm^2/V{\cdot}s$. The results indicate that undoped InP layers are compensated with a compensation ratio of 4. This compensation effect was mainly due to the C and N species generated from the dissociation of amine radicals incorporated into the epilayers.

Fig. 8.3 shows a typical PL spectrum of an unintentionally doped InP epilayer using cracked TDMAP ($T_{cracker}$=750°C). The peaks at 8800 Å (exciton recombination) and

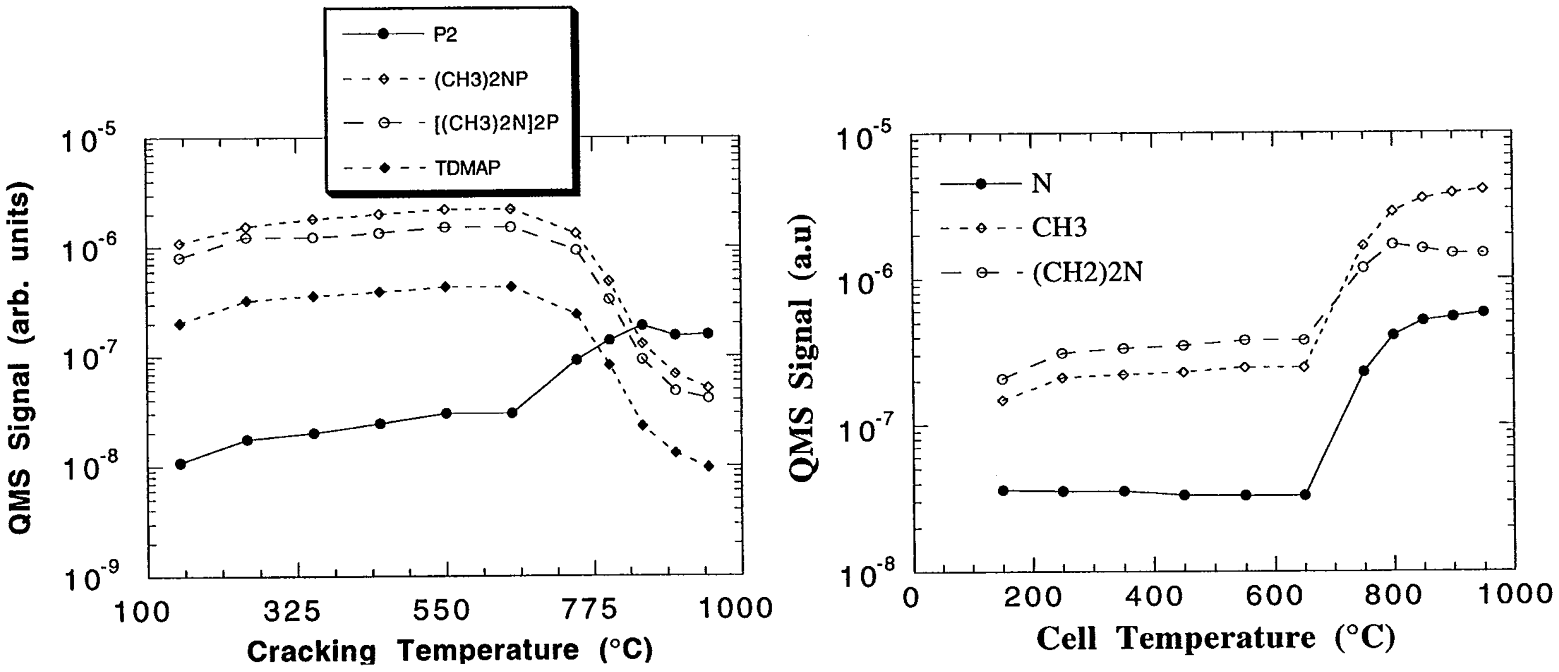

Fig. 8.1 (a) Phosphorous species, and (b) the byproducts as a function of the TDMAP cracker temperature.

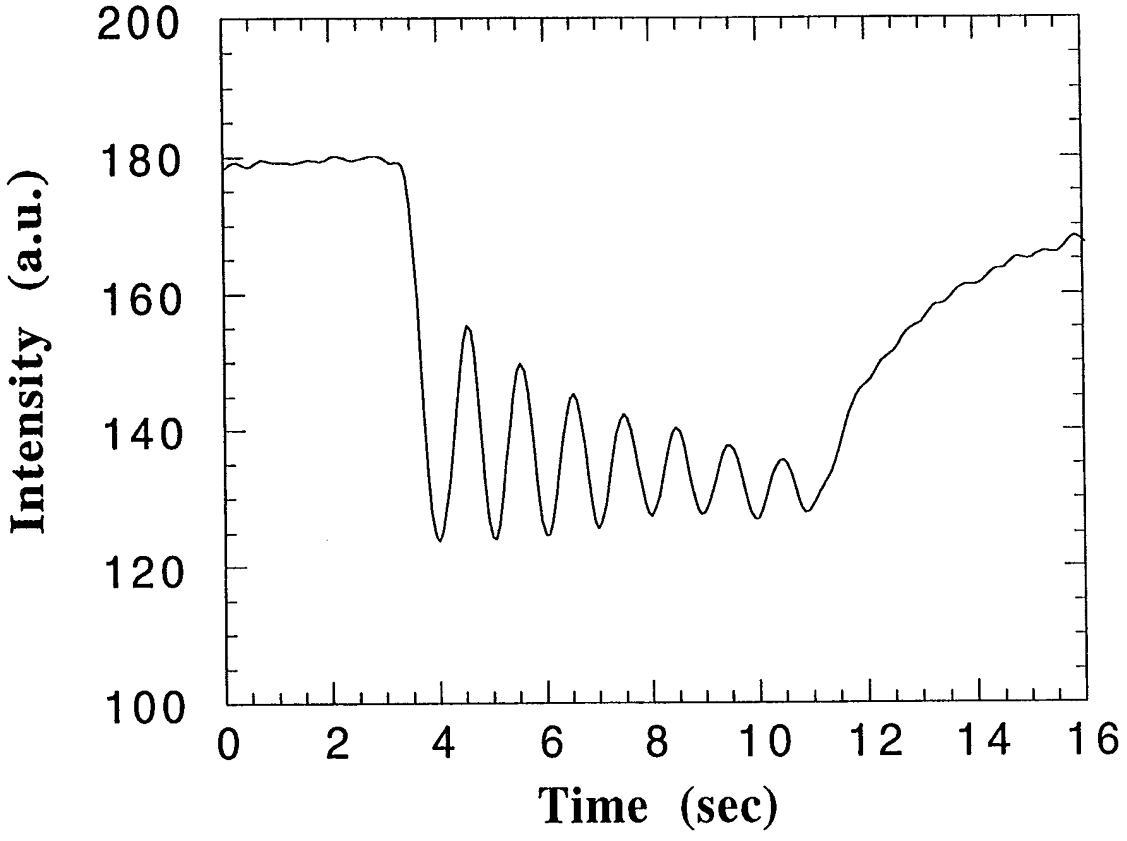

Fig. 8.2 Typical indium-induced RHEED intensity oscillations for InP grown at 470°C with a V/III incorporation ratio of 1.3.

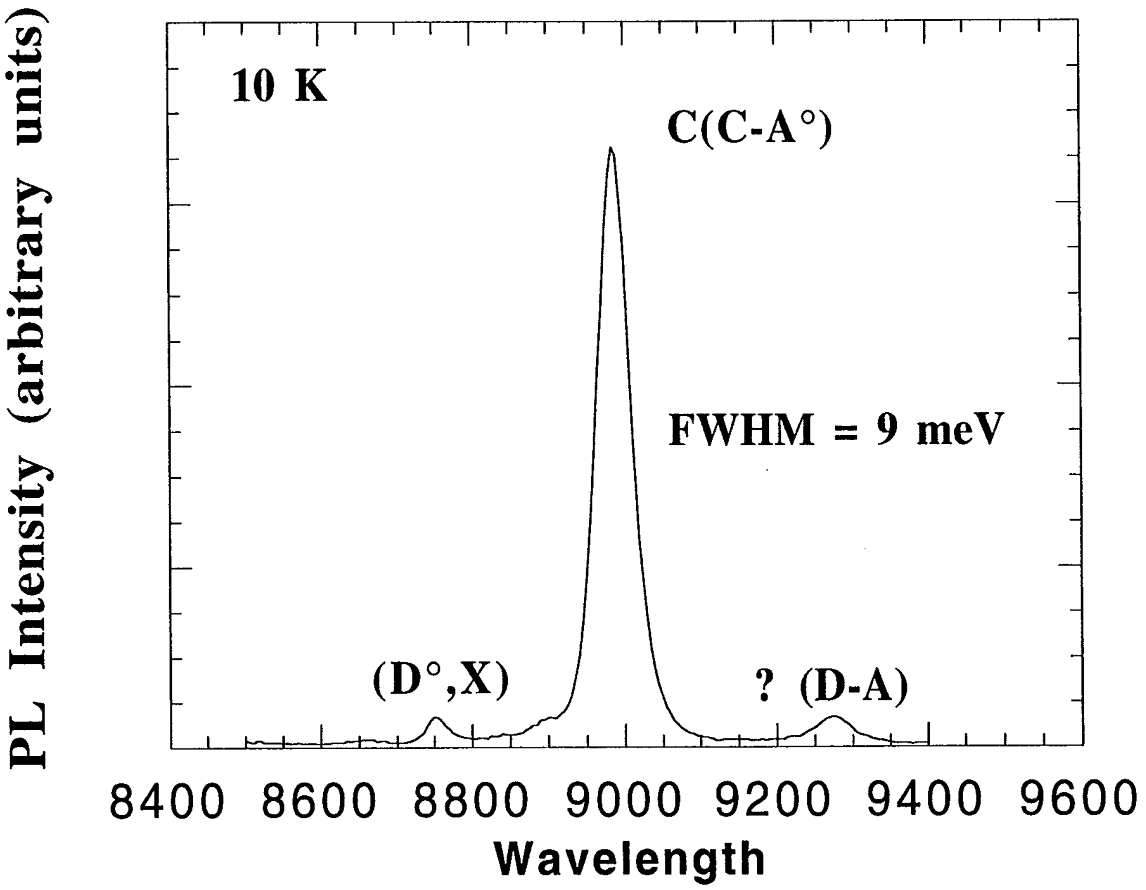

Fig. 8.3 Typical PL spectrum of an unintentionally doped InP epilayer using cracked TDMAP.

9000 Å (donor-acceptor pair) are frequently observed from undoped InP epilayer, but the peak at 9000 Å is dominant in our spectrum, indicating a high degree of compensation in the epilayer.

As for surface morphology, many hillocks are found on InP epilayers as shown in Fig. 8.4. This rough surface may be due to an etching effect from the TDMAP source. As indicated in the quadruple mass spectrum, $P[N[CH_3]_2]_x$ species are not completely decomposed at a cracking temperature of 750°C, and these residual amino species may degrade or etch the surface of InP leading to the hillock formation. To verify the possible etching effect of TDMAP, a patterned InP substrate was prepared and exposed to uncracked TDMAP flux at a substrate temperature of 570°C for 75 minutes. From the SEM photograph shown in Fig. 8.5, we see that the TDMAP source can etch the InP substrate with an etching rate of 4.5 μm/h at 570°C and the etching profile is similar to a wet chemical etch. This etching effect shows that TDMAP, similar to TDMAAs described in Chapter 7, is a promising source to develop an in situ etching technique in the CBE chamber for the regrowth of phosphide-based novel devices.

To improve the surface morphology of InP epilayers, TBP is used as the group-V precursor. Specular InP surface can be obtained at a TBP cracking temperature from 700 to 900°C. Fig. 8.6 shows the dependence of the InP growth rate on the TMIn flow rate using cracked TBP and cracked TDMAP. The growth temperature was 470°C and the group V incorporation rate was about 1.2 μm/h in both cases. For the same TMIn flow rate, we can see that the growth rate using TBP is always higher than that using TDMAP. This indicates that TDMAP could etch InP at a growth temperature of 470°C with an etching rate of about 0.2 μm/h.

Fig. 8.7 shows the InP growth rate as a function of substrate temperature. As we can see, the InP growth rate is independent of the substrate temperature from 430 to 490°C when TBP is used. When the growth temperature is below 430°C, the lower decomposition efficiency of TMIn limits the InP growth rate. When the substrate

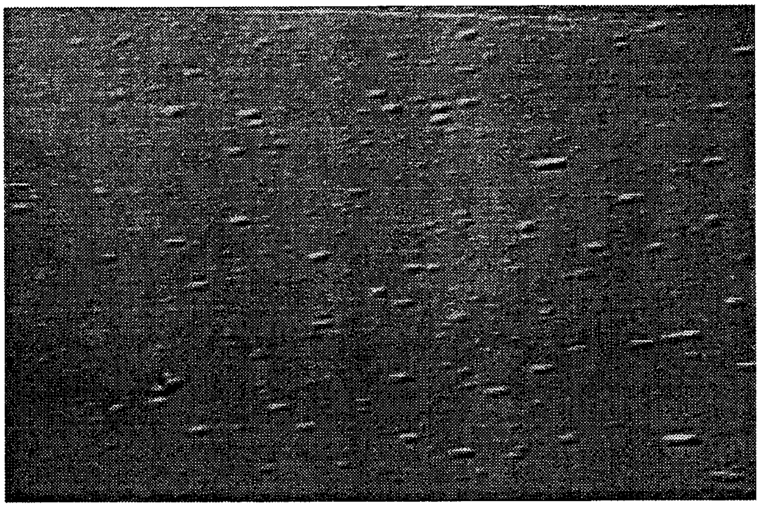

Fig. 8.4 InP surface morphology.

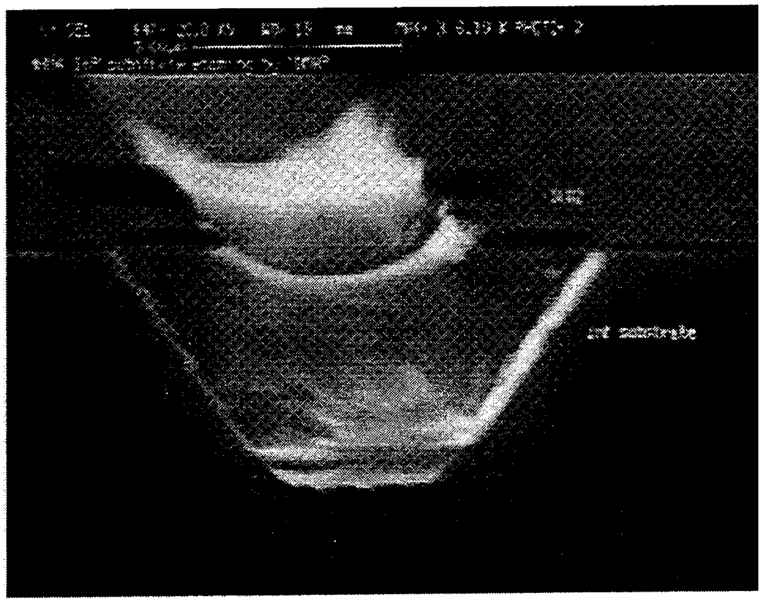

Fig. 8.5 The SEM picture showing the TDMAP etching effect at 570°C on a SiO_2-masked GaAs patterned substrate.

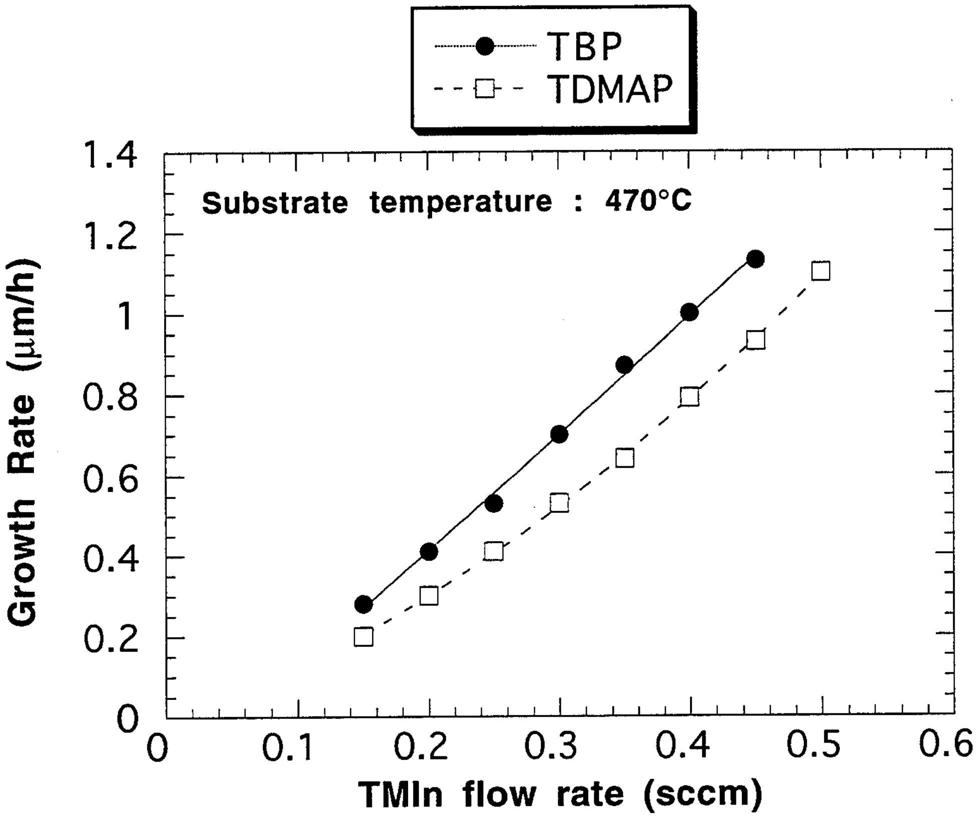

Fig. 8.6 The dependence of the InP growth rate on the TMIn flow rate using cracked TBP and cracked TDMAP.

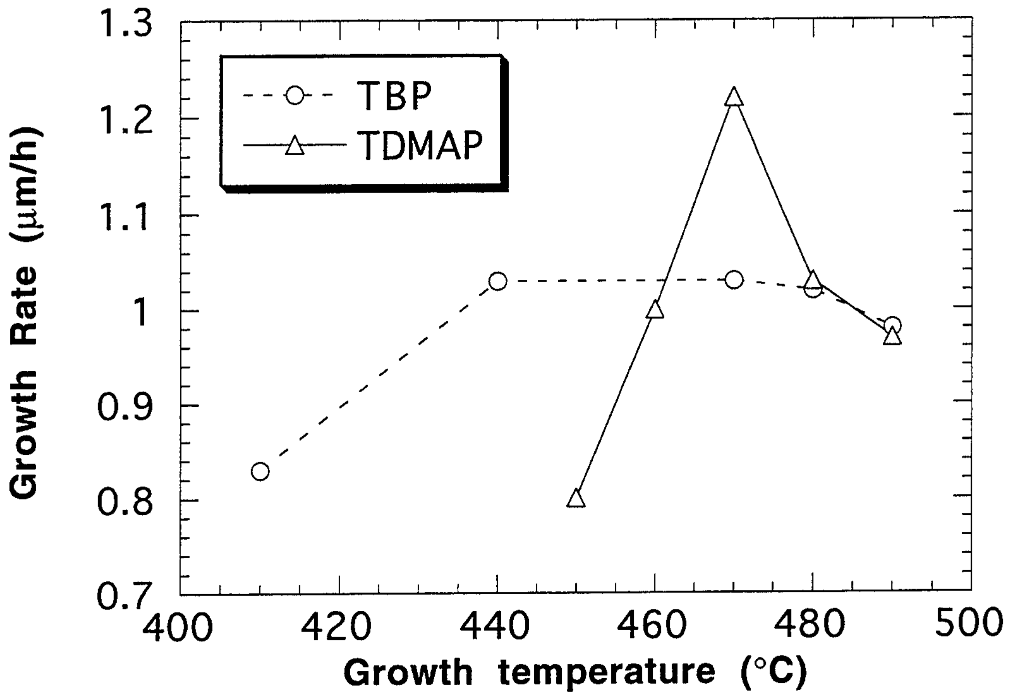

Fig. 8.7 InP growth rate as a function of substrate temperature.

temperature is higher than 490°C, the higher desorption rate of TMIn lowers the growth rate. On the other hand, the InP growth rate is strongly dependent on the substrate temperature in the temperature range of 450 to 490°C when TDMAP is used. In this case, the etching effect from TDMAP may play an important role. This etching effect, together with the decomposition and desorption efficiency of TMIn molecules, contributes to the temperature sensitivity in the growth rate.

8.3 Growth of InGaP by CBE

InGaP grown on GaAs with uncracked TDMAP were found to have droplet features on the surface. Figure 8.8 shows an SEM photograph of a typical InGaP surface grown on a GaAs substrate using uncracked TDMAP. The droplet formation may be due to an indium-enhanced phosphorous desorption on the epilayer surface observed by Abernathy *et al.*[8.1]. Typical x-ray rocking curve data shows only a GaAs substrate peak for these samples, which indicates no InGaP was grown on the GaAs surface.

By using cracked TDMAP, we were able to grow InGaP on GaAs, but x-ray rocking curve data and SEM photographs of the surface morphology show poor film quality. Figure 8.9 shows the x-ray rocking curve for the InGaP sample grown at a substrate temperature of 500°C with a cracker temperature at 750°C. The InGaP growth rate was 0.5 μm/h according to RHEED oscillation measurements. The $In_{0.4}Ga_{0.6}P$ peak is separated from the GaAs substrate peak by a theta angle of 0.19° as shown in Figure 8.9. Figure 8.10 shows the surface morphology of this sample. Many defects were observed on the surface (oriented along the [011] direction), which may be due to the etching effect caused by the TDMAP source. We have also seen similar defects oriented along a specific direction on GaP epilayers grown with cracked TDMAP.

InGaP samples grown at a substrate temperature of 470°C resulted in spotty RHEED diffraction pattern after 10 minutes of growth. The surface morphology of the InGaP

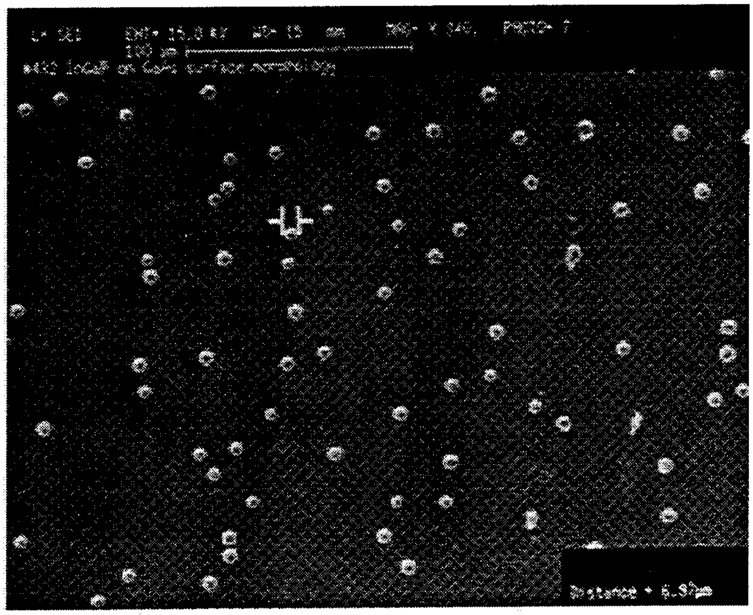
EHT= 15.0 kV
100 µm
InGaP on GaAs surface morphology
Distance

Fig. 8.8 SEM photograph of a typical InGaP surface grown on a GaAs substrate using uncracked TDMAP.

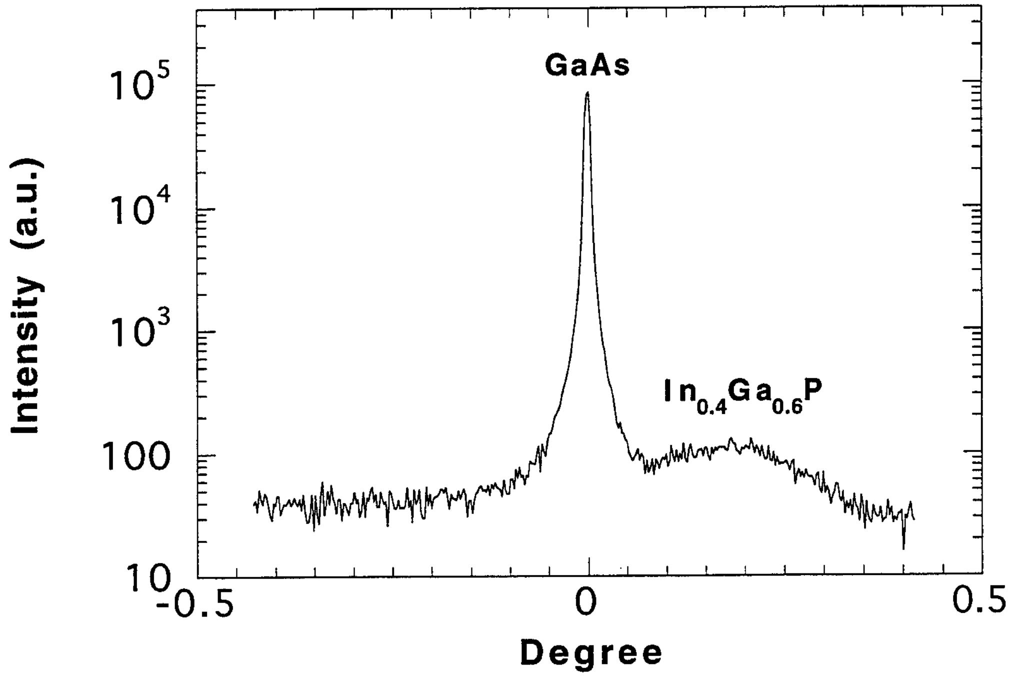

Fig. 8.9 X-ray rocking curve for the InGaP sample grown at a substrate temperature of 500°C with a TDMAP cracker temperature at 750°C.

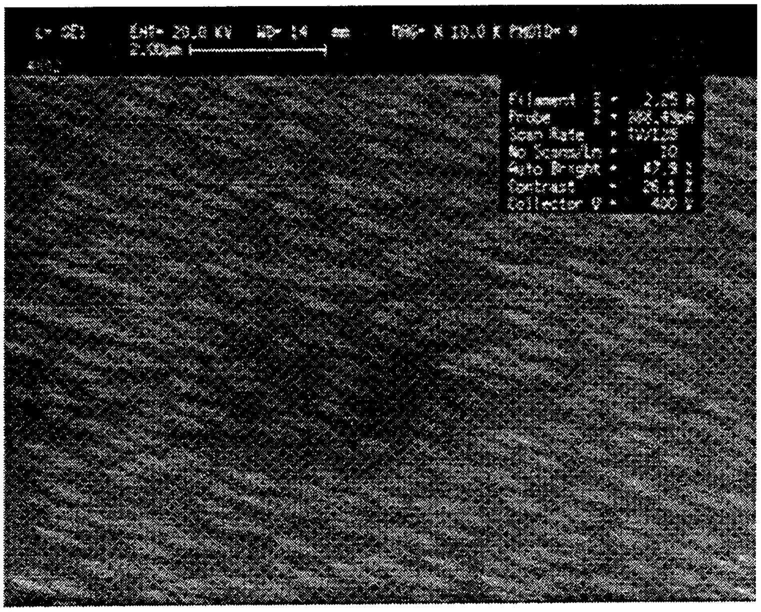
EHT= 20.0 KV
WD= 14 mm
MAG= X 10.0 K
2.00µm
Filament
2.25 A
Probe
Scan Rate
No Scans/Ln
Auto Bright
Contrast
Collector V
400 V

Fig. 8.10 SEM photograph showing the surface morphology of the InGaP sample grown at 500°C with TDMAP cracked at 750°C.

layer taken from an SEM is shown in Figure 8.11. The cause of the spotty RHEED diffraction pattern maybe attributed to this "lumpy" surface morphology that was formed.

To improve the surface morphology and obtain optical quality InGaP epilayers, TBP was used as a group V source. Featureless and specular surface morphology of the InGaP epilayers with In composition from 0.4 to 0.65 was obtained at a V/III ratio of 1.5 and a growth temperature of 500°C. The cracker temperature was set at 850°C. Fig. 8.12 shows a x-ray rocking curve of the $In_{0.45}Ga_{0.55}P$ epilayer. The lattice mismatch between the substrate and the epilayer is in the order of 10^{-3}. The low-temperature photoluminescence of the $In_{0.45}Ga_{0.55}P$ epilayer with a FWHM of 12 meV is shown in Fig. 8.13. These results demonstrate that good-quality InGaP epilayers can be grown on a GaAs substrate using cracked TBP as a group V source. Further work will be done to optimize the growth conditions of the InGaP material using TBP.

8.4 References

8.1 C. R. Abernathy, D. A. Bohling, G. T. Muhr, and P. W. Wisk, Mater. Res. Soc. Symp. Proc. *340*, 161 (1994).

8.2 G. Zimmermann, H. Protzmann, T. Marschner, O. Zsebök, W. Stolz, E. O. Göbel, P. Gimmnich, J. Lorberth, T. Filz, P. Kurpas, and W. Richter, J. Cryst. Growth *129*, 37 (1993).

8.3 C. Hincelin, M. Zahzouh, R. Mellet, and A. M. Pougnet, J. Cryst. Growth *120*, 119 (1992).

8.4 E. A. Beam III, H. F. Chau, T. S. Henderson, W. Liu, and A. C. Seabaugh, J. Cryst. Growth *136*, 1 (1994).

8.5 C. Jagadish, A. A. Allerman, N. Hauser, C. C. Hsu, and M. Gal, J. Cryst. Growth *145*, 953 (1994).

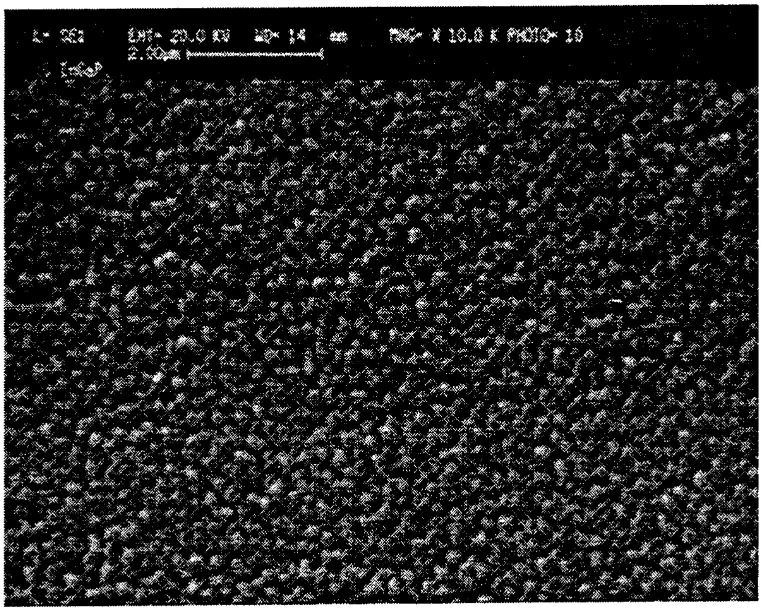
EHT= 20.0 KV
WD= 14 mm
MAG= X 10.0 K
PHOTO= 10
2.00µm
InGaP

Fig. 8.11 SEM photograph showing the “lumpy” surface morphology for the InGaP sample grown at 470°C.

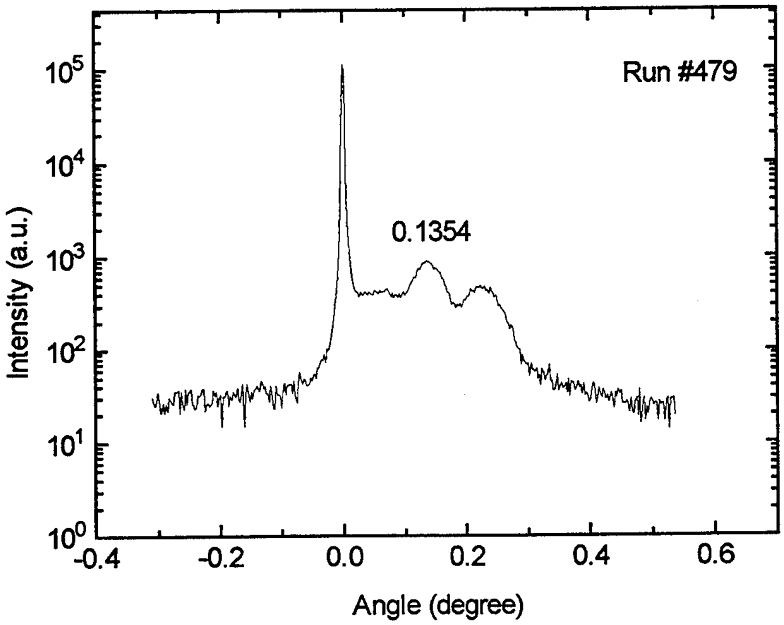

Fig. 8.12 X-ray rocking curve of InGaP layer grown at 500°C with TBP cracked at 850°C.

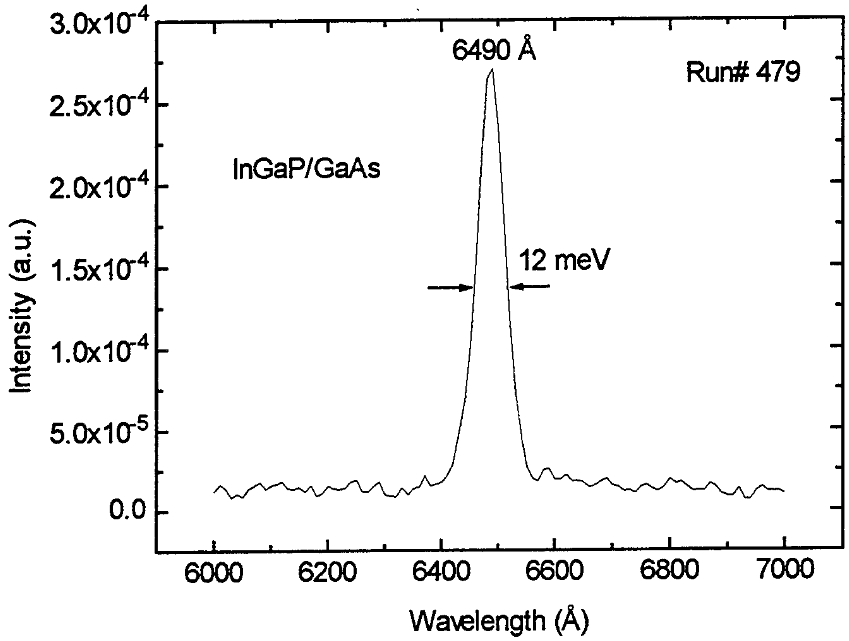

Fig. 8.13 The low-temperature PL spectrum of the InGaP layer grown by cracked TBP.

9. Recommendations

9.1 Modification of Laser Optics

Because of the long distance between the substrate and the laser entrance viewport in our modified MBE system, a long focal-length lens is required, which results in a focused laser spot size of ~ 300μm in diameter. Because CBE does not need a source cryoshroud (since using near-room-temperature sources), a modified source flange that allows a shorter distance between the substrate and the laser-entrance port can be installed to minimize the laser spot. In order to avoid obtaining the Gaussian profile of the laser beam on the substrate surface, a beam homogenizer is necessary to be incorporated into the present optics. A flat surface of laser-grown spot would be desirable for processing. After the laser beam passes a beam homogenizer, a flat-top profile can be obtained at a specific plane, and the pattern size can be magnified or reduced to what we want by a lens.

9.2 Laser-Assisted CBE of InGaP with TBP and TDMAP

InGaP has many advantages over $Al_{0.3}Ga_{0.7}As$, e.g., no DX centers, which is advantageous for HEMTs, smaller ΔE_C and larger ΔE_V, which is good for HBTs, higher breakdown field, and good etching selectivity over GaAs. Based on the results of CBE of InGaP using TBP and TDMAP discussed in Chapter 8, it would be interesting to explore laser-assisted CBE of InGaP. Further investigation of laser-assisted CBE of InGaAsP is also needed due to its important optoelectronic applications.

9.3 Laser Holographic Growth

An application that is unique to laser-assisted growth is growth of gratings and arbitrary shapes by holography. This technique utilizes the interference of two laser beam from the same laser source, as shown in Fig. 9.1a. The mirror setup on the GaAs substrate is designed to minimize the influence from the system vibration. In principle, a grating pattern can be formed on the substrate by laser interference, as shown in Fig. 9.1b. By adjusting the angle between the two laser beams, submicron grating will be possible. Vibration isolation, however, is paramount to the realization of laser holographic growth.

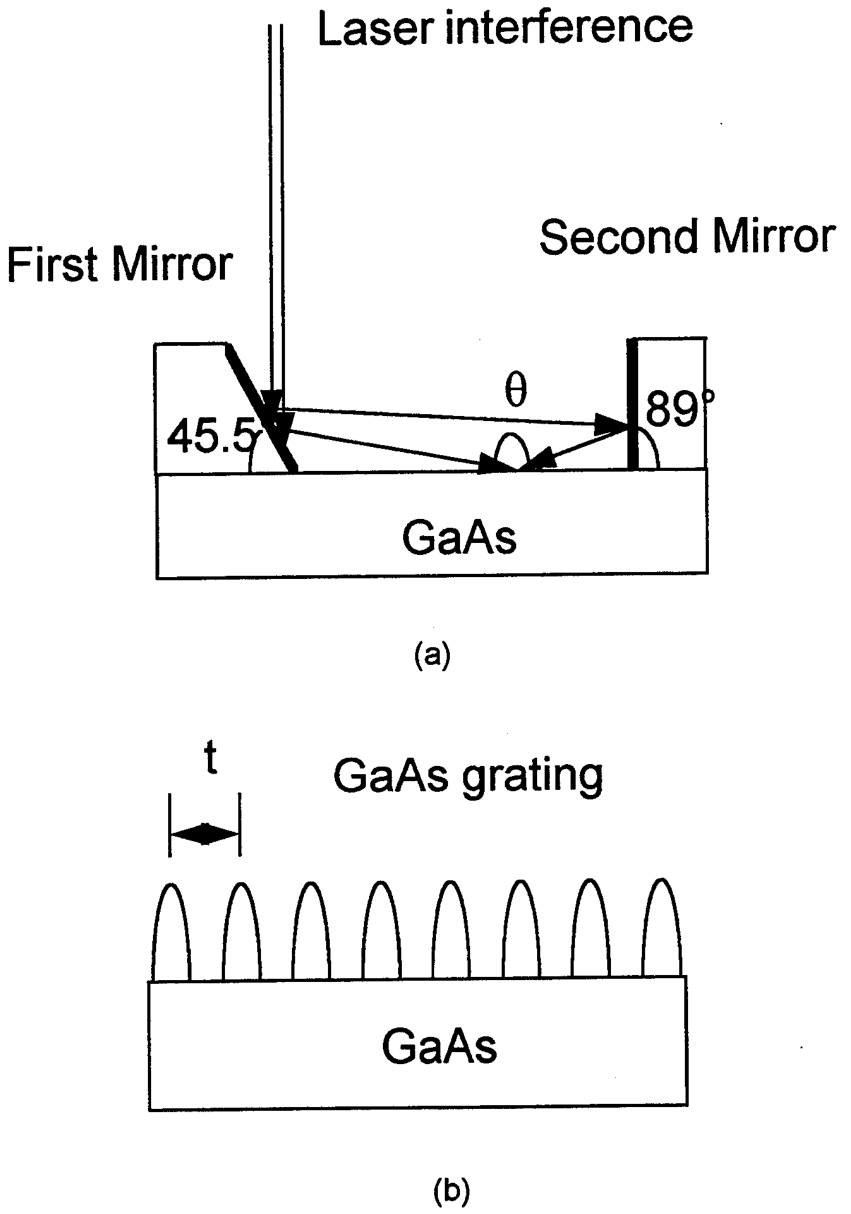
Laser interference
First Mirror
Second Mirror
θ
45.5°
89°
GaAs
t
GaAs grating
GaAs

(a)

(b)

Fig. 9.1 (a) Laser holography setup. (b) GaAs grating pattern.

Appendix A Selectively Regrown Carbon-Doped (Al)GaAs by CBE with Novel Gas Sources for HBT Applications

A1 Introduction

Recently, selective-area epitaxy (SAE) by chemical beam epitaxy (CBE) or metalorganic molecular beam epitaxy (MOMBE) is emerging as a very promising technology for the fabrication of planar, monolithic electronic and photonic integrated circuits. For fabricating advanced high-speed GaAs-based devices, selectively regrown n^+-GaAs layer on a pseudomorphic high electron mobility transistor structure[A1] and selectively grown permeable junction base transistor with a highly carbon-doped GaAs gate layer[A2] have been successfully achieved by CBE. In the area of photonic devices, the selectively buried growth of InGaAs/InP multilayers by CBE for double-heterostructure lasers are widely used[A3-5]. SAE also has the potential for preparing low-dimensional structures, such as quantum wires[A6, A7]. It is generally accepted that the growth rate and the composition of compounds grown selectively by CBE depends less sensitively on the growth area, in contrast to metalorganic chemical vapor deposition (MOCVD)[A8]. The high vacuum environment in CBE eliminates gas-phase reactions and the growth is controlled by only the chemical reactions of the sources on the heated substrate. Therefore, CBE is a suitable technique for SAE.

Most of these SAE studies on GaAs-based materials, however, were achieved by using the extremely toxic arsine (AsH_3). In this study, we investigate SAE using a much less toxic source, tris-dimethylaminoarsenic (TDMAAs), which has been reported to be a suitable replacement for AsH_3 to grow high-quality GaAs and AlGaAs materials by CBE[A9, A10]. In our SAE study, we found that using TDMAAs can achieve complete selectivity of (Al)GaAs layers at a lower growth temperature[A11] than using AsH_3 or As_4.[A12-14] The growth behavior of GaAs and AlGaAs in the unmasked region, however, has not been clear. Moreover, to improve the microwave performance of heterojunction bipolar transistors (HBTs) without sacrificing current gain, a lower base sheet resistance is highly desirable[A15-17]. To achieve this, an HBT with a lateral base contact (LBC) structure was proposed by regrowing $Al_{0.25}Ga_{0.75}As$/GaAs:C external base layers. The growth profile of the regrown layers can be a limiting factor to reduce the base resistance. Thus, the goal of this work is focused on the growth behavior of SAE in the vicinity of the mask edges to optimize the growth profile for the regrown base layers in an LBC HBT structure.

A2 Selective-Area Growth of (Al)GaAs

The CBE system used in this work was modified from a Perkin-Elmer 425B MBE system. The growth chamber is pumped by turbomolecular pump. Triethylgallium (TEGa) and trimethylaluminum (TMAl) were directly injected into the growth chamber without any carrier gas. The flow rates were controlled by vapor-source mass-flow controllers. TDMAAs was carried by hydrogen and transported into the growth chamber through an ultrahigh vacuum leak valve. Diiodomethane (CI_2H_2), without a carrier gas, was the carbon-doping source and was delivered into the growth chamber through a leak valve. The 4800 Å thick SiO_2 films were deposited on epi-ready semi-insulating (100) GaAs substrates by plasma enhanced chemical vapor deposition (PECVD). Stripe patterns along 011] and $01\bar{1}$] directions were fabricated by conventional photolithography and wet chemical etching in a buffered HF solution. The stripe openings ranged from 1.2 to 100 μm with a 100 μm separation. The patterned GaAs substrates were degreased, rinsed, and etched. The etching was done in $NH_4OH:H_2O(1:5)$ followed by a D.I. water rinse. A second cleaning etch with 20% HCl prior to a final D.I water rinse was used to remove the surface oxide. The samples were then loaded into the CBE chamber and thermally cleaned at 600°C under a flux of cracked TDMAAs for 5 min. Typical growth conditions for the growth rate, V/III ratio, substrate temperature, and CI_2H_2 vapor pressure setting of GaAs:C samples grown by CBE were 0.30-0.75 μm/h, 1.6-5.7, 470-565°C and 0.88-1.50 Torr, respectively. Those for $Al_{0.25}Ga_{0.75}As$:C samples were 0.5 μm/h, 1.6, 470-625°C, and 1.1-1.6 Torr, respectively. The chamber pressure was about $2x10^{-7}$ Torr when the CI_2H_2 was introduced. The V/III incorporation ratios were determined by the group III- and group V-induced RHEED intensity oscillations. The layers thickness, selectivity, and surface morphology were examined by a scanning electron microscope (SEM).

Fig. A1 shows SEM photographs for (a) a nonselective GaAs epitaxial layer grown at 440°C and (b) a selective GaAs epitaxial layer grown at 540°C using TEGa and uncracked TDMAAs. The flow rate of TEGa was varied from 0.24 to 0.40 sccm which corresponded to a GaAs growth rate from 0.25 to 0.60 μm/h. Within this range, true selectivity was achieved at substrate temperatures above 470°C. The surface morphology of the regrown layer in the opening, however, was always rippled. This textured surface morphology was independent of the V/III incorporation ratios between 1.8 to 4.4 in the growth temperature range of 470 to 565°C. In addition, the carbon incorporation efficiency was very low in the GaAs layers. The highest hole concentration obtainable was only $5x10^{18}$ cm^{-3}. It was observed from a quadruple mass spectrum, TDMAAs molecules can be completely decomposed at 350°C. To increase the carbon incorporation efficiency of the GaAs regrown layers, we explored thermally cracking TDMAAs at 350°C. Using this technique, the carbon incorporation efficiency was increased by two orders of magnitude, and the highest hole concentration achieved so far is $6.6x10^{19}$ cm^{-3}, as seen in Chapter 7. In addition, the surface morphology of the selectively regrown GaAs layer is very smooth as shown in Fig. A1c.

Furuhata and Okamoto[A18] and Bove *et al.*[A1] reported that true selectivity of GaAs was achieved at a substrate temperature above 600°C using TEGa and As_4 by MOMBE and between 580 and 620°C using TEGa and AsH_3 by CBE, respectively. In our work, true selectivity of GaAs epitaxial layers with a growth rate of 0.5 μm/h can be achieved at

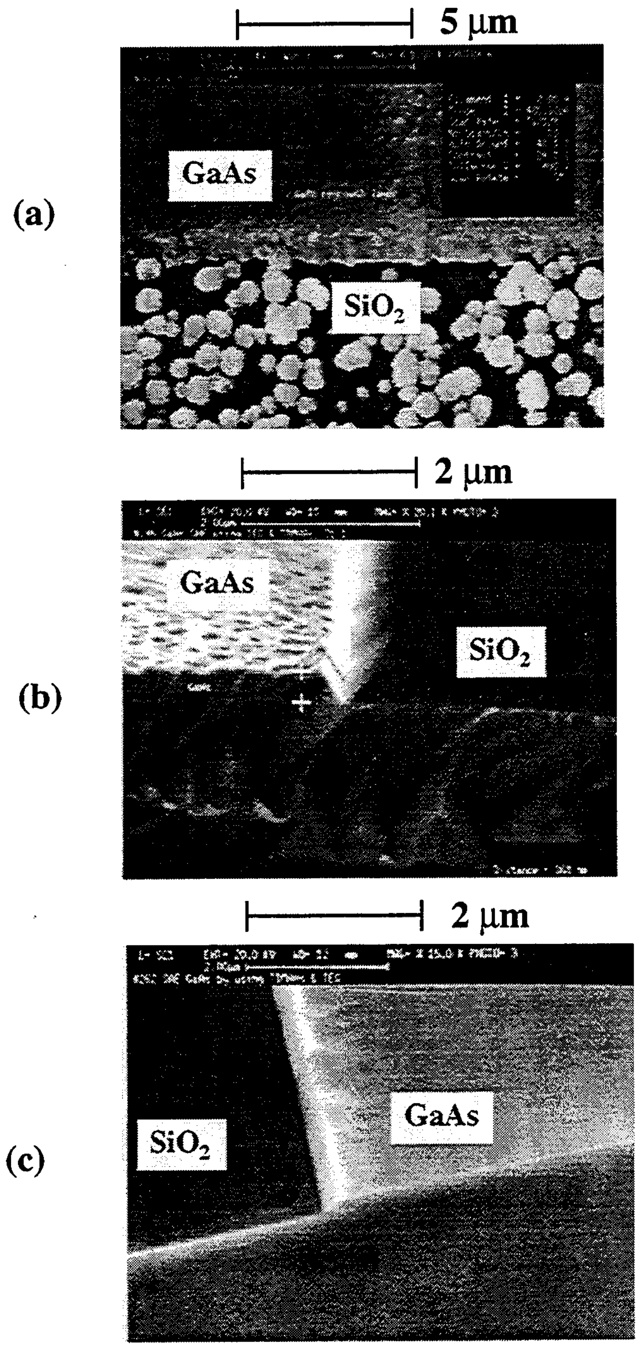
5 µm
GaAs
(a)
SiO2
2 µm
GaAs
SiO2
(b)
2 µm
GaAs
SiO2
(c)

Fig. A1 SEM photographs for GaAs selective area growth: (a) using uncracked TDMAAs at a substrate temperature of 440°C, (b) using uncracked TDMAAs at 540°C, and (c) using cracked TDMAAs at 540°C. The stripe is parallel to the [01$\bar{1}$] direction.

a growth temperature as low as 470°C. This behavior may be due to the fact that amine radicals ($N(CH_3)_x^+$) decomposed from TDMAAs can enhance desorption of TEGa molecules from the SiO_2 surface, resulting in SAE.

In order to evaluate the growth rate dependence on the stripe width, the edge growth enhancement, and the quality of the selectively grown GaAs materials, we designed a mask with stripe openings varying from 1.2 to 100 μm separated by 100 μm. Fig. A2 shows (a) an SEM photograph and (b) a sketch of a typical selective GaAs:C epilayer grown at 540°C with a growth rate of 0.6 μm/h. The stripe, with a 5 μm opening, is along the $01\bar{1}$] direction. A specular surface morphology of the GaAs:C regrown layer is obtained, but the thickness around the edges is slightly thicker than that in the broad area, resulting in "rabbit ears." For the stripe along the 011] direction, however, no significant "rabbit ear" effect is observed under a lower V/III ratio. We deduce that fewer TEGa molecules migrate from the (111)B sidewalls to the top surface due to the much higher growth rate on the (111)B planes compared to that on the (111)A planes[A19].

Fig. A3 shows the broad-area growth rate and the "rabbit ear" thickness of selective GaAs:C layers as a function of the stripe opening for two V/III incorporation ratios, 1.9 and 2.5, indicated by closed circles and squares, respectively. Here, the "rabbit ear" thickness is the thickness difference between the edge and the broad area of the GaAs layer. Solid and dash lines represent the broad-area growth rate and the "rabbit ear" thickness, respectively. The growth rate remains independent of the feature size down to about 5 μm, but as the opening size decreases below 5 μm, a growth-rate enhancement emerges. An approximately 28% increase of the growth rate was observed for a stripe opening of 1.4 μm. This growth-rate enhancement in the smaller stripe openings is attributed to the migration of impinging TEGa molecules from the sidewall planes to the top surface. From this result, we can estimate that the migration length near the edge, where the growth rate increased, is about 1.5 μm. This behavior has been observed in InGaAs epilayers selectively grown on InP patterned substrates[A20]. Furthermore, as

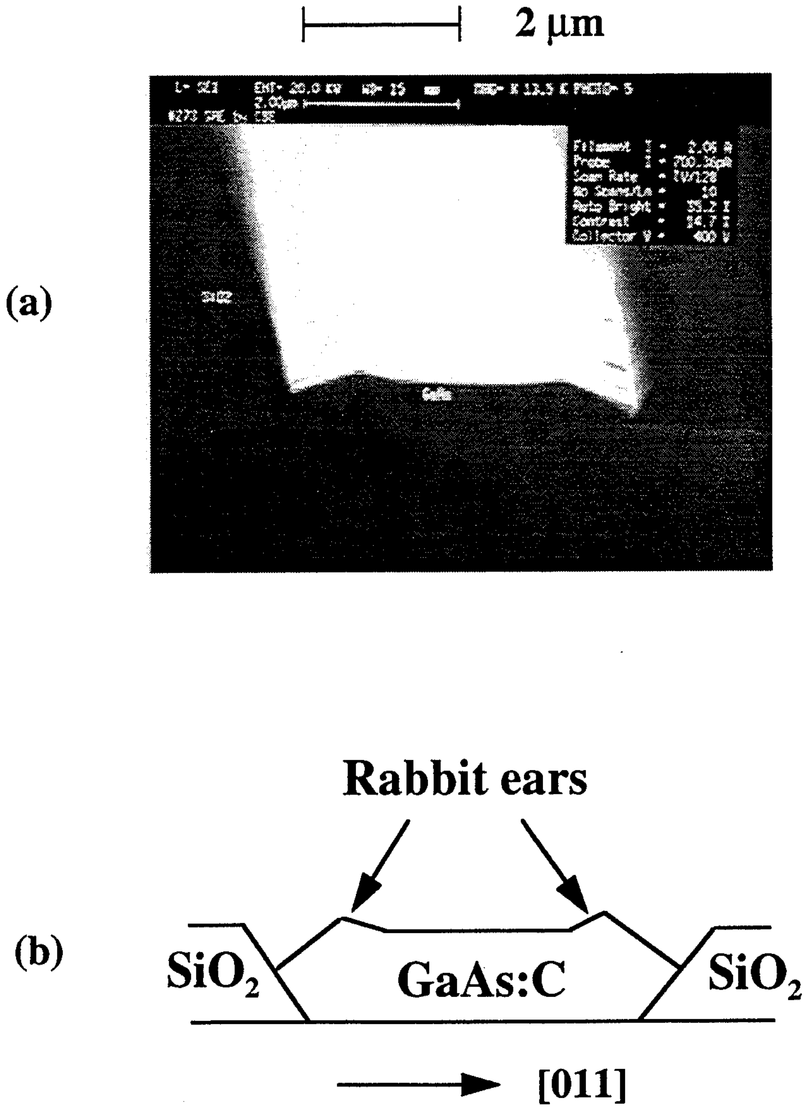
2 µm
(a)
SiO2
GaAs
Rabbit ears
(b)
SiO2
GaAs:C
SiO2
[011]

Fig. A2 SEM photograph of aselective GaAs:C layer in a stripe opening of 5µm grown at 540°C with a V/III ratio of 1.85.

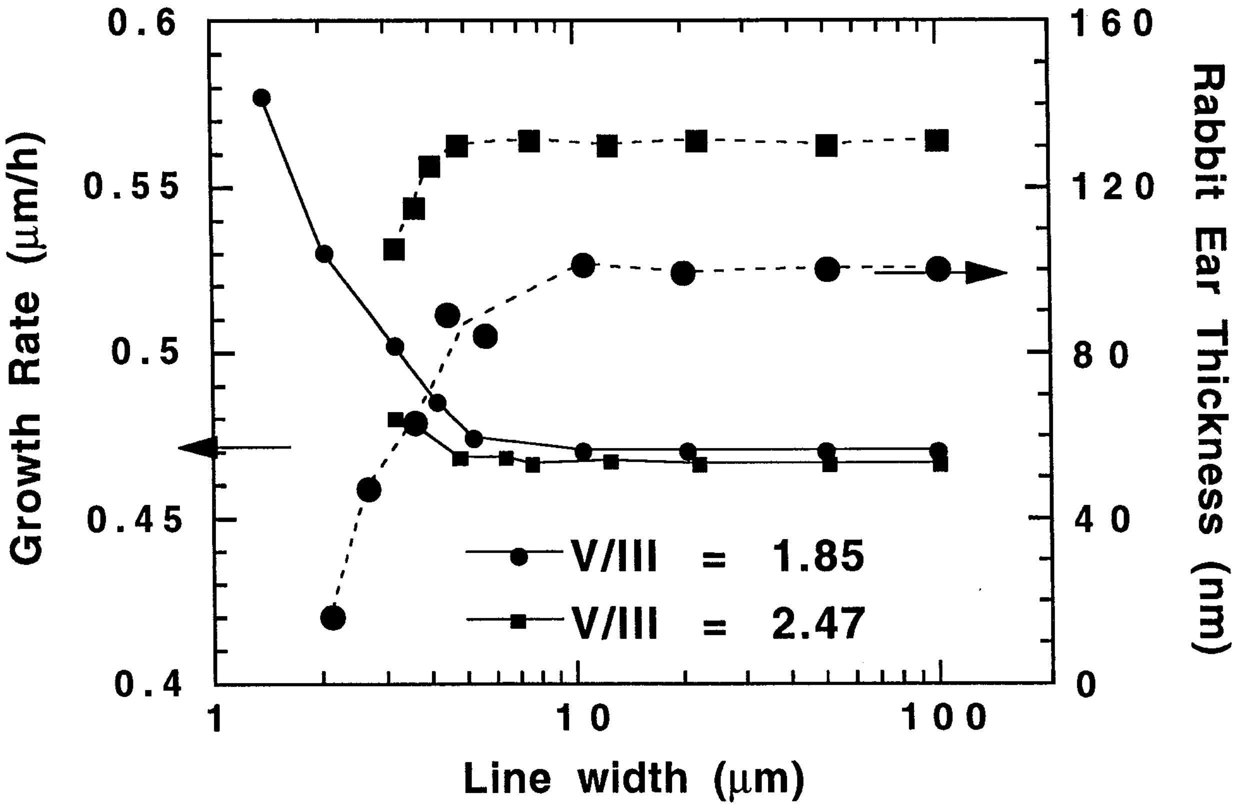

Fig. A3 Broad-area growth rate and “rabbit-ear” thickness of GaAs:C layers as a function of stripe openings for two values of V/III ratios. The thickness of the GaAs:C layer is 470 nm.

shown in Fig. A3, the "rabbit ear" thickness decreases for stripe openings below 5 μm and lower V/III ratios. Therefore, we can conclude that when the stripe opening is less than 5 μm, the TEGa molecules migrating from the sidewalls not only contribute to the growth around the edge but also enhance the growth in the broad area. When the stripe opening is nearly equal to the migration length, the "rabbit ear" effect should be minimal. At a higher V/III ratio, the migration length of TEGa molecules decreases on the growth surface and results in a more serious "rabbit ear" effect. Therefore, to minimize the edge growth enhancement, selective GaAs layers should be grown at a lower V/III ratio.

True selective-area epitaxy of $Al_{0.25}Ga_{0.75}As$ layers with a growth rate of 0.5 μm/h can be achieved at substrate temperatures between 470 and 530°C. At growth temperatures higher than 540°C, aluminum droplets appear on the SiO_2 surface, resulting in non-selective area growth.

Figs. A4 (a)-(d) show schematic cross sections along $01\bar{1}]$ and $011]$ directions of the GaAs epilayers selectively grown under different V/III ratios. The results indicate that the V/III ratio strongly affects the facet formation in both $011]$ and $01\bar{1}]$ directions. For stripes along the $01\bar{1}]$ direction, when the V/III ratio increases from 1.7 to 3.5, the high-index (311)A facets on both sides of the GaAs stripes gradually disappear and are replaced by (111)A facets and vertical (110) sidewalls. At an even higher V/III ratio of 5.7, only (111)A sidewalls form. Note also that there is no growth on the SiO_2 sidewalls for a V/III ratio higher than 3.5. In the case of the $011]$ direction, the facet formation is opposite to that in the $01\bar{1}]$ direction. We observe vertical sidewalls at a V/III ratio of 1.7, but when the V/III ratio increases, the vertical sidewalls disappear gradually and (311)B facets become dominant. Fig. A5 shows typical cross-sectional SEM photographs for SAE GaAs layers grown at a V/III ratio of 1.7 with (a) (311)A facets and (b) vertical sidewalls for stripes along $01\bar{1}]$ and $011]$ direction, respectively.

These opposite growth behaviors are due to the different surface-reaction kinetics of the growing surface. In the vicinity of the mask edges, the facet formation is usually

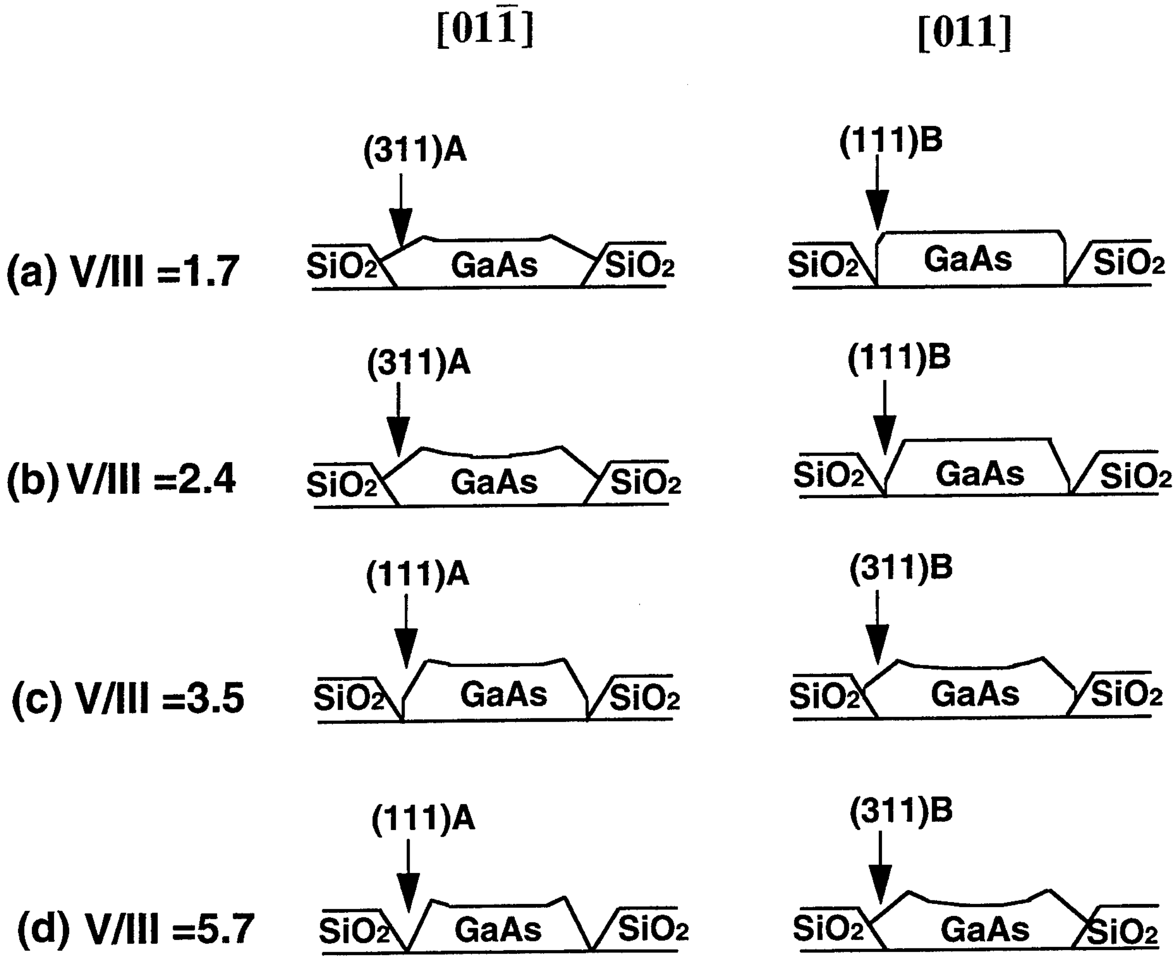
[01$\bar{1}$]
[011]
(a) V/III =1.7
(b) V/III =2.4
(c) V/III =3.5
(d) V/III =5.7
(311)A
(111)B
(311)A
(111)B
(111)A
(311)B
(111)A
(311)B
SiO2
GaAs
SiO2

Fig. A4 Schematic cross-section of GaAs:C layers grown at V/III ratio of (a) 1.7 (b) 2.4 (c) 3.5 (d) 5.7 along [01$\bar{1}$] and [011] directions.

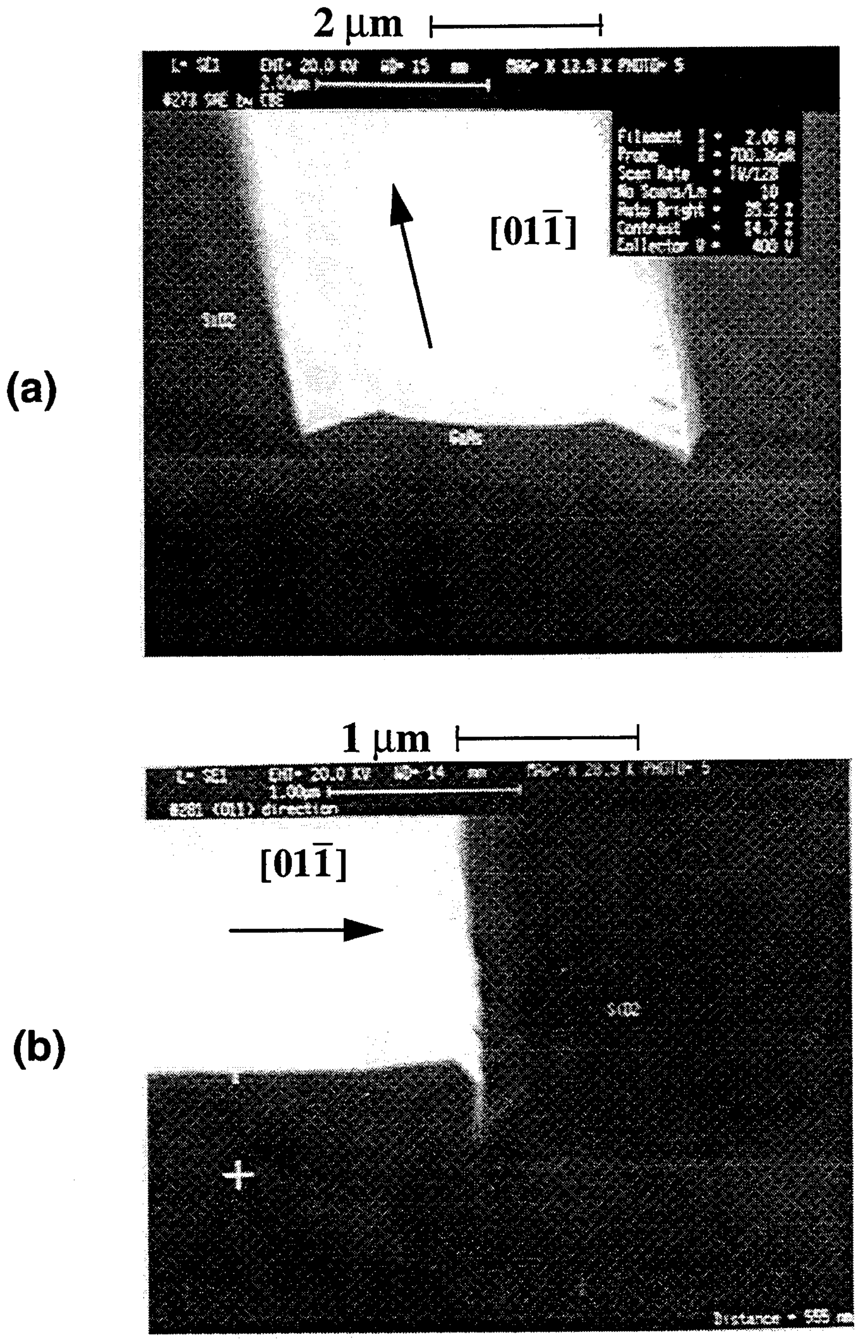
2 µm
$[01\bar{1}]$
SiO2
GaAs
(a)
1 µm
$[01\bar{1}]$
SiO2
(b)

Fig. A5 The typical SEM photographs of GaAs layers with
(a) (311)A facets along [011] direction, and
(b) vertical sidewalls along $[01\bar{1}]$ direction grown at a V/III of 1.7.

determined by the slowest growing planes, which are generally (111) planes. The (111) growing planes in the stripes along $0\bar{1}1]$ and 011] directions are (111)A and (111)B, respectively. The orientation of these growth fronts can significantly affect the growth rate of the GaAs layers, resulting in different facet formations of the regrown layers. Legay *et al.*[A19] reported that the growth rate of GaAs on (110) and (111) orientations is much lower than that on (100). The growth rate of a specific plane can be tuned by adjusting the V/III incorporation ratio. For (111)B orientation, the growth rate can be dramatically increased by decreasing the value of V/III ratio close to 1. Therefore, for stripes along the $0\bar{1}1]$ direction, the slowest growing planes at a lower V/III ratio are (111)A and (110), leading to the formation of (311)A facets. When the V/III ratio increases, the growth rate of (110) planes is much higher than that of (111)A planes, which then determines the facet formation. In the case of stripes along the 011] direction, the growth rate of (111)B is much higher than that of (110) at a V/III ratio of 1.7, resulting in vertical sidewalls. When the V/III ratio increases, the slowest planes are (111)B and (110), which eventually proceeds to form the (311)B facets. Moreover, we also found that the facet formation of $Al_{0.25}Ga_{0.75}As$ around masks was similar to that of GaAs.

A3 Regrown LBC Structure for HBT

The dependence on the mask pattern orientation is very critical in the design of regrown layers for the LBC structure. To achieve a complete coupling between the regrown external-base layers and the intrinsic-base layer of an HBT, lateral growth is highly desirable. Therefore, the V/III ratio should be close to 1 and the stripes opening for SAE must be parallel to $0\bar{1}1]$ direction. An SEM photograph and a schematic cross section of the embedded SAE AlGaAs/GaAs:C layers in an undercut groove is shown in Fig. A6. The stripe opening is along the $0\bar{1}1]$ direction and the V/III ratio is 1.3. It

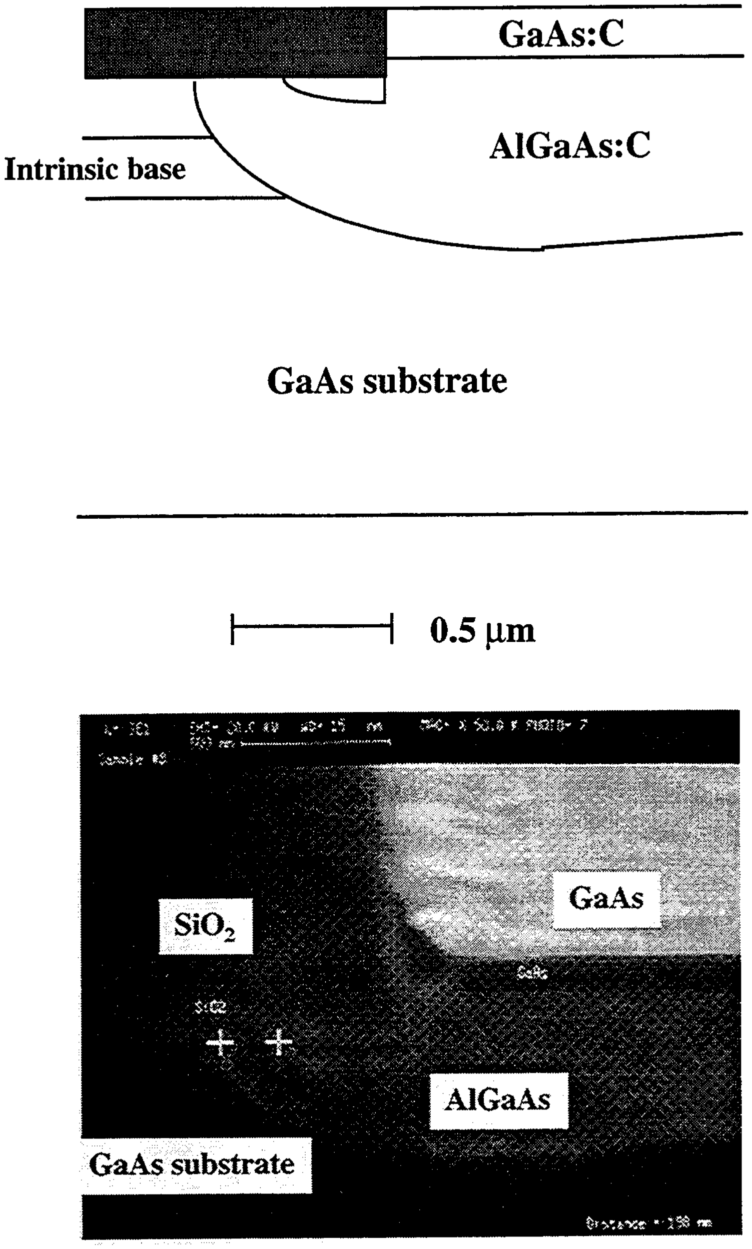
GaAs:C
AlGaAs:C
Intrinsic base
GaAs substrate
0.5 µm
SiO$_2$
GaAs
AlGaAs
GaAs substrate

Fig. A6 An SEM photograph and schematic cross-section of the embedded SAE AlGaAs/GaAs:C layers grown in an under cut groove at a V/III ratio of 1.3. The stripe is along the $[01\bar{1}]$ direction.

shows that the lateral coupling between GaAs substrate and AlGaAs/GaAs:C layers is quite good.

To improve the microwave performance of HBTs without sacrificing current gain, a lower base sheet resistance is highly desirable[A15, A21]. One HBT structure with a LBC has the external base layers regrown on the collector layer. We regrew heavily carbon-doped GaAs(800 Å)/$Al_{0.25}Ga_{0.75}As$(2000 Å) external base layers on an MOCVD-grown structure. The external base layers were regrown at 500°C. The intrinsic p-type carbon-doped $In_{0.005}Ga_{0.995}As$ base layer is 500 Å with a hole concentration of $4x10^{19}$ cm^{-3}. From the transmission-line measurement, the base sheet resistance is 350 $\Omega/\square$. The hole concentration of the carbon-doped GaAs/$Al_{0.25}Ga_{0.75}As$:C external base layers is higher than $4x10^{19}$ cm^{-3}, and the base sheet resistance is 132 $\Omega/\square$. This experimental value of the base sheet resistance is very close to a value of 115 $\Omega/\square$ calculated from measured Hall mobility (24 $cm^2/V\cdot s$) and carrier concentration ($p=8x10^{19}$ cm^{-3}) on an unpatterned wafer grown at the same time. The agreement indicates that the regrown interface does not contain many traps. An approximately 62% reduction of the base sheet resistance is obtained in the LBC structure. The common emitter DC current gain of large-area (75x75 μm^2) transistors versus collector current for the original and the LBC structures are plotted in Fig. A7. Due to its wide energy bandgap, an $Al_{0.25}Ga_{0.75}As$:C layer is regrown as a passivation layer. As a result, a better minority carrier confinement and a lower surface recombination current are achieved after regrowth, resulting in a lower base current in the LBC structure. Therefore, the LBC structure has a much larger current gain than the original HBT. The microwave performance of smaller-area HBTs is still under study and will be reported elsewhere.

A4 References

A1. P. Bove, K. Ono, K. Joshin, H. Tanaka, K. Kasai and J. Komeno, J. Crystal Growth *136*, 261 (1994).

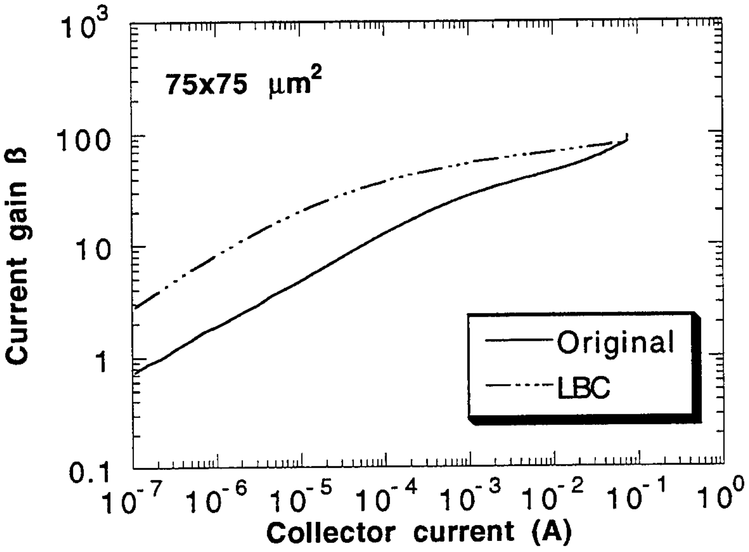

Fig. A7 Common-emitter current gain as a function of collector current for the original and the regrown external-base HBT structure.

A2. G. Mörsch, J. Gräber, M. Kamp, M. Hollfelder and H. Lüth, J. Crystal Growth *136*, 256 (1994).

A3. W. T. Tsang, L. Yang, M. C. Wu and Y. K. Cheng, Electron. Lett. *27*, 3 (1991).

A4. Y. L. Wang, H. Temkin, R. A. Hamm, R. D. Yadvish, D. Ritter, L. R. Harriott and M. B. Panish, Electron. Lett. *27*, 1324 (1991).

A5. M. Gotoda, H. Sugimoto, Y. Nomura, T. Isu, M. Nunoshita and S. Maruno, J. Crystal Growth *140*, 277 (1994).

A6. H. Sugiura, T. Nishida, R. Iga, T. Yamada and T. Tamamura, J. Crystal Growth *12*, 579 (1992).

A7. T. Nishiad, H. Sugiura, M. Notomi and T. Tamamura, J. Crystal Growth *132*, 91 (1993).

A8. O. Kayers, J. Crystal Growth *107*, 989 (1991).

A9. C. R. Abernathy, P. W. Wisk, D. A. Bohling and G. T. Muhr, Appl. Phys. Lett. *60*, 2421 (1992).

A10. H. K. Dong, N. Y. Li, C. W. Tu, M. Geva and W. C. Mitchel, J. Electron. Mater. *24*, 69 (1994).

A11. N. Y. Li, Y. M. Hsin, H. K. Dong, P. M. Asbeck and C. W. Tu, to be published in J. Cryst. Growth (1995).

A12. Y. C. Pao, J. Flanklin and C. Shih, to be published in J. Cryst. Growth (1995).

A13. E. Tokumitsu, Y. Kudou, M. Konagai and K. Takahashi, Jpn. J. Appl. Phys. *24*, 1180 (1989).

A14. H. Heinecke, A. Brauers, F. Grafahrend, C. Plass, N. Pütz, K. Werner, M. Weyers, H. Lüth and P. Balk, J. Cryst. Growth *77*, 303 (1986).

A15. K. Mitani, H. Masuda, K. Mochizuki, and C. Kusano, IEEE Trans. Electron Device Lett., *EDL-13*, 209 (1992).

A16. H. Shimawaki, Y. Amamiya, N. Furuhata, and K. Honjo, IEEE Trans. Electron Device Lett. *EDL-40*, 2124 (1993).

A17. P. Launay, R. Driad, F. Alexandre, Ph. Legay, A. M. Duchenois, presented at the 21st International Symposium on Compound Semiconductors, San Diego, USA, September 1994.

A18. N. Furuhata and A. Okamoto, J. Crystal Growth *112*, 1 (1991).

A19. P. Legay, F. Alexandre, and J. L. Benchimol, to be published in J. Crystal Growth (1995).

A20. M. A. Cotta, L. R. Harriott, Y. L. Wang, R. A. Hamm, H. H. Wade, J. S. Weiner, D. Ritter and H. Temkin, Appl. Phys. Letters *61*, 1936 (1992).

A21. H. Shimawaki, Y. Amamiya, N. Furuhata, and K. Honjo, IEEE Trans. Electron Devices *ED-40*, 2124 (1993).

Appendix B Publications and Presentations

Publications

1. H. K. Dong, N. Y. Li, W. S. Wong, and C. W. Tu, "Growth, doping, and etching of GaAs and InGaAs using tris-dimethylaminoarsenic", submitted to J. Vac. Sci. Technol. (1995).
2. H. K. Dong, N. Y. Li, and C. W. Tu, "Effects of laser irradiation on growth and doping characteristics of GaAs in chemical beam epitaxy", submitted to Mater. Res. Soc. Symp., Spring, (1995).
3. H. K. Dong, N. Y. Li, W. S. Wong, and C. W. Tu, "Laser-enhanced growth, carbon-doping, and in-situ etching of GaAs in chemical beam epitaxy with novel gas sources", to be published in Appl. Phys. Lett. (1995).
4. H. K. Dong, N. Y. Li, and C. W. Tu, "Chemical beam Epitaxy (CBE) and laser-enhanced CBE of InGaAs using tris-dimethylaminoarsenic", to be published in J. Electron. Mater. (1995).
5. H. K. Dong, N. Y. Li, and C. W. Tu, "Laser-modified chemical beam epitaxy of InGaAs/GaAs multiple quantum wells using tris-dimethylaminoarsenic", to be published in Mater. Res. Soc. Symp. Proc., (1995).
6. H. K. Dong, N. Y. Li, and C. W. Tu, "Chemical beam epitaxy of InGaAs/GaAs multiple quantum wells using cracked or uncracked tris-dimethylaminoarsenic", to be published in the Proc. 21st Int'l. Symp. Comp. Semicon. (1995).
7. H. K. Dong, S. C. H. Hung, and C. W. Tu, "The effects of laser irradiation on InGaAs/GaAs multiple quantum wells grown by metalorganic molecular beam epitaxy", to be published in J. Electron. Mater. (1995).
8. H. K. Dong, N. Y. Li, C. W. Tu, M. Geva, and W. C. Mitchel, "A study of chemical beam epitaxy of GaAs using tris-dimethylaminoarsenic", J. Electron. Mater. **24**, 69 (1995).
9. H. K. Dong, N. Y. Li, C. W. Tu, M. Geva, and W. C. Mitchel, "Chemical beam epitaxy (CBE) and laser-enhanced CBE of GaAs using tris-dimethylaminoarsenic", Mat. Res. Soc. Symp. Proc. **340**, 173 (1994).
10. H. K. Dong, S. C. H. Hung, and C. W. Tu, "Reflection high-energy electron diffraction study of metalorganic molecular beam epitaxy of GaAs and InGaAs", Mat. Res. Soc. Symp. Proc. **340**, 193 (1994).

11. H. K. Dong, B. W. Liang, M. C. Ho, S. Hung, and C. W. Tu, "A study of Ar ion laser-assisted metalorganic molecular beam epitaxy of GaAs by reflection high-energy electron diffraction", J. Cryst. Growth **124**, 181 (1992).

12. C. W. Tu, H. K. Dong, and N. Y. Li, "Metal-organic molecular beam epitaxy (MOMBE) and laser-modified MOMBE of III-V semiconductors", to be published in the Proceeding of the 1994 IUMRS International Conference on Electronic Materials; also to be published in Materials Chemistry and Physics (1995).

13. N. Y. Li, H. K. Dong, Y. M. Hsin, P. M. Asbeck, and C. W. Tu, "Heavily carbon doped (Al)GaAs epitaxial layers using diiodomethane (CI_2H_2) in molecular beam epitaxy and chemical beam epitaxy for HBT applications", to be published in the Proceeding of the 1994 IUMRS International Conference on Electronic Materials.

14. N. Y. Li, Y. M. Hsin, H. K. Dong, T. Nakamura, P. M. Asbeck, and C. W. Tu, "Selectively regrown carbon-doped (Al)GaAs by chemical beam epitaxy with novel gas sources", to be published in J. Cryst. Growth (1995).

15. N. Y. Li, H. K. Dong, Y. M. Hsin, P. M. Asbeck, and C. W. Tu, "Selectively-area epitaxy of carbon-doped p-type GaAs by metalorganic molecular beam epitaxy with novel gas sources", to be published in J. Vac. Sci. Tech (1995).

16. N. Y. Li, H. K. Dong, C. W. Tu and M. Geva, "P-type GaAs doped by diiodomethane (CI_2H_2) in molecular beam epitaxy (MBE), metal-organic MBE, and chemical beam epitaxy", to be published in J. Cryst. Growth (1995).

17. S. C. H. Hung, H. K. Dong, and C. W. Tu, "Non-contact substrate temperature measurements with infrared laser interferometry", Mat. Res. Soc. Symp. Proc. **340**, 35 (1994).

Conference Presentations

1. H. K. Dong, B. W. Liang, M. C. Ho, S. C. H. Hung, and C. W. Tu, "RHEED Study of Ar ion laser-assisted metalorganic MBE of GaAs", *6th International Conference on Metalorganic Vapor Phase Epitaxy*, Cambridge, Massachusetts, June 8-11, 1992.

2. H. K. Dong, S. C. H. Hung, and C. W. Tu, "Reflection high-energy electron study of metalorganic molecular beam epitaxy of GaAs and InGaAs", *35th Electronic Materials Conference*, Santa Barbara, California, June 23-25, 1993.

3. H. K. Dong, N. Y. Li, and C. W. Tu, "A Reflection high-energy electron diffraction study of metalorganic molecular beam epitaxy of GaAs using tris-dimethylaminoarsenic", *Southern California American Vacuum Society Symposium*, Pasadena, California, September 29, 1993.

4. H. K. Dong, N. Y. Li, C. W. Tu, M. Geva, and W. C. Mitchel, "Chemical beam epitaxy (CBE) and laser-enhanced CBE of GaAs using tris-dimethylaminoarsenic", *Materials Research Society Spring Meeting*, San Francisco, California, April 4-8, 1994.

5. H. K. Dong, S. C. H. Hung, and C. W. Tu, "Reflection high-energy electron diffraction study of metalorganic molecular beam epitaxy of GaAs and InGaAs", *Materials Research Society Spring Meeting*, San Francisco, California, April 4-8, 1994.

6. S. C. H. Hung, H. K. Dong, and C. W. Tu, "Non-contact substrate temperature measurements with infrared laser interferometry", *Materials Research Society Spring Meeting*, San Francisco, California, April 4-8, 1994.

7. H. K. Dong, N. Y. Li, C. W. Tu, "Chemical beam epitaxy (CBE) and laser-enhanced CBE of InGaAs using tris-dimethylaminoarsenic", *36th Electronic Materials Conference*, Boulder, Colorado, June 22-24, 1994.

8. W. C. Mitchel, M. Roth, H. K. Dong, N. Y. Li, and C. W. Tu, "Electrical properties of GaAs grown by MOMBE with triethylgallium and tris-dimethylaminoarsenic", *36th Electronic Materials Conference*, Boulder, Colorado, June 22-24, 1994.

9. N. Y. Li, H. K. Dong, C. W. Tu and M. Geva, "P-type GaAs doped by diiodomethane (CI_2H_2) in molecular beam epitaxy (MBE), metal-organic MBE, and chemical beam epitaxy", *8th International Conference on Molecular Beam Epitaxy*, Osaka, Japan, August 29-September 2, 1994.

10. N. Y. Li, Y. M. Hsin, H. K. Dong, T. Nakamura, P. M. Asbeck, and C. W. Tu, "Selective-area epitaxy of carbon-doped p-type (Al)GaAs by chemical beam epitaxy with novel gas sources", *8th International Conference on Molecular Beam Epitaxy*, Osaka, Japan, August 29-September 2, 1994.

11. H. K. Dong, N. Y. Li, and C. W. Tu, "Chemical beam epitaxy of InGaAs/GaAs multiple quantum wells using cracked or uncracked tris-dimethylaminoarsenic", *21st International Symposium on Compound Semiconductors*, San Diego, California, September 19-22, 1994.

12. N. Y. Li, H. K. Dong, Y. M. Hsin, T. Nakamura, P. M. Asbeck, and C. W. Tu, "Selectively-area epitaxy of carbon-doped (Al)GaAs by chemical beam epitaxy", *14th North American Conference on Molecular Beam Epitaxy*, Urbana-Champaigne, Illinois, October 10-12, 1994.

13. H. K. Dong, N. Y. Li, and C. W. Tu, "Chemical beam epitaxy (CBE) and laser-enhanced CBE of GaAs and InGaAs using tris-dimethylaminoarsenic", *Materials*

Research Society Fall Meeting, Boston, Massachusetts, November 28-December 2, 1994.

14. C. W. Tu, H. K. Dong, and N. Y. Li, "Metal-organic molecular beam epitaxy (MOMBE) and laser-modified MOMBE of III-V semiconductors", *the 1994 IUMRS International Conference on Electronic Materials*, Hsinchu, Taiwan, December 19-22, 1994.

15. N. Y. Li, H. K. Dong, Y. M. Hsin, P. M. Asbeck, and C. W. Tu, "Heavily carbon doped (Al)GaAs epitaxial layers using diiodomethane (CI_2H_2) in molecular beam epitaxy and chemical beam epitaxy for HBT applications", *the 1994 IUMRS International Conference on Electronic Materials*, Hsinchu, Taiwan, December 19-22, 1994.

16. H. K. Dong, N. Y. Li, and C. W. Tu, "Effects of laser irradiation on growth and doping characteristics of GaAs in chemical beam epitaxy", to be presented in *Materials Research Society Spring Meeting*, San Francisco, California, April 17-21, 1995.

17. H. K. Dong, N. Y. Li, W. S. Wong, and C. W. Tu, "Growth, doping, and etching of GaAs using tris-dimethylaminoarsenic", to be presented in *37th Electronic Materials Conference*, Charlottesville, Virginia, June 21-23, 1995.